MASTERARBEIT | MASTER'S THESIS

Titel | Title

The influence of the electrode design and electrode manufacturing on the response of quartz crystal microbalances

verfasst von | submitted by

Paul Johann Karrer BSc

angestrebter akademischer Grad | in partial fulfilment of the requirements for the degree of

Master of Science (MSc)

Wien | Vienna, 2025

Studienkennzahl lt. Studienblatt | Degree programme code as it appears on the student record sheet:	UA 066 862
Studienrichtung lt. Studienblatt | Degree programme as it appears on the student record sheet:	Masterstudium Chemie
Betreut von | Supervisor:	Univ.-Prof. Mag. Dr. Peter Lieberzeit

Table of contents

Abbreviations

16-MHDA	16-mercaptohexadecanoic acid
AAPH	2,2'-Azobis(2-amidinopropane) dihydrochloride
AFM	Atomic force microscopy
AuNP	Gold nanoparticles
CPA	4-cyano-4-(phenylcarbonothioylthio)pentanoic acid
CPE	Copolyester
CVD	Chemical vapor deposition
DMSO	Dimethyl sulfoxide
EDC	1-Ethyl-3-(3-dimethylaminopropyl)carbodiimide
ENPs	Engineered nanoparticles
FC	Fully coated
MAA	Methacrylic acid
MIP	Molecularly imprinted polymer
NHS	N-hydroxysuccinimide
NIP	Non-imprinted polymer
OM	Optical microscopy
PBS	Phosphate buffered saline
PC	Partially coated
PDMS	Polydimethylsiloxane
PLA	Polylactic acid
PVD	Physical vapor deposition
PVP	Polyvinylpyrrolidone
QCM	Quartz crystal microbalance
RAFT	Reversible addition fragmentation chain transfer
RDRP	Reversible deactivation radical polymerization
SECM	Scanning electrochemical microscopy
SEM	Scanning electrode microscopy
SFM	Scanning force microscopy
SPM	Scanning probe microscopy
TRIM	Trimethylolpropane trimethacrylate
vdW	Van der Waals

Acknowledgments

I would like to thank Univ.-Prof. Mag. Dr. Peter Lieberzeit for giving me the opportunity to do my master's thesis in his research group. I am thankful for the continued support throughout my thesis.

Furthermore, I would like to thank every member of the research group for the support. Special thanks to Mahdieh Bagheri, B.Sc., M.Sc., who supervised me and introduced me to most of the applied techniques. More special thanks go out to Ulrich Pacher and Houra Hadadi, M.Sc., who helped in the production of the QCM masks and PVD process.

Finally, I want to thank my family and friends for supporting my educational path and helping me when needed. Special thanks to my parents, Ina Karrer and Johann Karrer, for being there for me throughout my life.

1. Introduction

Rapid detection of various synthetic and biochemical molecules is the goal of various forms of analytics, such as environmental sensing, food analysis or diagnostics. To make sensors for such applications possible, the sensors need to be developed to be fast, cheap, easy to use and small. Chemical sensors comprise of two main parts (see Figure 1), the receptor layer, which interacts with the analyte and upon interaction a physical/chemical change occurs, which is transformed by a transducer into an electric signal and further processed by the measuring electronics.

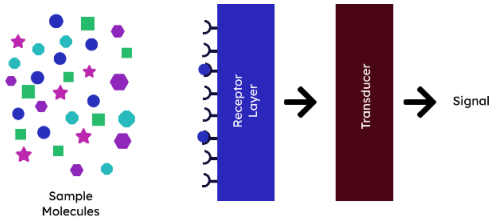

Figure 1: Schematic representation of a sensor [41]

The combination of a quartz crystal microbalance (QCM) with molecularly imprinted polymers (MIP) is a common way of coupling the high selectivity and low cost of the MIPs receptor layer with the high sensitivity of the QCM transducer. To allow for a high-quality measurement the sensors transducer and receptor have to be thoroughly tuned to one another to realize the advantages this transducer and receptor offer for any specific analyte. These QCMs have electrodes deposited on them. The deposited electrodes can vary in pattern and shape. Aside from being mass-sensitive, the QCM also effectively functions as a capacitor, with field lines penetrating the QCM. The exact shape of the field lines are influenced by the electrode designs, the group discovered previously. The field lines on partially covered QCM designs reach into the liquid of the analysed solution. If this has an influence on the measurement was questioned. [1] [2] [22]

In this work the influence of the QCM design on the measurements response and noise was researched. For this a new QCM electrode design and way to deposit this design on the QCM was developed and had to be optimized. Figure 2 shows what the analysed designs look like. To monitor the influence of the QCM designs, a QCM with a fully coated side and a partially coated design that only covers the electrodes were measured, characterised and compared. To do this a previously successful polymer/analyte pair, namely gold nanospheres and a methacrylic acid polymer, was polymerized on the created QCMs to see the influence different concentrations of the analyte had on the different QCMs as well as how the QCMs are influenced by the background during measurement. Another part of the thesis focuses on how the different ways of manufacturing the electrodes of the QCM influences the measurements. Atomic force microscopy (AFM) and scanning electron microscopy (SEM) were utilized to characterize the surface of the QCMs, to see whether the method was acceptable and the imprinting and re-binding processes were successful.

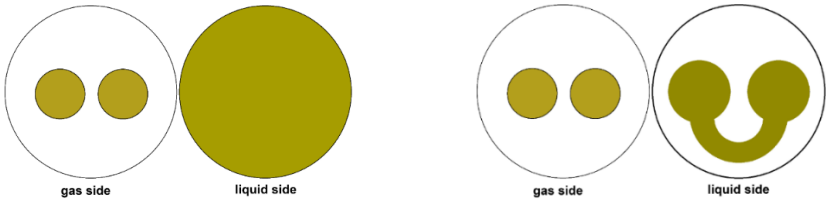

Figure 2: The two QCM designs that were compared in the research.

2. Theory

2.1. Quartz Crystal Microbalance QCM

The quartz crystal microbalance (QCM) is one of multiple types of acoustic transducers. Sensors are typically tuned to be very specific as well as sensitive to a target analyte, because in real on-field samples there are many other components that could disturb a measurement. The most common transducers are electrochemical, optical and acoustic transducers. QCMs belong to the acoustic transducers. The sensitivity and reliability of acoustic sensors is often close to classical analytical instruments such as a gas chromatograph, but only for one analyte. The main property measured by acoustic sensors is mass, which is a fundamental property of all molecules, making acoustic resonators universal transducers. The main advantage of acoustic sensors is that due to the universality, they allow for label-free measurements. A change in the important acoustoelectric parameters, such as resonance frequency or acoustic wave velocity of these acoustic wave devices, can be induced by anything that influences wave propagation or causes surface perturbations [1] [2]

2.1.1. Quartz Crystal Microbalance general

A QCM is a gravimetric sensor. Mass is one of the fundamental properties of an analyte, which means any analyte causes a signal on an acoustic transducer, i.e. they are inherently non-selective. Not only can mass be detected with QCM measurements, QCMs also allow for a rapid measurement, allowing for the monitoring of very subtle mass changes by tracking the frequency changes. Typically, when deposition on the sensor surface occurs, the resonance frequency of the QCM decreases. This effect is referred to as mass loading and was first described by Sauerbrey. Sometimes a positive frequency shift is observed at binding, which generally is attributed to loose coupling to the QCM surface. [1]

The QCM sensor is based on the piezoelectric effect. The piezoelectric effect only occurs in non-centrosymmetric crystals. It describes induction of an electric charge / electric polarization on a crystal surface when applying mechanical stress to the crystal. Under strain, deformation takes place, the atoms of the crystal are displaced and this displacement produces electric dipoles in the material. The piezoelectric effect also works inversely, as strain can be induced proportionally to an applied electric field. The inverse effect is referred to as the converse effect. Not all non-centrosymmetric crystals exhibit the piezoelectric effect. To find out if a material does exhibit the effect, it has to be determined experimentally. Most utilized materials that exhibit the piezoelectric effect are ceramics such as PZT. The application of piezoelectric materials often involves moving machines very subtly and the proportional strain of the piezoelectric materials allows for very miniscule controlled movements of a machine. Some naturally occurring crystals exhibit the effect, such as Rochelle salt and more importantly quartz. Quartz is the primary material used for QCMs. Whether synthetic or naturally occurring, piezoelectric materials have to be oriented and cut at specific crystallographic directions to obtain the best piezoelectric response. The AT-cut gives quartz excellent temperature stability at room temperature, because the frequency-temperature curve has an inflection point at 25°C, meaning the QCM is less influenced by the temperature near 25°C. This also gives the quartz a thickness shear mode of vibration and is usable between 0.5 and 30MHz. For the production of AT-cut quartz the crystal is cut at a 35° 15’ to the crystallographic Z axis (see Figure 3). The thickness shear mode of vibration is the reason that QCMs are very thin quartz wafers,

because higher frequency devices demand thinner quartz wafers and eventually make QCMs fragile and limit their possible applications. [1-5]

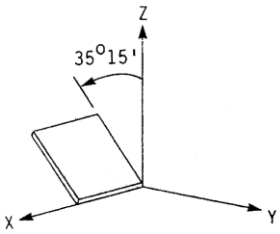

Figure 3: Quartz crystal AT-cut 35° 15' to Z axis [5]

2.1.2. Quartz crystal microbalance setup

A QCM comprises of a piezoelectric crystal plate with paired electrodes on both sides. Figure 4 shows the structure of a QCM. As the name implies the piezoelectric crystal is typically made from quartz (SiO_2). When an oscillating electric field is applied across the device, it induces an acoustic wave that travels throughout the crystal with a certain impedance depending on the applied frequency. At the resonance frequency the impedance is minimal and this minimal impedance is reached when the thickness of the QCM is a multiple of half the wavelength of the acoustic wave. For a QCM to function as a sensor, some form of coating is required to establish sensitivity and specificity. [1] [5]

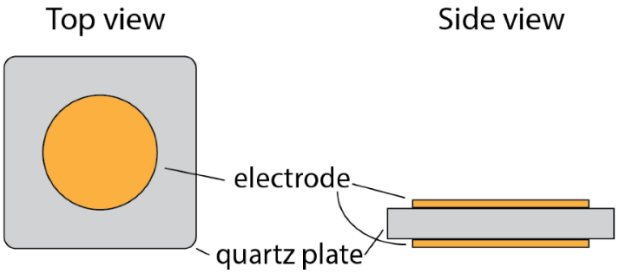

Figure 4: Basic structure of a QCM [24]

2.1.3. Quartz Crystal Microbalance Working principle

The QCM has a natural resonance frequency that depends on the cutting angle and the thickness of the quartz crystal. Any QCM also has a fundamental frequency that depends on mass, its chemical structure, its shape and its thickness. Figure 5 showcases the vibration of a QCM. Due to the thickness shear vibration of the QCM, the displacement is perpendicular to the quartz thickness with a maximum amplitude at the quartz plate surface.

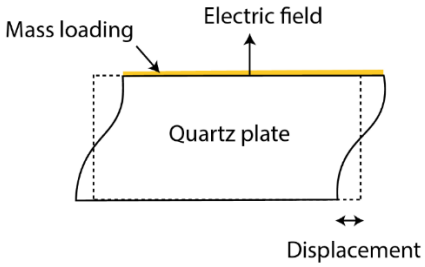

Figure 5: Thickness shear mode of vibration of a QCM [1]

Sauerbrey proved that changes in the resonance frequency are related to the mass that has accumulated on the crystal, but his research only focused on the QCMs in gas phase and it did not consider the viscosity of the medium and is therefore not applicable to liquid phase. For a more in-depth understanding of QCMs, various mathematical models are being utilized, but these are too complicated to go into detail here. The equation Sauerbrey developed is given below in Formula 1. Another point worth mentioning is that Sauerbrey equation is limited to rigid thin films that are firmly attached to the QCM electrode. At high mass loadings of more than 15% of the total QCM mass, a deviation of Sauerbreys equation does occur. Lu and Lewis derived a one-dimensional acoustic composite-resonator model that still works at high mass loading, but it is a lot more complicated, so unless high mass loading occurs the Sauerbrey equation is utilized. [1] [5]

$$\Delta f = -\frac{2f_0^2}{S_A\sqrt{\rho_q \mu_q}}\Delta m,$$

Formula 1: Sauerbrey equation combining the frequency change and the mass deposition. f_0…Resonance frequency of the fundamental mode, Δf…Frequency change, Δm…mass change, S_A… Electrode area, ρ_q…density of quartz, μ_q…Shear modulus of quartz for AT-cut crystal.

Gas phase QCM measurement was originally the only application possible, because in liquid phase the viscosity impeded the oscillation too strongly and hence its ability to maintain positive oscillation feedback. This issue was solved due to further research and the development of a more stable oscillator circuit, vector network analyzers and suitable QCM designs. Nowadays biological and chemical sensing in both liquid and gas phase is possible. [1] [5]

Kanzawa defined the QCM application in liquid phase and based his own equation on the vanishing shear wave into liquid. Figure 6 shows how a vibrational wave travels through liquid. Since in liquid there is coupling between the liquid layer and the crystal surface the frequency drastically changes compared to gas phase. This is because when the crystal oscillates in contact with a liquid, shear motion on the QCM surface generates plane-laminar flow in the liquid, which decreases the frequency proportionally to the viscosity and the density of the liquid. The distance the wave can travel into liquid before effectively disappearing is called the viscous penetration depth. It is defined as the maximum thickness of the liquid layer over the QCM that still influences the frequency shift. The further away from the QCM the wave travels through liquid, the further dampened the amplitude becomes until it effectively vanishes. A frequency change is caused by the viscosity or density change of the liquid layer itself. In practice this is not as simple. Sometimes the QCM resonance frequency can shift despite the perturbation being beyond the penetration depth. Kanzawa's research also did not consider film thickness, which influences QCM measurements. Since the penetration depth changes depending on the viscosity of the liquid, it also means that the oscillation frequency changes depending on the solvent used. [1] [5]

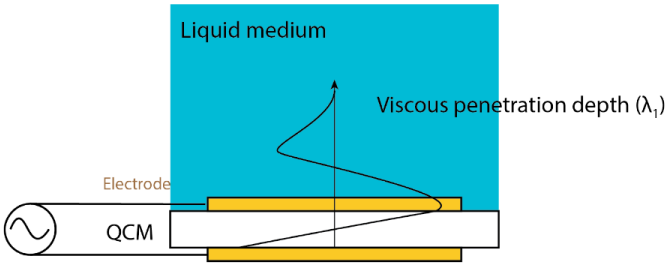

Figure 6: Penetration depth of QCM immersed in liquid medium [1]

To achieve resonant oscillation the piezoelectric crystal has to be in an oscillation circuit where the mechanical and electric oscillations are near the fundamental frequency of the crystal. For the actual QCM measurement there are different circuits that were developed as well as different measurement equipment. [1] [5]

Earlier it was mentioned that the film has an influence on the QCM measurement. Specifically, the sensor surface composition can quite strongly influence the results of a QCM measurement. A paper by Urbakh and Daikhin studied the influence of electrode surface roughness. In liquid the frequency does change depending on the surface roughness, because of inertial motion rigidly coupled to the surface and additional viscous energy dissipation induced by roughness. The liquid induced resonance shift of a QCM is basically the same for smooth surfaces, but for rough surfaces the resonance shift differs greatly. In general, if deviations occur from the theoretical predictions to the experimental results, it is often due to the neglect of microscopic properties of the interfaces with the surface roughness. Another effect of increased surface roughness is that the surface increases and additional mass of the solvent can be trapped in the cavities. So Urbakh and Daikhin concluded that the measurement of electrochemical oxidation can change the surface roughness and so influence the observed resonance frequency shift. [6] [7]

2.2. RAFT Polymerization

RAFT polymerization or reversible addition fragmentation chain transfer (RAFT) polymerization, is a very versatile polymerization technique that yields more controlled polymers. Radical polymerization is one of the most common methods for the production of high-weight-polymers and RAFT polymerization is a form of reversible deactivation radical polymerization (RDRP), which is a class of polymerization whose end product closely resembles the feature of living polymerization while still being and benefiting from being a form of radical polymerization. RDRP, and so RAFT as well, allows for synthesis of a polymer that has a more predictable molecular weight and so more uniform chain lengths, low molar mass dispersity, high end group fidelity and a capacity for continued chain growth. [8] [9]

The RDRP mechanism relies on an equilibrium between actively growing and dormant chains. Figure 7 showcases the basic RDRP mechanism. This can be achieved by two processes. The first of these processes is reversible activation, which relies on the persistent radical effect to keep the equilibrium. The second process is known as degenerative transfer and RAFT is one of its examples. There is the same number of radicals in the activation and deactivation steps in degenerative transfer systems as in regular radical polymerization. To acquire the radicals, same as in regular polymerization, some form of radical initiator has to be present. The key feature of RAFT polymerization is that a RAFT agent is mixed into the monomer solution that is capable of transferring the radical ends between polymer chains, which allows for a more even growth of the polymer chains instead of the commonly achieved few long polymer chains

with many very short chains. Essentially the fluctuations of polymer length are reduced significantly. To ensure that this happens, the rate of addition and fragmentation of the radical ends is higher than that of propagation making it so that each polymer chain is less likely to grow, but all of them are more likely to grow at the same rate. In practice it is aimed for less than one monomer unit added per activation cycle.

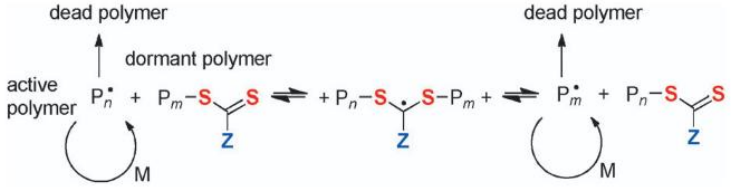

Figure 7: Mechanism of RDRP with the reversible activation and deactivation by degenerate chain transfer. [9]

A bimolecular termination, leads to dead chain ends and is irreversible in the system, but to ensure even growth with almost no dead chain ends, the likelihood of dead chain end terminations are calculated and controlled by adjusting the number of introduced radicals formed by initiators. If only the initiator concentration is lowered, it also lowers the polymerization rate, but other parameters also influence the polymerization rate, which are typically adjusted to keep the polymerization rate the same. A limitation of RAFT and RDRP in general is the limited range of molecular weights that are producible, while at the same time keeping control over dispersity and end-group functionality. Naturally, not every RAFT agent is suitable for every monomer, so the right RAFT agent has to be selected and tuned to the monomer. [8] [9]

2.3. Nanoparticles

Nanoparticles are very small materials ranging between 1 and 100nm. They find application in various fields of medicine, biotechnology, environmental applications and agriculture, because of better physiochemical properties compared to common bulk materials in certain applications. Only the surface of a material can interact with the environment, which is why nanoparticles, which have a very high proportion of particles at the surface, generally react stronger than bulk materials. Engineered nanoparticles (ENPs) show comparatively better magnetic, electrical, optical and thermal properties. But nanoparticles have upsides and downsides. The performance of ENPs is often really high, but the impact and control of the ENPs on the environment has to be studied. Typically, the main focus of ENPs studies is the study on the surface properties, as to assess and predict behavior of the ENPs on the environment. [10]

Outside influences such as pH, electrolytes or dissolved organic matter can greatly influence the behaviors of ENPs and change the interaction of ENPs with organisms or sensors. As the size of ENPs decreases and the surface increases, so generally increases the adsorption capacity. The higher surface areas drawback is that compared to bulk materials, nanoparticles weathering is increased and so their “lifetime” is significantly decreased. [10]

2.4. Scanning Electron Microscopy

Scanning electron microscopy (SEM) is a method to amplify small features of objects or living beings that are not visible with the human eye. Generally, a human eye can distinguish objects

smaller than 200µm, but that is not nearly enough to analyze and observe the microscopic world let alone the nanoscopic world.

For simple amplification typically optical microscopy (OM) is used. It utilizes light and lenses to focus in on a sample, meanwhile SEM is applying electron emissions to analyze a surface. The lenses of OM bend light to magnify the image, which can lead to a magnification of 400 to 1000 the original image sizes. This magnification may appear as good, but for chemical purposes and to resolve molecules, it is simply nowhere near sufficient. [11]

SEM provides a remedy for the limitations of OM and still maintains many of its upsides. SEM is an effective method that allows for the analysis of organic and inorganic samples on the nanometer scale, but it can also be used to analyze bigger samples on a micrometer scale. SEM uses an electron beam of high energy to scan a surface. Figure 8 features a schematic representation of an SEM. Essentially, secondary electrons and backscattered electrons from the surface are used to create an image. Since electrons are used to generate the image, the color of the sample is not maintained, instead the image is resolved in a greyscale of high resolution. Under an SEM it is possible to magnify surfaces to 300 000 times of its original size and in certain newer models a magnification of up to one million times has been achieved. At this magnification it is possible to distinguish features smaller than 1nm, which does enable us to observe smaller molecules. The ability of an SEM machine to distinguish fine details of a sample is determined by its spatial resolution. Often energy dispersive x-ray spectroscopy is applied together with SEM to achieve qualitative and semi-quantitative results. [11] [12]

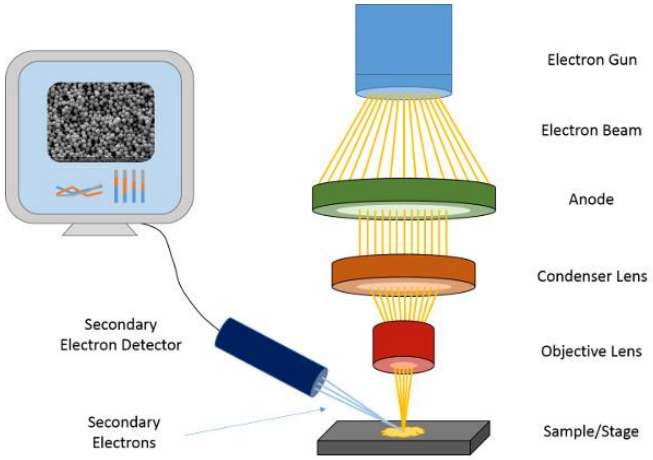

Figure 8: Schematic representation of how an SEM operates and its parts [13]

Normal field emission SEM is operated at ~25kV accelerating voltages normally achieve a resolution of 1nm. Despite all this the practical resolution limit is determined by the machine and its lens aberration and defects. [12]

Figure 9 shows a photo of the SEM setup. An SEM comprises of three major components, which are the electron column, the specimen chamber and the electronics control system including the computer.

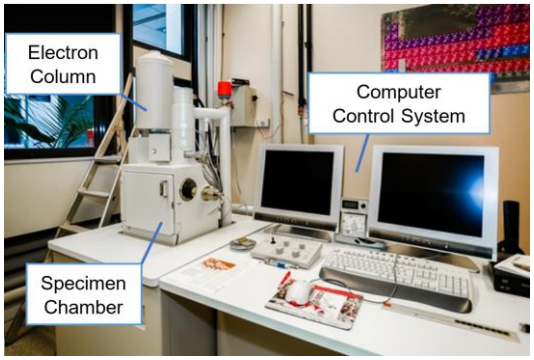

Figure 9: A photograph that shows the three major sections of the SEM: the electron column, the specimen chamber and the computer control system [14]

The most important component of the electron column is the electron gun, which generates an electron beam (see Figure 8). The electron gun is located in the upper section of the electron column and consists of a cathode and associated electrodes. The electrons are accelerated downward through the column by applying a potential difference and electromagnetic lenses positioned in the electron column to focus the electron beam with a diameter of a few nanometers onto a sample. When interacting with the sample, the electrons enter a few micrometers deep, which leads to different analyzable signals. Figure 10 shows those signals. The depth of penetration is dependent on the energy of the electron beam and the sample density and can range from 100nm to 5µm. The electrons penetrating the surface spread out in the form of a droplet into the sample. [12]

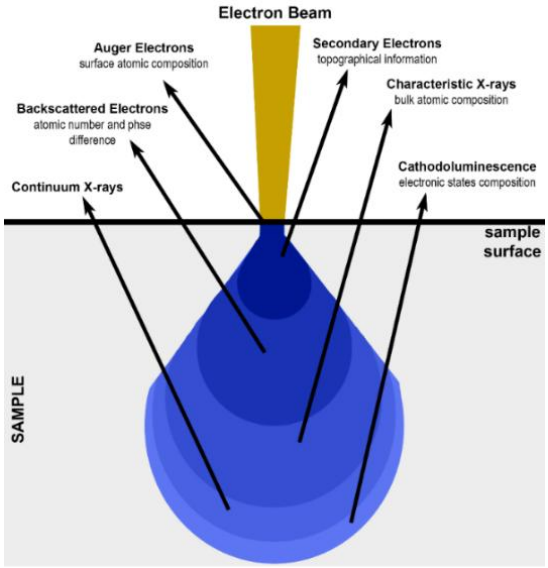

Figure 10: Different penetration depths of electrons and x-rays through a sample and what information can be derived from the different electrons / x-rays [15] [16]

Backscattered electrons, secondary electrons and x-rays can be produced from the interaction of the electron beam with the sample and these signals are collected and interpreted by the machine to generate an image of the sample surface as well as the elemental composition. To prevent any scattering of the electrons due to collision of the electrons with other particles, ultra high vacuum is established in the entire electron column and specimen chamber. [12]

SEM is very useful to analyze surfaces. It is capable of observing and imaging the surface details of a variety of different materials. Among these materials are metals, ceramics, alloys, polymers, minerals, corrosion deposits, membranes, filters, biological samples and others.

Furthermore, all types of samples are accessible by SEM, whether they are conductive or non-conductive, solid or powdered, wet or dry. [12]

There are limitations to SEM where other techniques have to be applied. Such limitations include that sample size is limited, the samples themselves have to be solid, the instrument is quite big, non-conductive samples need to be coated, samples need to be examined in vacuum. [12]

2.5. Atomic Force Microscopy AFM

Atomic force microscopy (AFM), similar to SEM, is a method to magnify and image surfaces to yield information about nanoscale features of a sample. AFM is also often referred to as scanning force microscopy SFM, but in this thesis it will only be referred to as AFM. The method is classified as one of the different methods of so-called scanning probe microscopy (SPM). Scanning probe microscopy is an umbrella term spanning multiple different methods that analyze the topographical features of a sample on the nanoscale utilizing a probe often referred to as a tip. SPM methods analyze and characterize the surface of a sample by raster scanning it. This means one position of the sample is measured, before moving on to the next one, once a defined row is fully measured, the device moves on to the next one. [17] [18]

The AFM essentially consists of five important components (see Figure 12). These are the sample surface, the height regulator, the cantilever with tip, the laser and the detector. In AFM the atomic force between the tip and the sample is measured. The force between the tip and sample can be shown as a function of the tip sample distance. Figure 11 shows a typical force-distance curve.

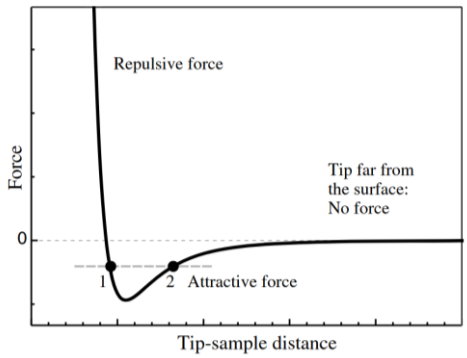

Figure 11: The qualitative behavior of the force between the AFM tip and the sample surface as a function of the tip-sample surface [19]

In the force/distance diagram, three distinct regimes can be observed. If the tip is far away from the surface, the measured force between tip and sample is negligible. If the distance of the sample and tip becomes too small, a strong repulsive force is observed. If the sample and tip distances are in a certain range between being too close and too far away, a non-negligible attractive force occurs. AFM is mostly performed in one of four modes. The modes are separated via 2 categories. First the mode of operation, which separates them into static (non-oscillating) and dynamic (oscillating) and secondly into the type of interaction probed, which are repulsive (contact) or attractive (non-contact).

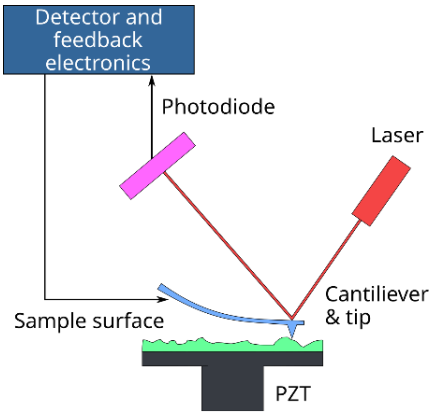

Figure 12: schematic representation of how an AFM operates.[20]

Figure 12 showcases a schematic representation of an AFM. The force between sample and tip can be recorded with deflection of a cuboid shaped flat spring with the sharp tip at its end, known as the cantilever. With the known stiffness of the cantilever, it is possible to measure the force between tip and sample, by measuring the bending of the cantilever. Often cantilever bending is determined by reflecting the light emitted from a laser diode onto multisegment photo diode (2 or 4 segments). If the laser light is deflected outside a defined range, the feedback loop will automatically adjust the tip position in z-direction to maintain an adequate measurement. The changes in the z-position, correspond to topography. [19]

The tip height is very precisely measured and changed with actuators that implement an application of the piezoelectric effect (more details regarding the piezoelectric effect are located in the theory chapter on QCMs). The application of a fine charge on a piezoelectric material induces a mechanical deformation and this allows for very precise height adjustments. [19]

Vibrations can have a large influence on the image quality, because the tip-sample distance is attempted to be kept stable and vibrations distort that. Outer vibrations can be effectively reduced by the application of a spring suspension. Meanwhile the microscope is an oscillating system itself, since the tip and sample oscillate against each other. This leads to vibrations, which are tried to be minimized by making the microscope very rigid. So external and internal vibrational shielding are utilized to minimize all these adverse effects. [19]

The principle behind AFM is to use the measured force between tip and sample to acquire information about the surface topography. There are various forces acting between the tip and sample. One of the major long-range forces is the van der Waals force. Among long range forces, influencing the tip and sample, the vdW force is the strongest at distances larger than 1nm. Short range interactions can be repulsive or attractive, depending on whether the overlap of the electron wave functions of the outer shell reduce the total energy (attractive) or not (repulsive). For simplicity the Lennard-Jones potential (see Figure 13) is meant to describe the interaction between neutral atoms, but it also describes the tip-sample interaction quite well.

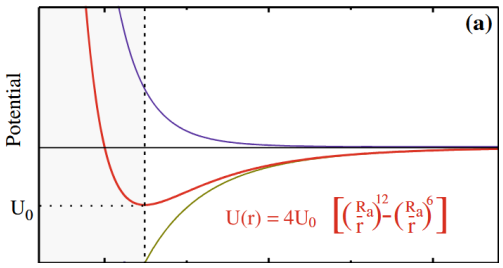

Figure 13: Lennard-Jones potential [19]

Electrostatic interaction between tip and sample also occurs, if there are static electric charges trapped on the tip or sample or if both are conductive and are set at different potentials. These forces are rather long range, rather strong and can therefore disturb the measurement, but they are easily eliminated by applying a bias voltage. [19]

2.5.1. Static Atomic Force Microscopy

In static AFM a cantilever is deflected by the force between the tip and sample. The deflection can be described by Hooke's law, which describes that the force necessary to compress or pull apart a spring has a linear correlation to the distance. Instead of there being a spring in static AFM, Hooke's law is used to describe the cantilever bending. [19] [21]

In the static mode, the surface topography is recorded and mapped during a scan, by changing the z-position of the tip or sample in a way that the tip-sample force is kept at a constant value. In this mode the tip is in direct contact with the sample. If the measurement is performed in the repulsive regime it is referred to as the contact mode. Typically, the force and therefore the distance between surface and sample is kept constant during measurement.

A schematic illustration of the contact mode and the following tapping mode are visible in Figure 14. In contact mode specifically, the tip is directly in contact with the sample and strong repulsive forces act between them. This can damage the surface and tip, but to reduce wear down, the cantilever is soft. If soft surfaces are analyzed it can still lead to damaging of the sample, so those are mostly analyzed with the dynamic modes. The total tip-sample force is given by a summation of forces. AFM can be influenced by various phenomena that deteriorate image quality. In contact mode it is possible that the attractive forces close to the surface can be strong enough to pull in the tip, when a certain distance is reached where the force gradient of the tip-sample interaction becomes larger than the cantilevers spring constant. That is why contact AFM is typically done in the repulsive regime to avoid this snap-to-contact phenomenon. Snap-to-contact can also be avoided by using stiff cantilevers. [19]

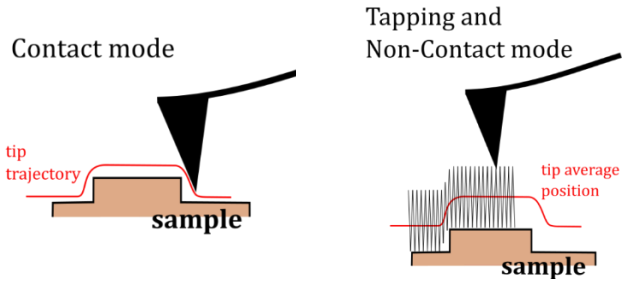

Figure 14: A schematic representation of (left) the contact mode AFM and (right) tapping mode AFM. [22]

2.5.2. Dynamic Atomic force microscopy

In dynamic AFM the cantilever is being excited over the surface very closely to the resonance frequency of the free cantilever. The actual frequency of the cantilever is referred to as the driving frequency. Due to the interaction of the tip and the surface is the resonance frequency of the cantilever being modulated. The resonance frequency is generally being changed to lower frequencies due to attractive tip-sample forces and to higher frequencies due to repulsive forces. In the dynamic mode the cantilever is excited at or close to its own free resonance frequency. At this frequency if the tip approaches the sample surface, the interaction between tip and sample leads to changes in the resonance frequency of the cantilever and a change in

the amplitude of the cantilever. This change in amplitude is used for the detection as the signal for the feedback to regulate the tip-sample distance. [19]

Tapping mode or Intermittent Contact mode

The tapping mode is also often referred to as intermittent contact mode. The tapping mode is the most commonly used mode in ambient conditions. The distinguishing factor of the tapping mode is that when the cantilever is oscillating, the tip makes contact with the surface intermittently. As a part of the dynamic AFM modes, in this mode the cantilever is excited at a fixed driving frequency very closely to the resonance frequency and the oscillation amplitude is being measured. This information is fed back to the controller electronics to maintain intermittent contact. The amplitude is dependent solely on tip-sample distance, which bypasses instabilities resulting from the feedback control of the tip-sample distance. This leads to a clearly measurable feedback signal. [19]

A great advantage of the tapping mode is that the scan speed is as high as that of the non-contact mode, while also not having much contact with the surface so that the lateral forces between tip and sample do not damage the surface. Hence, with tapping mode it is possible to analyze soft samples such as cells with high resolution. Furthermore, the tip is not as easily worn down as with the contact mode. The very brief contact prevents a pulling of the sample sideways due to shear forces. Another advantage is that the method avoids snap to contact. But, the biggest advantage of the tapping mode relates to the contamination layer of mostly water on the surface resulting from humidity in the air onto the tip and surface. A thin liquid layer can form on the sample and tip that can cause substantial problems for measurements in the non-contact mode and contact mode, because the properties of the actual surface are being masked. The advantage of the tapping mode is that the tip just passes through the contamination layer and interacts with the actual surface. [19]

2.6. Molecularly imprinted Polymers (MIP)

Molecular imprinting is a technique to generate tailor-made binding sites in a polymer. These are referred to as cavities. They are specifically tuned to a certain analyte also referred to as the target molecule and the binding and separation are tailored to the template molecules specific shape, size and functional groups.

The technique is also described as a method for producing surfaces with specific locks matching a molecular key. These created cavities act as an artificial recognition site for a certain molecule in polymer matrices also referred to as the substrate. Molecular imprinting is a technique used mainly for analysis. The technique is very useful for analysis due to its simplicity, specificity and its relatively low cost. [23]

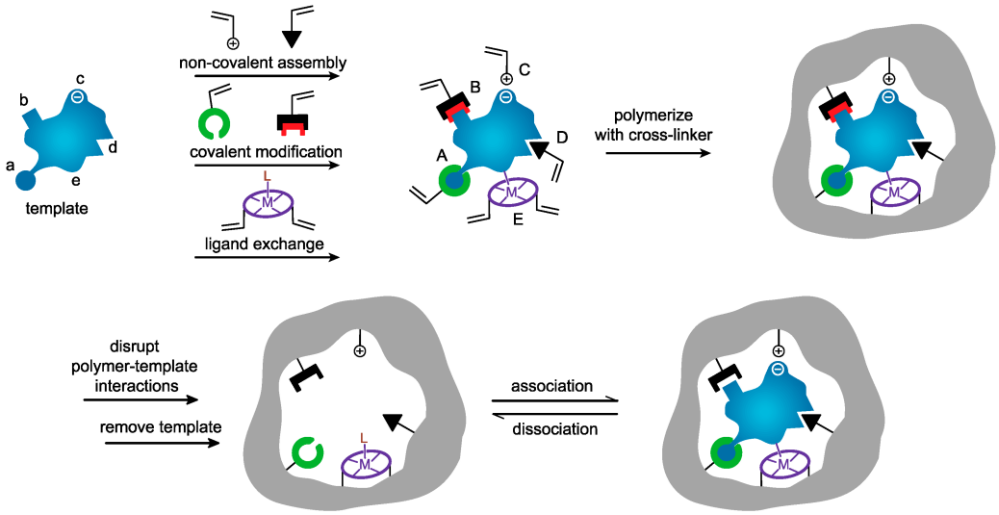

Figure 15: Schematic of the molecular imprinting process. It shows the pre-formation of the template molecules and the complex before polymerization. After polymerization the template is removed and the polymer can be used for detection/trapping. In the first step it also shows the different possible interactions that can be utilized for imprinting. [24]

Figure 15 showcases a schematic representation of the procedure. Molecularly imprinted polymers are also referred to as MIPs and non-imprinted polymers are referred to as NIPs. MIPs are produced by co-polymerizing functional monomers with cross linkers in the presence of template molecules. Due to the crosslinker, the mechanical properties of the polymer change, generally making them more structurally sturdy. Without the 3D connections between monomers introduced by the crosslinker, most of the cavities would collapse upon removal of the template molecules. Typically, before the polymerization the template molecules and functionalized monomers pre-form a complex due to covalent, non covalent or semi-covalent interactions. [23]

Various types of molecular imprinting are being performed such as bulk imprinting, surface imprinting and epitope imprinting. Each of these is used depending on the necessary polymer conditions and analytes. Figure 16 shows a schematic representation of bulk imprinting. Here, the template molecules are fully imprinted into the polymer matrix. After polymerization is completed, they need to be removed from the formed cavities inside the polymer. Bulk imprinting is only preferred for the imprinting of small molecules, since the adsorption and release of the template molecules is generally a lot faster and reversible, which makes the created polymers reusable for multiple analyses. If bigger molecules are bulk imprinted, it becomes a major hurdle to remove them from the polymer for reasons of steric hindrance and diffusion. Another drawback for bigger molecules would be that the created cavities are large enough that smaller molecules could diffuse into them, which hinders the diffusion into the cavity of the target molecule. Bigger cavities also are more easily cross-reactive and less selective than smaller ones, for example if the bigger molecule were to be a protein, it is easy for smaller peptides to diffuse into the created cavity and lead to a signal. [23] [25]

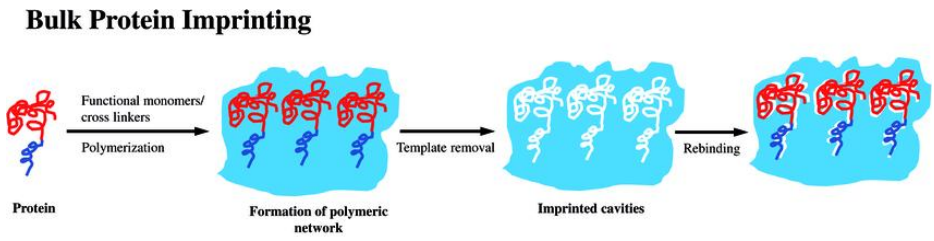

Figure 16: schematic representation of bulk imprinting [26]

Typically, molecular imprinting involves the formation of a pre-formed complex between the template molecules and its complementary functionalized monomer after which the polymerization is started with crosslinkers and initiators present. After the MIP formation the template molecules are removed with the help of eluents. There are two main approaches to produce MIPs. These are covalent imprinting and non-covalent imprinting, which are visualized in Figure 15. There are also multiple derivatives of these two main approaches.

For the covalent imprinting technique, prior to polymerization the template-monomer complex forms by establishing actual reversible covalent bonds. The established bond types are often Schiff base bonds, ketals, acetal bonds or boronic ester bonds since they are relatively easy to break. Since the energy required for breaking covalent bonds is high, it also means that strong chemical interaction is necessary to extract the template molecules. The fact that strong interaction between the template and substrate exists also means the cavities are well tuned to the target molecules. This leads to one of the biggest advantages of covalent imprinting, which is that polymers are being prepared with binding groups in the cavities at specific spots. This greatly reduces non-specific interaction and increases selectivity. Due to the high stability of the complexes during polymerization, polymer networks are being formed that show a very homogenous binding site distribution with high selectivity. One of the biggest problems of this technique is that covalent imprinting is limited to only a certain number of accessible functional monomers existing. Another demerit is that higher effort and therefore cost is necessary for covalent imprinting, since the template-monomer complex has to be synthesized beforehand. [23] [27]

In contrast the non-covalent imprinting approach is based on non-covalent interactions between the template and the polymer network, such as van der Waals forces, hydrogen bonds, dipole-dipole interactions, ion-dipole interactions, π-π interactions etc. Due to the interactions only being non-covalent, it also means the energy required to break them is far lower than that of covalent bonds and hence the removal of the template is easier than for covalent imprinting. The effort required to build these bonds is also far lower, so the complex does not have to be pre-formed before polymerization. Since the recognition is based upon non-covalent interactions, it is way more likely that a molecule that is not the target molecule, interacts with the interaction sites in the cavity. This means the selectivity is lower than for covalent imprinting. The cavities are also way less homogenous compared to the covalent imprinting, which also makes false positive interactions more likely. [27]

2.7. Physical Vapor Deposition PVD

Physical vapor deposition (PVD) is a method utilized to create thin films and coatings on substrates. In this technique, under a vacuum, a solid material is being brought into gas-phase and transferred to a substrate, which is then coated in the material. PVD does not include a chemical reaction between the substrate and the substrate, since that would fall under the chemical vapor deposition (CVD). In CVD the composition of the source and the deposited film are different due to a reaction, whereas the composition of the source and deposited film are fundamentally the same when it comes to PVD. There are combinations of PVD and CVD, making a strict separation of the methods by reaction difficult. In PVD the coating material is only brought into gas phase by physical means. There are various types of PVD, which mostly differ by the way in which the coating material is brought into gas phase, such as thermal evaporation, sputtering, pulsed laser deposition and others. Since PVD is used to create thin films, it is mostly used to manufacture semiconductors or sensors. While there is no rigid definition of what “thin film” means, it is generally understood that at least one dimension is small. Thin films are of interest, because they can produce properties in a material, that are

normally conflicting to the bulk properties. In the case of QCM sensors, thin gold films are applied, to create conductive electrodes on the surface. The actual microstructure of the film is influenced by various factors, such as the mechanism of nucleation, mechanism of growth, composition, effect of buffer layers, temperature etc. Essentially all PVD are being performed under vacuum, since it allows for a better control of growth and properties. The exact vacuum conditions depend on the individual device and the substrate, but generally higher vacuum has the benefit of having fewer contaminants in gas phase that could possibly interfere with the production of an even film and therefore leads to more reproducible film properties. The growth rate is kept rather low to improve control of film growth and reproducibility. One problem of PVD is that it is not possible to only coat the substrate, instead to an extent a film will be deposited onto the entire chamber. [28]

There are multiple techniques that were developed to bring the source directly into gas phase. The most widely employed technique is the thermal evaporation, in which the solid source is simply heated up with a resistive heat source to induce evaporation. This is performed in a vacuum chamber to create vapor pressure. The evaporated material is transported to the source and coats the substrate. The heat source can be electric or sometimes a laser. The biggest advantages of thermal evaporation compared to the other techniques is the simplicity, the reproducibility and the minimal contamination of the method.

Another widely utilized way to bring atoms into gas phase in PVD is sputtering. It is used to bypass energetic limitations that some materials pose for bringing the material into gas phase. For sputtering, the target material is used as a cathode and the substrate as an anode. A small amount of argon is brought into the chamber and an argon plasma is ignited above the target material. The positive argon ions Ar^+ are accelerated towards the target and crash into it. This collision, ejects some atoms from the solid target into gas phase. The ejected atoms now deposit onto the chamber and substrate. The electrons formed in the argon ignition are accelerated to the substrate, but their energy is not high enough to have the same effect as the Ar^+ ions. The mechanism of sputtering can be easily understood by two theoretical models, the bombardment of high energy particles generates enough heat to vaporize the solid target, as well as some of the kinetic energy the Ar^+ ions have is transferred to the surface atoms. Since this method requires the target to be conductive, it is only applicable for metals. Very thin films can be manufactured by utilizing direct current sputtering. [29]

2.8. Plasma Cleaner

There are various forms of cleaning a surface, such as via solvents, thermal heating and ion bombardment. Each method has advantages and disadvantages While solvent cleaning has the greatest range of utility, it is also limited in the sense that the solvents themselves often function as contaminants. Cleaning by thermal heating is really useful if applicable, but it is limited by the temperature limits of the surfaces. Ion bombardment with plasma allows cleaning, where the plasma energy is a lot higher than what can be achieved thermally without exceeding the temperature limits. For this process a plasma is created above the surface, which has such high energy it ionizes the organic contaminants, by breaking the organic bonds and removes them from the surface. Different than regular solvent cleaning, Plasma cleaning does not leave any residues behind and does not require the handling of potentially harmful chemicals. [30] [31]

The plasma cleaning process, takes place at very low pressure. Following this a process gas is led into plasma chamber. The gas is broken down and ionized creating the plasma. The highly reactive plasma starts to interact and break down the contaminants on the surface. The residues will be vaporized into gas phase and removed by the vacuum pump. Typically, an argon, oxygen or hydrogen plasma is utilized for the plasma cleaner. [30 - 32]

3. Experimental Section

The goal of this thesis is to compare different QCM designs regarding their properties in sensing. For this it focuses on two main aspects, that were explored, which are the production of the QCM designs and the following measurement for ultimate comparison of the different designs.

3.1. QCM Manufacturing

3.1.1. QCM designs

For the comparison a prior successful QCM comprising methacrylic acid polymer and gold nanoparticles (AuNP) was used. For the measurement, the QCM side with the imprinted polymer is in a liquid environment to allow target molecules to diffuse into the cavities. To compare if a fully coated liquid side of the QCM had an influence on the QCM measurements or if only the electrodes needed to align, a very simple design was conceived that basically only covers the electrodes and establishes contact to the external power circuit. Figure 17 and Figure 18 shows the QCM designs.

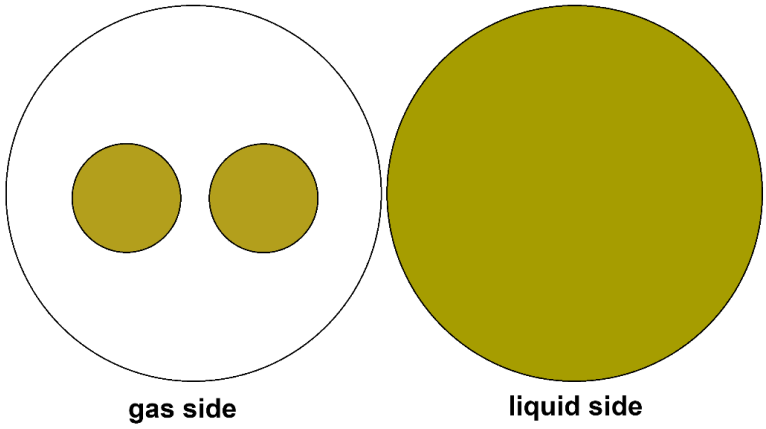

Figure 17: QCM design setup Nr.1. The fully coated (FC) QCM design. (left) The gas side of the QCM with only the screen-printed electrodes. (right) The liquid side of the QCM is fully covered with gold. That side comprises the MIP.

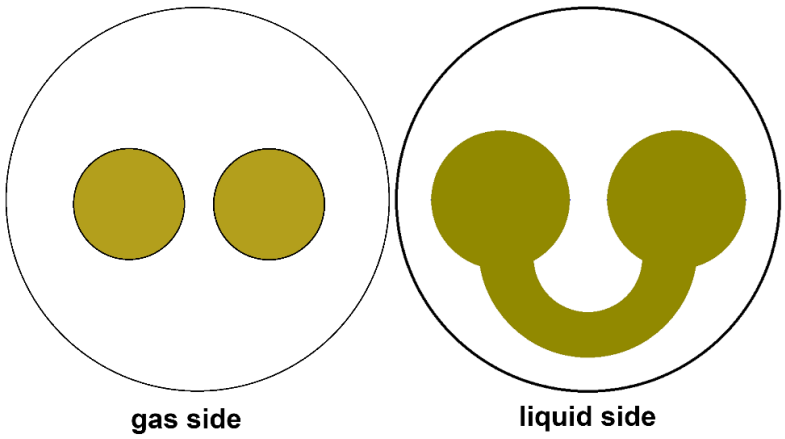

Figure 18: QCM design setup Nr.2. The partially coated (PC) QCM design (left) The gas side of the QCM with only the screen-printed electrodes. (right) The liquid side of the QCM is only partially covered with a bridge connecting the two electrodes contacting them to the external oscillator circuit.

To produce QCMs, quartz disks (Diameter 13.8mm, 168µm thick) were purchased from Roditi Inc, London. The electrodes on the gas side of the QCM follow the same design in both cases with the electrodes having a diameter of 4mm and spaced at a distance of 1.8mm. In Figure 19 the QCM design of the liquid side is shown with size markers to visualize the dimensions. For the partially covered design the electrodes on the liquid side were made larger to 5mm to more easily align the electrodes on both sides, but the distance remained 1.8mm. For constructing the bridge, from the center point of the QCM it was offset 1mm to get to the center point of the bridge. From this new bridge center point the radius of both edges are 4.5mm and 2.5 mm, which makes the bridge a 2mm wide.

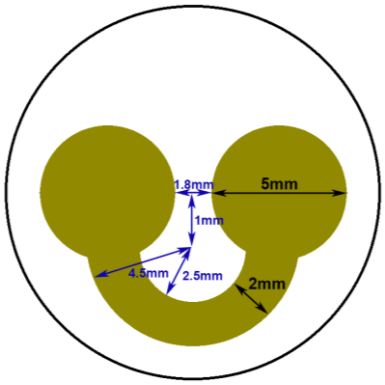

Figure 19: The partially covered QCM design with all design elements sizes (black) and the lengths of design elements only necessary for the production (blue).

3.1.2. QCM electrode manufacturing

To produce these two QCM designs, multiple strategies were employed and compared. For the gas side on both QCM designs, screen printing of a gold paste, followed by hardening the paste in the oven was employed. To produce the different designs of the liquid side, four different strategies were employed.

Screen printing

Screen printing served to produce the electrodes of all QCMs on the gas side and for comparisons sake for the partially covered QCMs liquid side.

In the first step, sieves were produced by printing the QCM designs shown in Figure 18 on a UV-permeable foil and placing them on a UV light. To prepare the sieve, artificial silk was glued on a metal frame under strain to keep the fabric stretched. The silk of the frame was then treated with a photo resistant lacquer (Azocol Poly-Plus S, KIWO). It was made sure all holes in the textile were covered in the lacquer by dispersing and spreading it rigorously. After applying the lacquer, the sieve was left in the dark to dry for 40 minutes. To ultimately harden the lacquer, the sieve was placed under a UV lamp for 30 seconds, with the earlier prepared electrode mask blocking hardening in the printed sections. Following this, the non-hardened parts were washed off with water. After blowing dry, the sieves remained open in the non hardened areas. In Figure 20 the sieves with various used designs are shown.

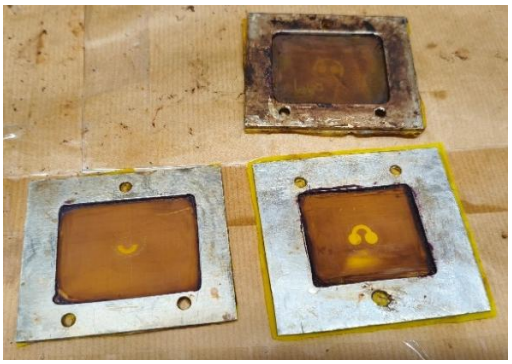

Figure 20: Metal frames with sieves used for screen printing

With the sieve completed it was possible to screen print electrodes on the quartz plates. Figure 21 visualizes the process of screen printing. To achieve this, a quartz plate was placed onto a socket with a hole connected to a vacuum pump. The vacuum was initiated to fix the quartz plate on the socket. The sieve with the desired pattern was placed on top of the quartz plate, gold paste was pressed through the sieve and smoothed out before removal. After the sieve was removed, the quartz plate was released and then baked in the oven at 400°C for four hours in a bake stand.

Typically, this was the only procedure, but for QCMs containing screen printed electrodes on both sides, the procedure was adjusted. The electrodes of the gas side were screen printed first and baked in the oven at 200° for two hours to ensure drying of the paste. Then, the quartz plate was removed from the oven and the electrode pattern of the other side was screen printed on the quartz plate and baked at 400°C for four hours. The reason for the different temperatures and times lies in the fact that for each time and the quartz plate is heated up and cooled down, there is a possibility of stress building up in the quartz, which can lead to fragility and breaking. This strain is increased with temperature.

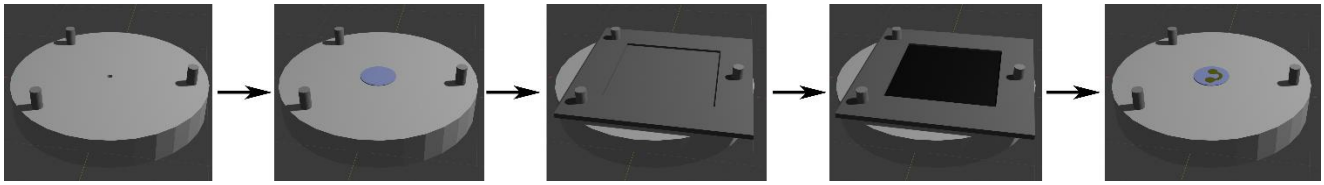

Figure 21: schematic representation of the screen-printing procedure (1) setup (2) QCM fixed in place (3) sieve placed on top (4) gold paste spread evenly (5) removed sieve

QCM parasol foil PVD masks

For the PVD deposition of the partially covered QCMs, masks had to be produced to ensure deposition of correct pattern. In Figure 22 some of these masks on quartz plates are shown. One method was to apply parasol foil. To prepare these masks, the designs were pre-drawn on the sticky foil with rulers and then stamped out with a 5mm and 9mm stencil respectively. These masks were then placed on the QCMs before PVD see the following section. These masks were quite irregular, because they were made by hand.

Furthermore, some masks prepared to contain the whole design, while others only comprised the electrode structures. QCMs prepared with the latter technique required to screen-print the bridge between the electrodes afterwards.

Figure 22: QCMs on the PVD deposition plate with parasol foil masks

3D-printed PVD masks

To bypass the limitations of screen printing and parasol masks and to produce partially covered QCMs with an even surface as well as a highly reproducible electrode pattern, 3D-printed masks were developed.

For the entire development cycle of the 3D-printed QCM masks, two different filaments were used, due to the availability at the university, namely polylactic acid (PLA) (see Figure 92) and copolyester (CPE) by Ultimaker. Because of trade secrets the exact composition of CPE is unknown. Both types of filaments did not melt in the PVD machine, which means in practical use any of them would work as a mask material. [38]

To produce the 3D printed masks, various designs were designed in the program “Autodesk fusion 360”. The different designs as well as their advantages and problems are discussed in the results section of the thesis. Some of the 3D printed mask designs were compared by light microscopy (Nikon Eclipse Lv100 H600L) to see which QCMs were better suited for the application, by analyzing the edges of the QCM electrodes. A QCM measurement comparison of the QCMs produced by the final few mask designs was performed. The used light microscope is shown in Figure 23.

Figure 23: Light microscope

The final design of the masks is visible in Figure 24. This design consists of a top part with a clip holder, a mask to clip in with the desired pattern, the quartz plate, a protective disk to prevent any deposition on the QCMs gas side, a PDMS disk to dispense the pressure in the design to not break the QCM, a bottom part to keep everything pressed together and cylinders that functioned as the locks of the hinges from the top and back part.

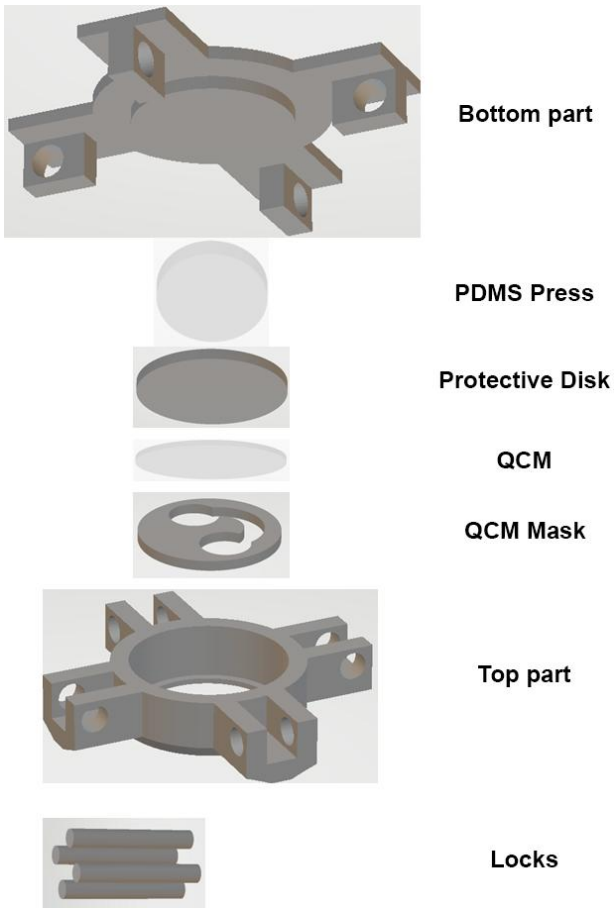

Figure 24: Final design of the QCM masks

Polydimethylsiloxane (PDMS) had to be prepared for the PDMS press in the mask design. The ratio between the curing agent and silicone was chosen at 1:10. For producing the silicone and curing agent were combined and mixed. After which the curing PDMS was evacuated to remove any bubbles. Following this the PDMS was left to cure in a petri dish until solidified. It was aimed for a height of the press between 2.5mm to 3.5mm. After curing was completed, the PDMS presses were stamped out since no specific radius was required.

For depositing electrodes on the QCM, the quartz disks were placed inside the masks, followed by PVD of the electrodes. The electrodes are made from gold, which requires depositing an interlayer of chromium to generate stable gold layers on quartz. To deposit, a batch of quartz plates was placed on a plate with a sticky foil to hold them. The PVD apparatus and sample plate are shown in Figure 25. Inside the machine the QCMs are flipped upside down and rotated during deposition. Then a 30nm film of chromium was sputtered followed by 50nm gold, which was deposited via thermal evaporation. After deposition the QCMs were cleaned via the internal plasma cleaner, removed from the machine and kept in an oven for two hours at 200°C.

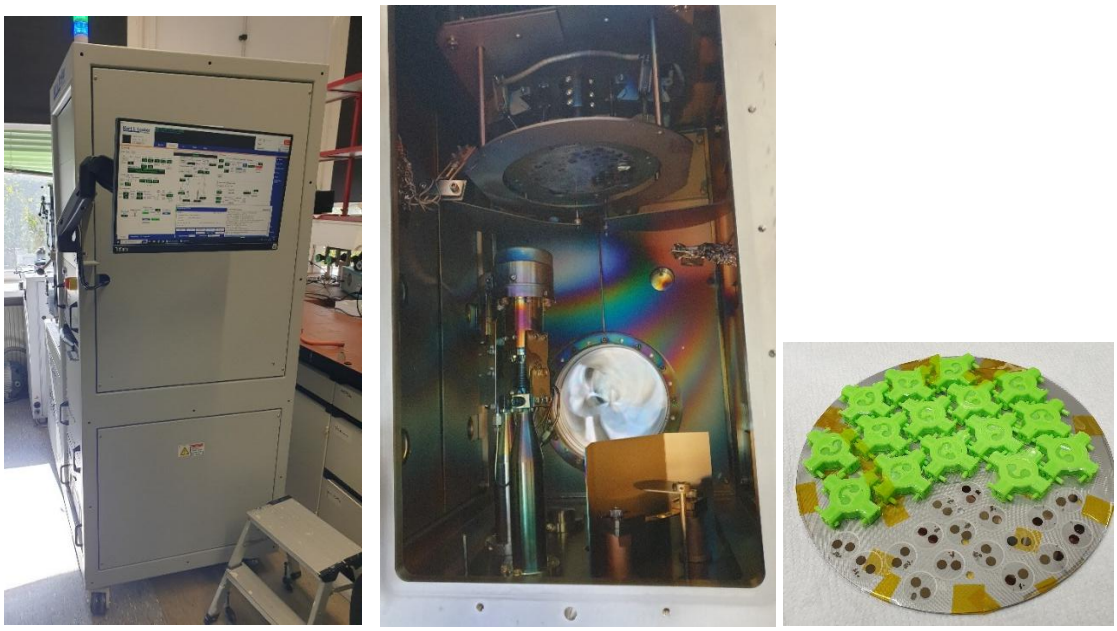

Figure 25: PVD machine (left) outside of machine (middle) sample chamber (right) PVD sample plate with QCMs before deposition

Fully coated QCM electrode production.

The fully metalized gold electrodes resulted from the same process, but without using masks. Differently than with the partially covered QCMs, the electrodes of the gas side were screen printed on before PVD.

3.2. QCM characterization, functionalization and measurements

3.2.1. Polymerization on the liquid side electrodes

In situ polymerization was performed on the liquid electrode surfaces in PBS buffer (Phosphate buffered saline) at pH=7.4. PBS is composed of 8g/l NaCl, 0.2g/l KCl, 0.2g/l KH_2PO_4 and 1.15g/l Na_2HPO_4. Pre-made PBS tablets (TH.GEYER BIOSOLUTE PBS) were dissolved in MilliQ water, the pH measured and if outside of pH 7.2 – 7.6, NaOH (0.1M) was added until the pH was in that range. Then the PBS was filled up to the required level.

Synthesis of MIP and NIP layers typically lasted three days, with batches consisting of 4-8 QCMs, with half being MIPs and the others being NIPs.

All QCMs were cleaned by sonication in an ultrasonic cleaner with ethanol for five minutes. After letting them dry, were the QCMs placed in plasma cleaner (Plasma Surface Technology Zepto Plasma Cleaner with a Balcers TCP-015 Vacuum Pump) and cleaned for 10min at 10^{-3} bar for the purpose of remove organic rests. For each produced QCM 2.5 ml 100% ethanol were mixed with 0.75mg 16-mercaptohexadecanoic acid (16-MHDA), the QCMs were placed in the solution and left to functionalize overnight in the fridge. Figure 26 shows the adsorption of 16-MHDA. All chemical structures for chemicals used in this experimental section are shown in the list of chemical structures at the end. [33 - 35]

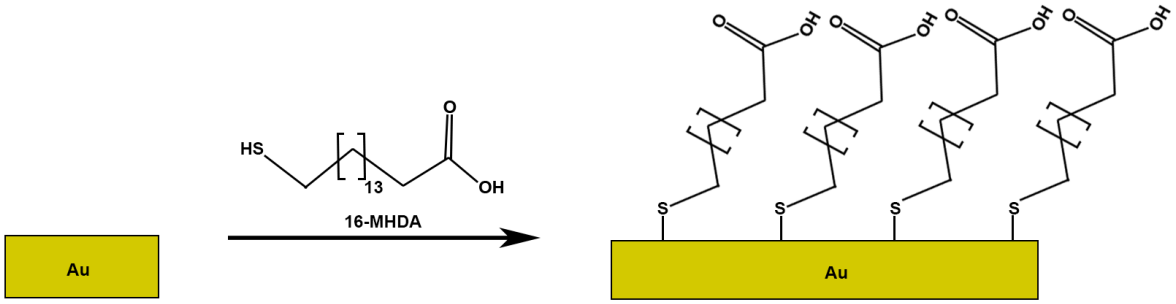

Figure 26: Reaction between 16-MHDA and a gold surface [34]

On the next day the QCMs were sonicated two times in ethanol and distilled water each. Meanwhile for each QCM 135.5mg 2,2'-Azobis(2-amidinopropane) dihydrochloride (abbreviated AAPH) were combined with 25mg N-Hydroxysuccinimide (NHS) and 29mg 1-Ethyl-3-(3-dimethylaminopropyl)carbodiimide (EDC) in 2,5ml PBS buffer and mixed until fully dissolved (5-10minutes). The washed QCMs were left to functionalize in the mixture for three hours in the dark. Gas bubbles formed in the solution, which disturbs functionalization, so they had to be removed. In the reaction (see Figure 27) the carboxylic acid activation is initiated at the acidic group of 16-MHDA, an NHS ester is substituted by reaction with NHS and finally the NHS is replaced by coupling with the NH_2 containing AAPH. To stop the functionalization after three hours, were the QCMs placed in the fridge overnight. [36] [37]

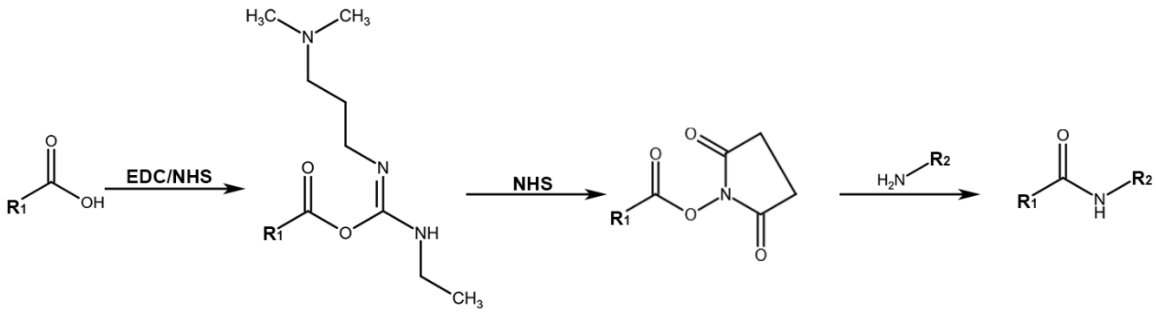

Figure 27: EDC/NHS activation/reaction scheme. (1) Carboxylic acid activation by NHS/EDC (2)conversion to NHS-ester and the following (3) coupling with NH_2 containing biomolecule (like AAPH) [36] [37]

A gold nanoparticle solution was prepared for the MIP. To produce them for each imprinted QCM that was prepared, 1.5 mg 16-MHDA were dissolved in 5ml ethanol. 100µl of a AuNP solution (75 nm Gold Nanospheres, PVP, Econix) were added. The mixture was then stirred in the dark until a light purple color emerged (2-3 hours), before placing it in the fridge overnight. In Figure 28 the reaction is shown. The reaction replaces the PVP shell that already occupied the AuNPs with 16-MHDA.

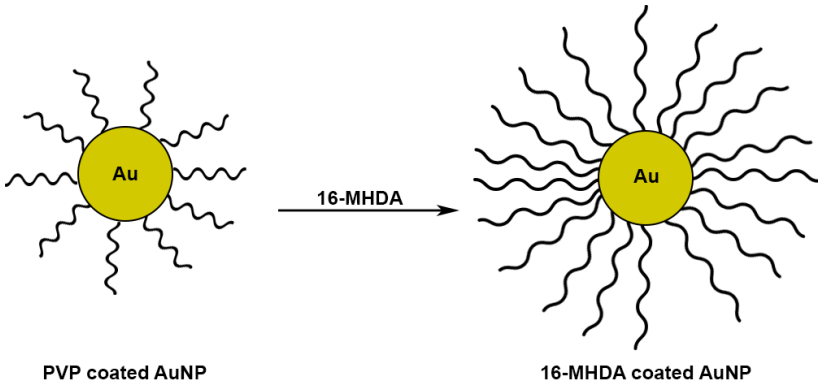

Figure 28: schematic representation of the AuNP shell change from PVP to 16-MHDA [34]

After removing the AuNP solution from the fridge, the AuNPs were centrifuged (8000 rpm, 15min), the solvent removed without losing AuNPs and sonicated with fresh ethanol to wash them. This was repeated three times, while replacing ethanol with 3.2ml dimethyl sulfoxide (DMSO) on the last step for each prepared MIP QCM. The falcon was sonicated until all AuNPs were dissolved into the solution.

The functionalized QCMs were removed from the fridge sonicated in distilled water and ethanol each two times. For the actual polymerization on each QCM, a UV permeable vial containing 3.5 ml DMSO, 86.6µl methacrylic acid (MAA), 338.8 µl trimethylolpropane trimethacrylate (TRIM) and 5 mg 4-cyano-4-(phenylcarbonothioylthio)pentanoic acid (CPA) was prepared. For the MIP QCMs, another 3.5ml of the prepared AuNP solution was added, while for the NIP QCMs another 3.5ml of DMSO were added. In this setup, MAA functions as the monomer, TRIM as the crosslinker and CPA as the RAFT agent. The prepared solutions were sonicated, the QCMs inserted and each vial flushed with argon for 5 minutes. Afterwards the vials were sonicated shortly and placed under a UV lamp of 365 nm for 3½ hours to polymerize. Following this, the nanoparticles were removed by sonicating the QCMs in DMSO for one hour and in distilled water for 15 minutes. The QCMs were ultimately left to dry in an oven at 80°C for 24 hours. [38 – 40]

3.2.2. QCM measurements

The different QCMs were measured in different ways to extract data. Firstly, with priorly produced AuNP solutions of different concentrations, it was determined whether there is an effect of the QCM designs on the measurement depending on the AuNP concentration. To do so, the 4 different concentrations were added in 200µl increments, waiting for the signal to stabilize before another injection. Between two injections the cell was flushed with 1ml PBS to wash AuNPs.

Similarly, to test for the influence of the background, the different QCMs were measured with AuNP solutions at the same concentration but varying PBS concentration. Again, each AuNP solution of different background concentration was measured 3 times with washing steps in between. The concentration of PBS of the washing solution changed with the change of injection type. The only variation is that an extra washing step was added when the background concentration was altered.

To measure the QCMs, gold nanoparticle solutions with known concentrations had to be prepared. For that purpose, 600µl from the 75nm gold nanosphere with PVP shell solution (Econix) were mixed with 15mg 16-MHDA in 10ml ethanol and sonicated for 3-5 hours until a

deep purple color emerged, to ensure the shell changed to 16-MHDA. Following this the solution was centrifuged (8000 rpm, 15 minutes), the solvent removed and washed by sonication with ethanol. This was repeated 3 times. Afterwards the solution was centrifuged again, all solvent removed and then 3 ml PBS were added. This led to a 1 mg/ml stock solution, which was diluted with PBS to 100µg/ml stock solution. From this solution, four stock solutions with the concentrations of 10 µg/ml, 5 µg/ml, 3 µg/ml, 1 µg/ml of nanospheres were created by dilution with PBS. The 100 mg/ml stock solution was also used to create three other stock solutions to measure the impact of the electrolyte concentration. For that the 100µg/ml stock solution was diluted to with PBS and MilliQ water in different ratios to produce three 10µg/ml gold nanosphere solutions with a PBS percentage of 100%, 50% and 10%. For washing purposes PBS alone was also diluted to these concentrations.

The QCM measurement cells were already made before by other group members. Figure 29 showcases a measuring cell. The measuring cells consisted of a solid cell with two spring contacts for the gas side, a PDMS lid with a sample chamber of 200µl and a backside to hold the parts together.

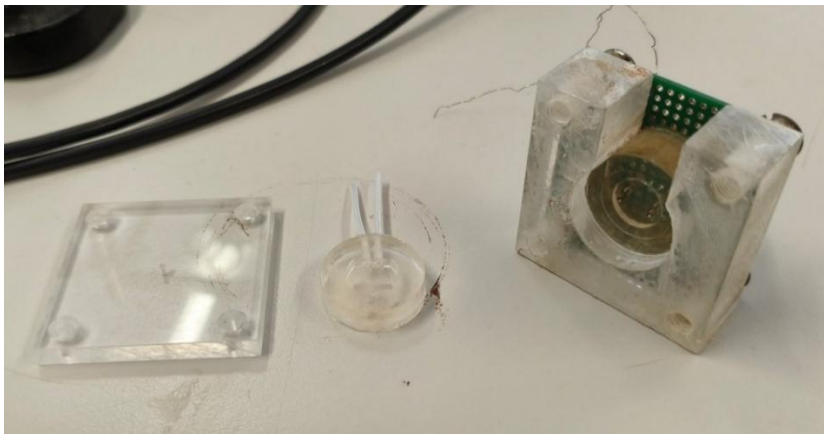

Figure 29: Picture of the QCM cell

Figure 30 shows the QCM measuring setup. To measure the QCMs they were first fixed in the measurement cells, which were filled with PBS as the background solution. The dampening and the resonance frequency of both electrodes was recorded with a network analyzer. After this, the QCM cell was connected to the measuring electronics consisting of an oscillator circuit, a power supply (Elektro Automatik EA-PS 2032-025) and a frequency counter (Agilent Universal frequency counter Keysight 53220A). The power supply was consistently set between 15.2 V – 15.5 V and 0.06 A – 0.08 A. The resonance oscillator was adjusted until the measured resonance frequence displayed the same as what was recorded on the network analyzer. Since in-situ polymerization was used, the electrodes were often very similar and a cross-talk of the resonance frequencies occurred commonly and was tried to be remedied.

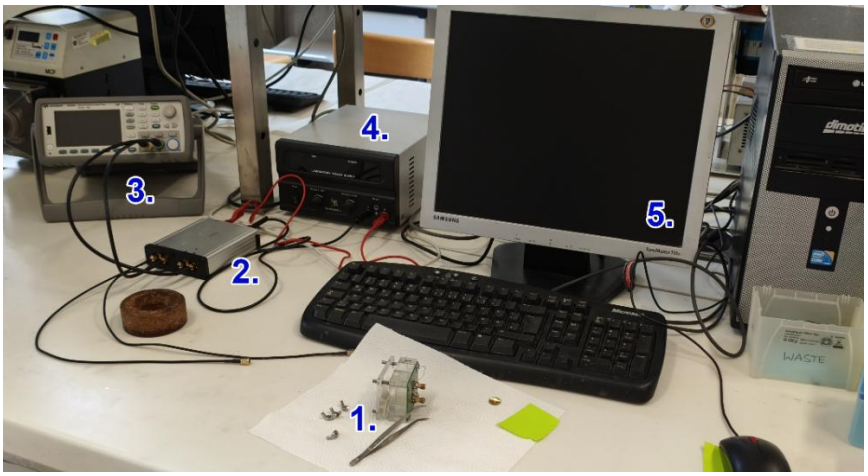

Figure 30: QCM measurement setup (1) QCM measurement cell (2) oscillation circuit (3) frequency counter (4) power supply (5) computer

3.2.3. QCM surface characterization

To characterize the QCMs after measurement, SEM and AFM were utilized to detect AuNPs and cavities on the surface. To better see cavities instead of only nanoparticles and salt crystals, was the QCM sonicated in DMSO for five minutes after the QCM measurement. Typically, the QCMs were analyzed with SEM first.

All SEM images were taken with a Zeiss Supra 55 VP was utilized (see Figure 31).

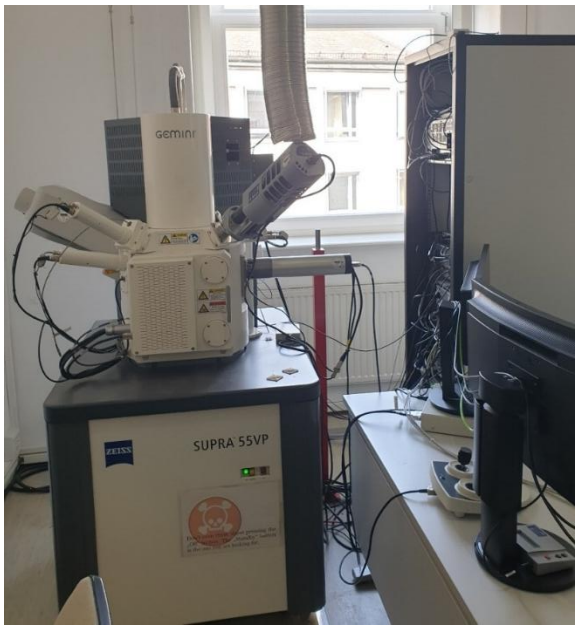

Figure 31: Supra Zeiss 55 VP scanning electron microscope

A Bruker AFM (Multimode 9 Atomic Force Microscope digital instruments with a picoforce spectroscopy control module) was used (see Figure 32) to characterize the surface.

Figure 32: AFM setup

4. Results and Discussion

4.1. Motivation for the different employed electrode manufacturing methods

To ultimately compare the different designs, first it is necessary to find the optimal way to deposit the electrode patterns. According to literature [6] [7], uniformity and surface roughness impact the QCM measurement, which leads to the need to produce very smooth surfaces.

Screen printing leads to a reproducible, but uneven surface. Producing the electrodes on the gas side of the QCMs was always performed with screen printing, because the surface irregularities do not matter there as much as on the liquid side. Since nanoparticles were used to synthesize MIP, the surface irregularities resulting from screen printing can influence measurement results.

When preparing the masks from parasol foil, only the electrode structures were deposited, followed by screen printing the connecting bridge. The reason is that when the whole masks were prepared by hand, they turned out very irregular, which can lead to deviations.

Finally, 3D-printed masks were employed, because they turned out very reproducible, much more so than any manually produced ones. At the same time the 3D-printed masks allow depositing the electrodes with PVD and therefore lead to a more even surface than screen printing.

4.2. Optimization of electrode manufacturing

All methods of electrode manufacturing tested indeed yielded usable QCMs, though with varying results.

4.2.1. Optimizing 3D printed PVD masks

A multitude of 3D-printed masks were designed for PVD electrode deposition. The following sections describe each iteration and their respective advantages and drawbacks and thus the rationale leading to the next iteration step.

3D printed masks: Batch 1

Figures 33 to 38 show the first batch of QCM mask designs. All these designs were developed before any PVD deposition with PLA were attempted.

Figure 33:(Design 1.1) QCM mask design first batch. A fully flat mask with slits

Figure 34: (Design 1.2) QCM mask design first batch. A mask with an elevated patch for easier grip

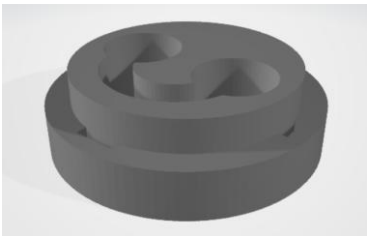

Figure 35: (Design 1.3) QCM mask design first batch. A thicker QCM mask

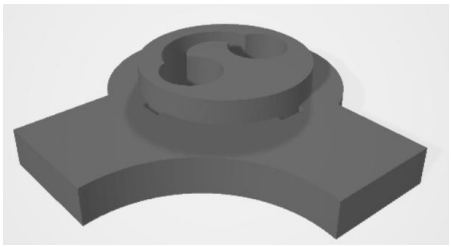

Figure 36: (Design 1.4) QCM mask design first batch. A thicker QCM mask with extrusions for better adhesion

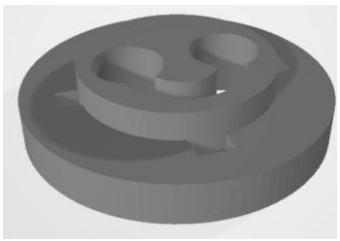

Figure 37: (Design 1.5) QCM mask design first batch. A larger outer border for better adhesion

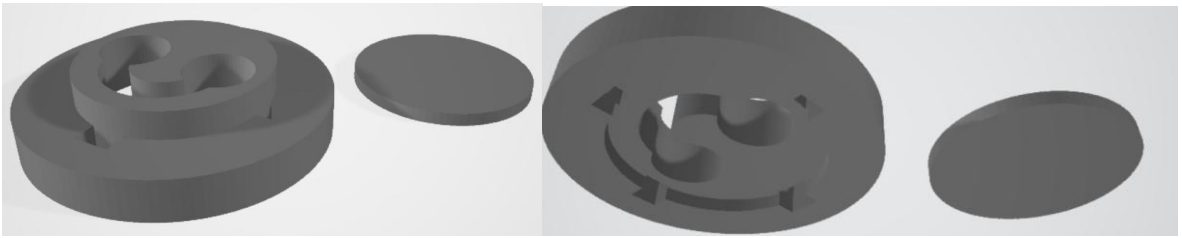

Figure 38: (Design 1.6) QCM mask design first batch. A larger border for better adhesion with an inlet for the QCM backside part to keep QCM in place.

It was possible to 3D-print all these designs. They all contain slits on the sides so that the mask can be placed on the QCM in such a way that it allows for centering it. Furthermore, they were meant to be placed on top of the QCM mounted in the PVD apparatus to be held in place by gravity.

The first design (Figure 33), is a simple round and flat thin mask to be placed on top of the QCM. The second design (Figure 34) slightly altered this by adjusting the sides, resulting in

better grip to remove and place it more easily. The third design (Figure 35) was made thicker to be heavier and, thus, to stay on the QCM. The fourth and fifth designs (Figure 36 and Figure 37) comprised an enlarged border to make sure the mask could be fixed with tape. Finally, the sixth design (Figure 38) of the first batch was designed with a backside press to ensure that the mask sits more tightly on the QCM. The thicker masks were all designed to be 5mm thick, while the thin ones were manufactured 1mm thick.

The 3D-printed masks comprise one very even side at the bottom, whereas all other surfaces are rougher, because the printer adds the filament line by line. In Figure 39 this surface roughness disparity is shown. Since a more even surface allows for better adhesion between the QCM and mask, future designs aimed at placing the base of the mask directly on the QCM.

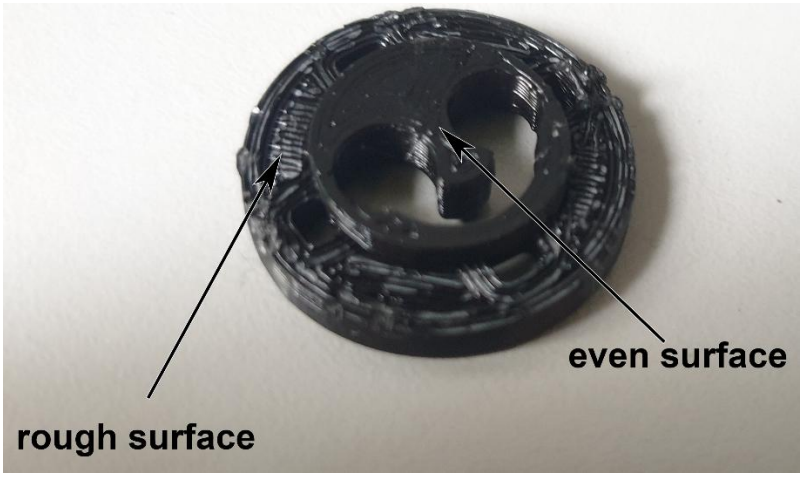

Figure 39: Comparison of how evenly the mask surface is being printed on the base plate of the 3D printer compared to how rough the surface becomes when printed on air/ on the top

During PVD deposition all designs turned out inadequate. One of their common drawbacks is that they have been designed to be placed on top of the QCMs and kept there through gravity. The problem hereby is that the PVD sample plate rests in the PVD machine upside down, meaning all masks just fell off. This was remedied by fixing them in place with tape (see Figure 40), but this did not help in all cases. Two designs are not usable for PVD at all. These are the thicker version of the QCM mask (Design 1.4) and the larger QCM mask with a backplate (Design 1.6). The thicker design can not simply be fixed onto the plate with tape. The problem with the design with a backplate is that the designed backplate is too big and so the mask could not be fixed on top of the sample plate without breaking the QCM inside.

Figure 40:QCM masks fixed with tape on PVD plate.

Figure 41: QCM that resulted from one of the thicker masks from the first batch.

After deposition another issue became apparent. Figure 41 shows a QCM deposited with a thicker mask. The QCMs electrodes resulting from thicker masks were transparent, which means the thicker masks lead to insufficient amounts of Cr and Au being deposited on the QCMs. The thin masks meanwhile all fell off during PVD. Meanwhile, the parasol foil masks lead to appreciably shaped gold electrodes. Figure 42 shows why thicker masks lead to badly deposited electrodes: during deposition the sample plate is spinning and there is Cr/Au in gas phase. The Cr/Au in gas phase is very delicately deposited. Since the sample plate is spinning there is a very limited time window for the metal to diffuse through the mask holes and deposit before the spinning plate moved the mask so much that the metal atoms are hitting the inner sides of the mask instead. This means that very thin masks lead to better/more even deposition on the QCM.

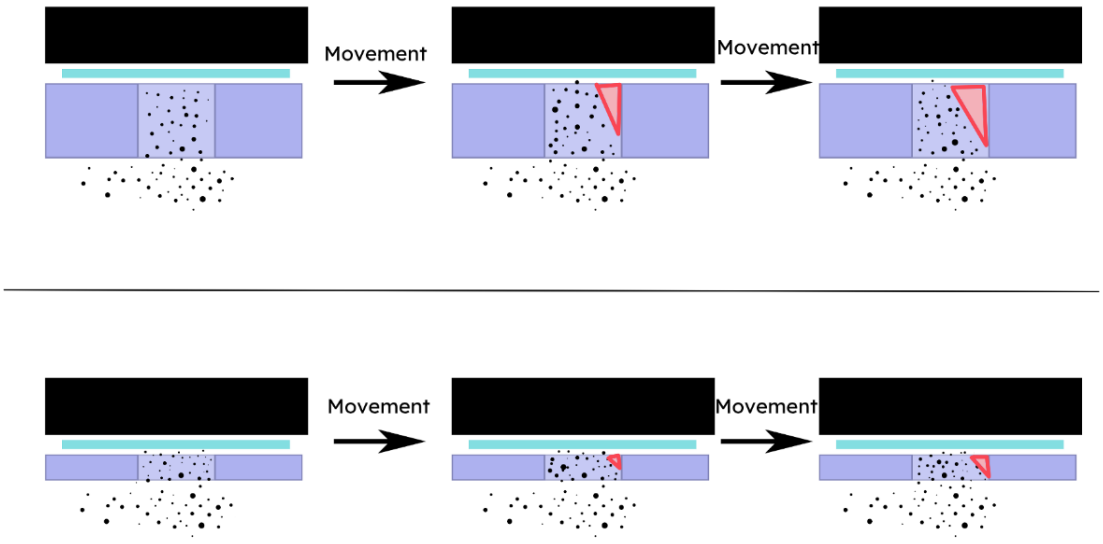

Figure 42: Schematic representation of moving QCMs with masks during PVD deposition and the gas metallic particles within the masks. The way the diffusion in gas phase is influenced by moving the QCMs (cyan) and masks (purple) is influencing the way the vaporized metallic particles are distributed in the QCM mask and it is visible why for deposition it is better to have thinner masks (bottom), because more of the particles reach the QCM, rather than thicker masks (top). The area no particles diffuse (red area) grows depending on the movement speed, which is influenced where on the deposition plate the QCM and mask is placed.

Another point of concern was the possibility of the QCM masks melting at PVD conditions. However, the experiments revealed that this does not happen.

To summarize, a mask needs to be thin, smooth on the QCMs side, capable of staying on the sample plate, not crushing the QCMs, designed to center the QCM in the right position easily.

3D printed masks: Batch 2

These requirements led to the next design (see Figure 43), which fulfils all conditions but one, namely that the mask's smooth side does not face the QCM.

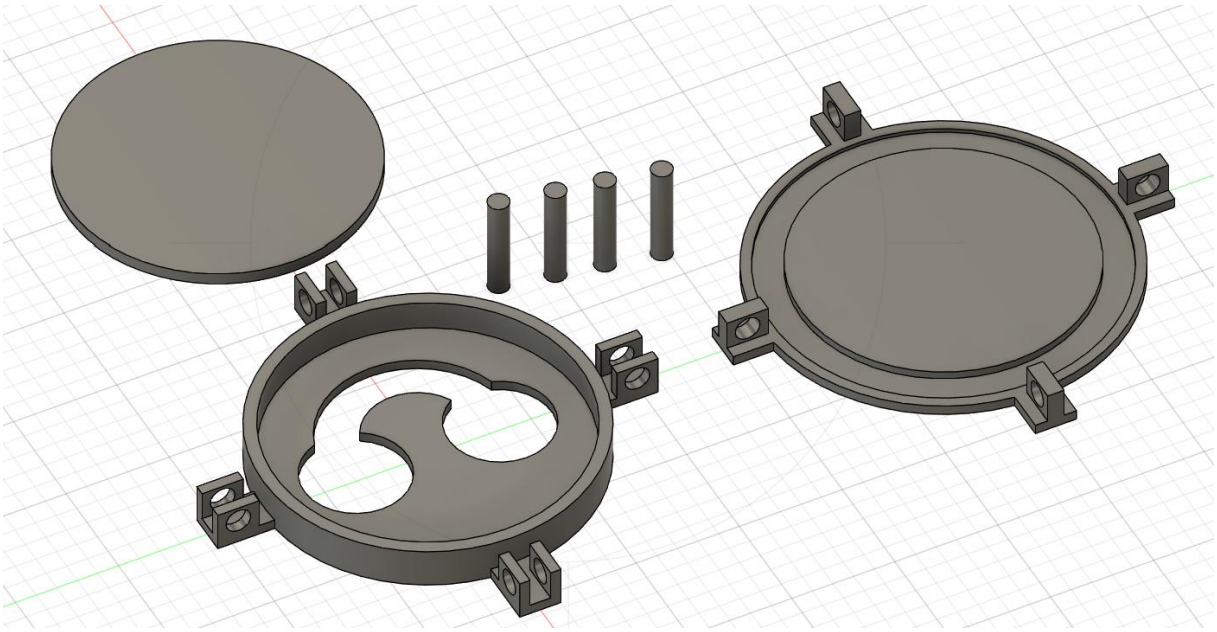

Figure 43: (Design 2.1) QCM mask design batch 2.

The idea is putting the QCM inside an entire framework during deposition instead of sticking it onto tape and then the mask on top, to ensure stable contact between QCM and mask. The backplate presses the QCM even more onto the mask. It also functions as a protection from any metallic vapors that enter the mask. The mask and all walls itself were made 0.5mm thin.

The problem with the design is that all of the locks and walls of the design are too thin and small to be printable. At 0.5mm thickness of filament, the mask would basically consist of only one 3D printed filament layer, which would lead to inconsistencies in the final QCM result. Also, when the mask is only 0.5mm thin, any form of pressure from the QCM would be enough to bend it and, in turn, reduce contact between the QCM and the mask. The general idea is very promising, so for further development the design was only adjusted.

Hence, the PVD mask walls need to be thick enough to be mechanically sturdy and printable, but thin enough to allow for good quality PVD.

3D printed masks: Batch 3

The third iteration relies on the same design principle, but adapts it to ensure that the quartz plates adhere to the surface of the PVD sample plate, the way the pattern was inserted and how thick the PVD mask should be. It consists of a top part that acted as the mask for the PVD deposition, a central part placed inside the QCM mask to improve contact between the mask and QCM, a bottom part that would stick the entire mask to the surface of the sample plate and finally locks to keep all parts together.

Bottom parts:

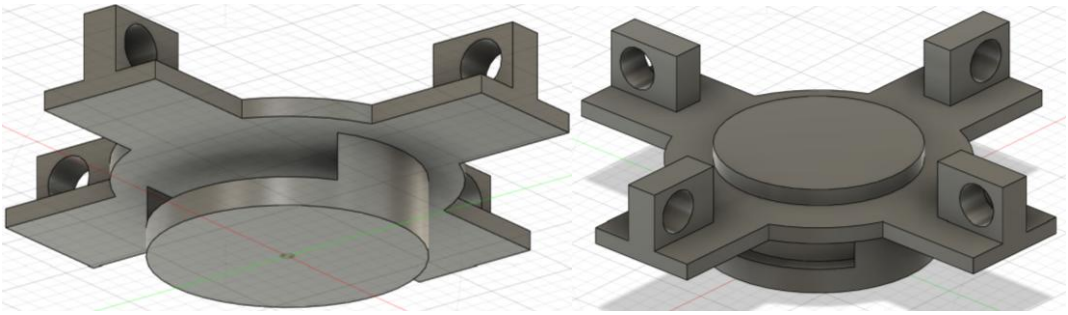

Figure 44: PVD QCM 3D-printed mask bottom part with a magnet inlet. (left) Bottom perspective (right) top perspective (hole radius 1.3mm, wall thickness 2mm, ground thickness 1mm)

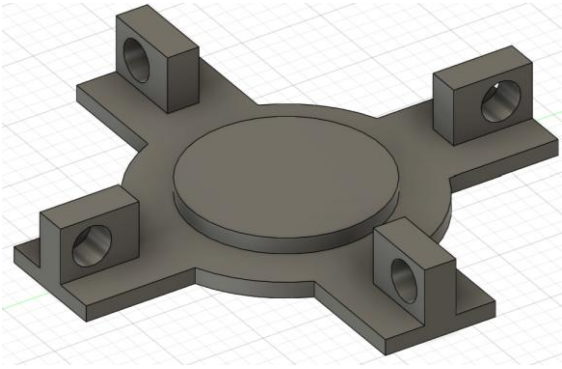

Figure 45: PVD QCM 3D-printed mask bottom part with a flat bottom area for gluing it to the PVD sample plate (hole radius 1.3mm, wall thickness 2mm, ground thickness 1mm)

Figure 44 and Figure 45 show the two designs resulting from the next iteration step. The setup in Figure 44 is meant for using a magnetic sample plate, while the design in Figure 45 is meant to adhere with glue or tape to the sample plate.

Even before PVD deposition it became clear that using double-sided adhesive foil is superior, because the sample plate is not magnetic. However, when using adhesive tape, this design turned out suitable for the purpose and served during all further deposition experiments.

Locks:

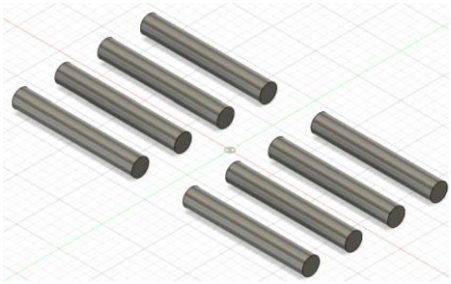

Figure 46: The locks to seal the QCM mask (length 14mm, radius 1mm)

The locks (radius 1mm, length 14mm) (see Figure 46) were simply scaled up to fit the larger holes in the newer designs. The only slight changes are laying them sideways, because it is easier for the 3D-printer to print them that way, as well as making them longer, because then they are easier to insert and remove.

Central parts:

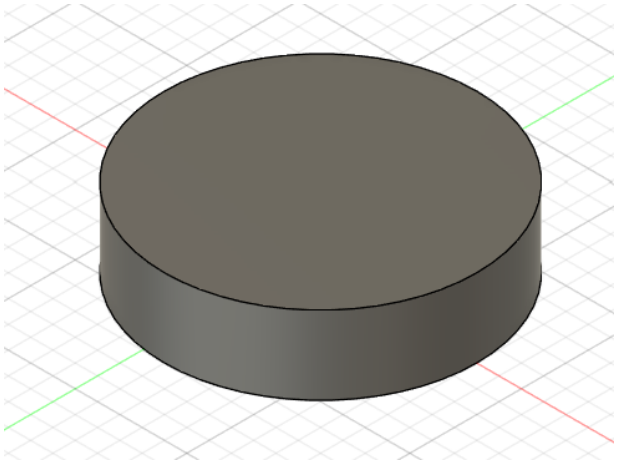

Figure 47: PVD QCM mask single part inner press. A thicker 3D printed part that fills the whole space of the mask. (thickness 3.5mm, radius 7mm)

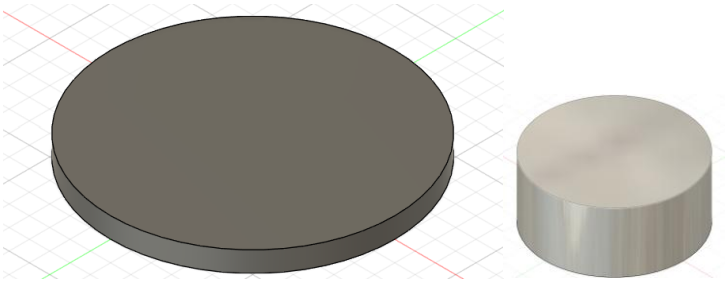

Figure 48: PVD QCM mask inner press. Consisting of (left) a protection plate of the same diameter as the QCM and lies on top of it and (right) a smaller, but thicker PDMS piece that bridges the gap to the back part of the mask. (1mm thick, 7mm radius, PDMS press thickness ~2.7mm)

Two possible designs of the middle plate were assessed: (see Figure 47) one comprising a 3D printed plate 3.5mm thick and the other one (see Figure 48) consisting of a 3D printed plate 1mm high and a PDMS cylinder (~2.7 mm high) as an elastic part to press the plate to the QCM. Both designs worked, but the second turned out more convenient to handle.

Top parts:

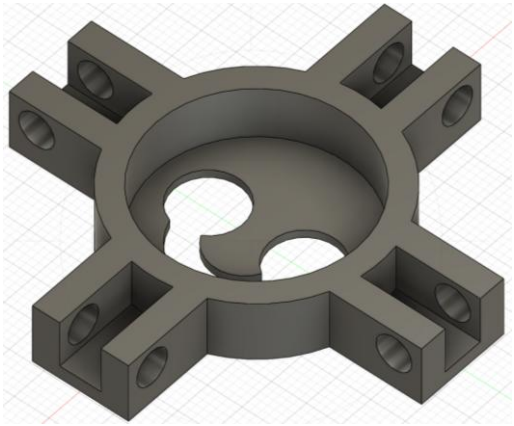

Figure 49: PVD QCM mask single part top part design. (hole radius 1.3mm, wall thickness 2mm)

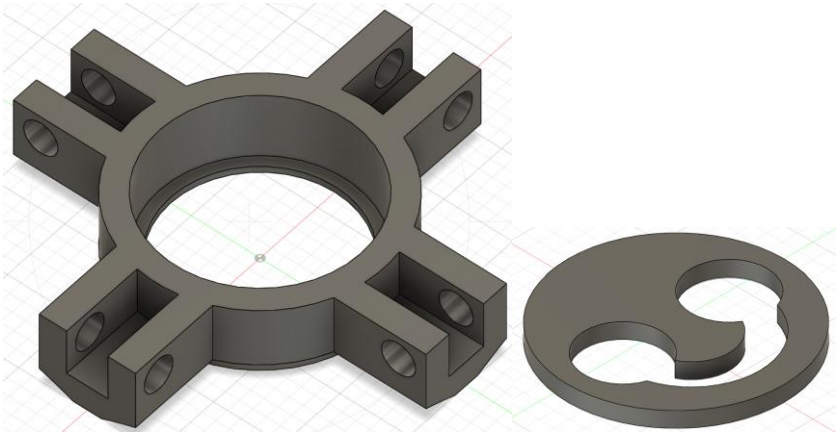

Figure 50: PVD QCM mask clippable mask top part design. (hole radius 1.3mm, wall thickness 2mm, pattern plate thickness 1mm)

Two designs of the top part were considered. One (see Figure 49) comprising of a fully 3D-printed mask with the pattern and the other one (see Figure 50) consisting of a 3D-printed framework and a 3D-printed plate with the pattern to be clipped into the framework. Both designs were successful, but the second design allows for a better contact between QCM and mask. In Figure 51 and Figure 52 the designs contact to the mask is compared and it is visible how in the clippable mask design in Figure 52 the QCM mask lies really well on the QCM, compared to the other.

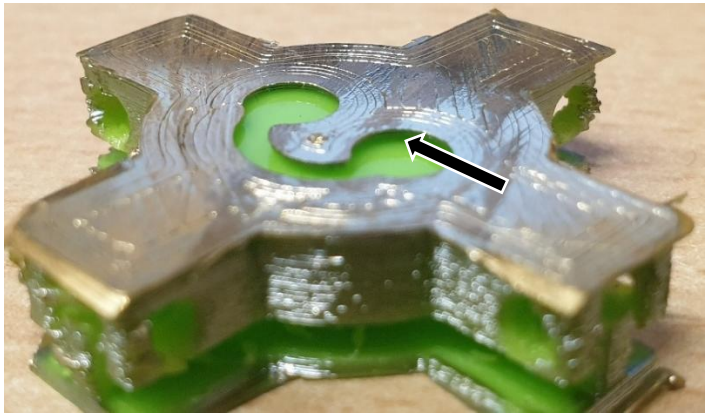

Figure 51: Photo of a QCM in a single part top piece 3D printed mask design.

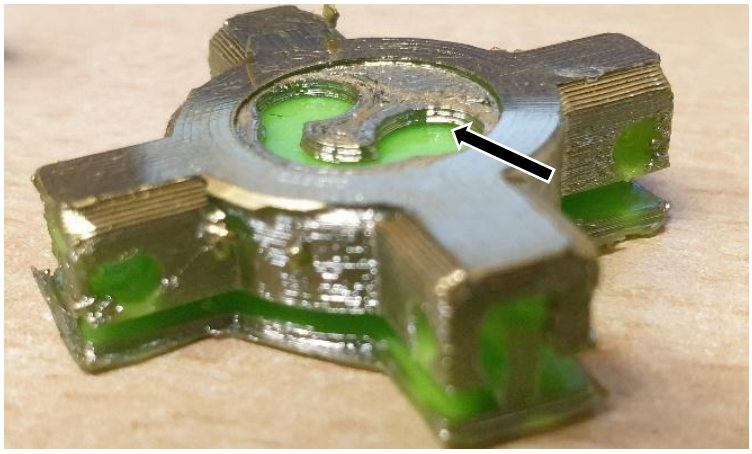

Figure 52: Photo of a QCM in a clippable 3D printed mask design. The mask surfaces show the different contact between mask and QCM depending whether the rougher or more even surface is in contact with the QCM.

Figure 53 shows QCMs resulting from these two top part designs. A slight chromium border is visible on the QCMs resulting from the single part 3D-printed mask designs. This is because of the lower adherence between the mask and the QCM allowing for Cr to deposit to an extent in the area between the mask and the QCM. At the same time, no gold has been deposited in those areas, which is indicated by Cr filling the gap.

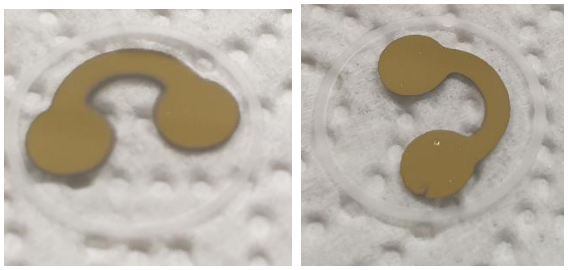

Figure 53: QCMs manufactured using the different 3D-printed mask designs. (left) single part design. A slight grey chromium border is visible (right) clippable mask design.

Figures 54 to Figure 61 show light microscopy images of the analyzed Cr border of two QCMs that were made and compared with each mask type.

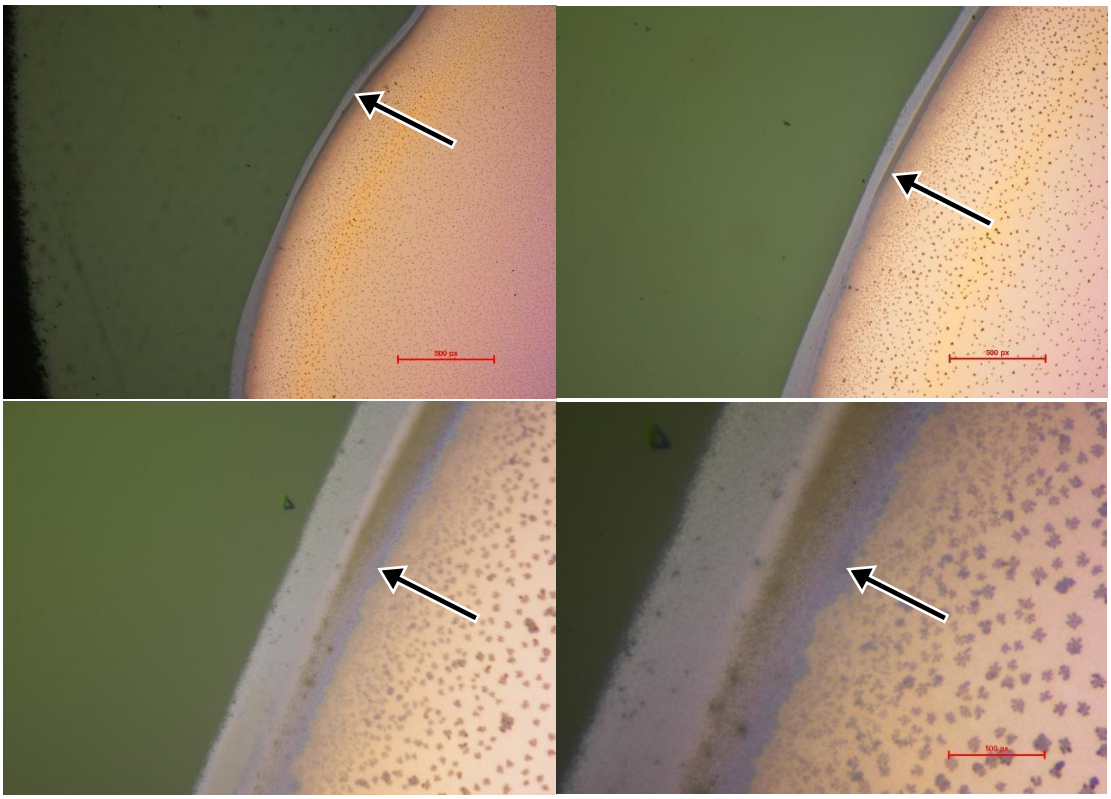

Figure 54: QCM Nr.1. visible Cr on the electrode edge when using single part 3D-printed Mask. These images all look at the outer rim of an electrode (top left) 5x magnification, ruler = 1000µm, (top right) 10x magnification, ruler = 500µm, (bottom left) 50x magnification {ruler forgotten}, (bottom right) 100x magnification, ruler = 50µm. The arrow is to show the chromium border.

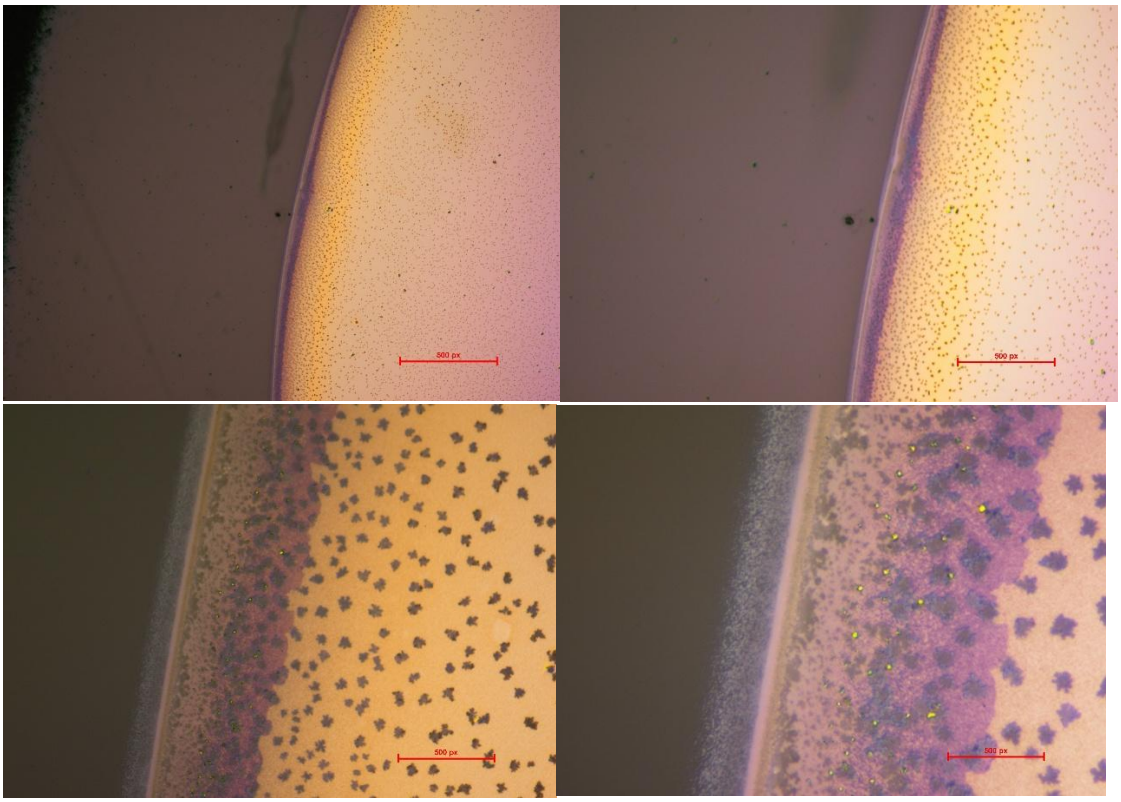

Figure 55: QCM Nr. 2. visible Cr on the electrode edge when using single part 3D-printed Mask. These images all look at the outer rim of an electrode (top left) 5x magnification, ruler = 1000µm, (top right) 10x magnification, ruler = 500µm, (bottom left) 50x magnification, ruler = 100µm, (bottom right) 100x magnification, ruler = 50µm

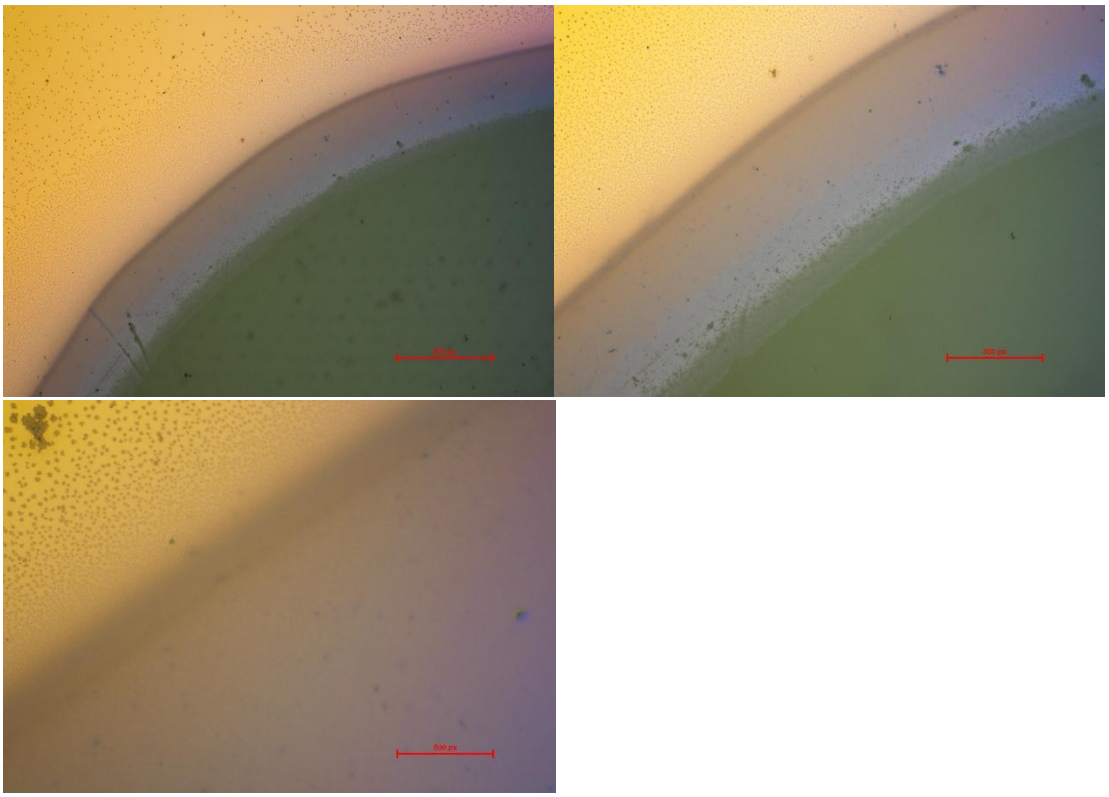

Figure 56: QCM Nr. 1. visible Cr on the electrode edge when using single part 3D-printed Mask. These images all look at the inner rim of the bridge that connects the electrodes (top left) 5x magnification, ruler = 1000µm, (top right) 10x magnification, ruler = 500µm, (bottom left) 50x magnification, ruler = 100µm, {no 100x magnification, because the border was too big}

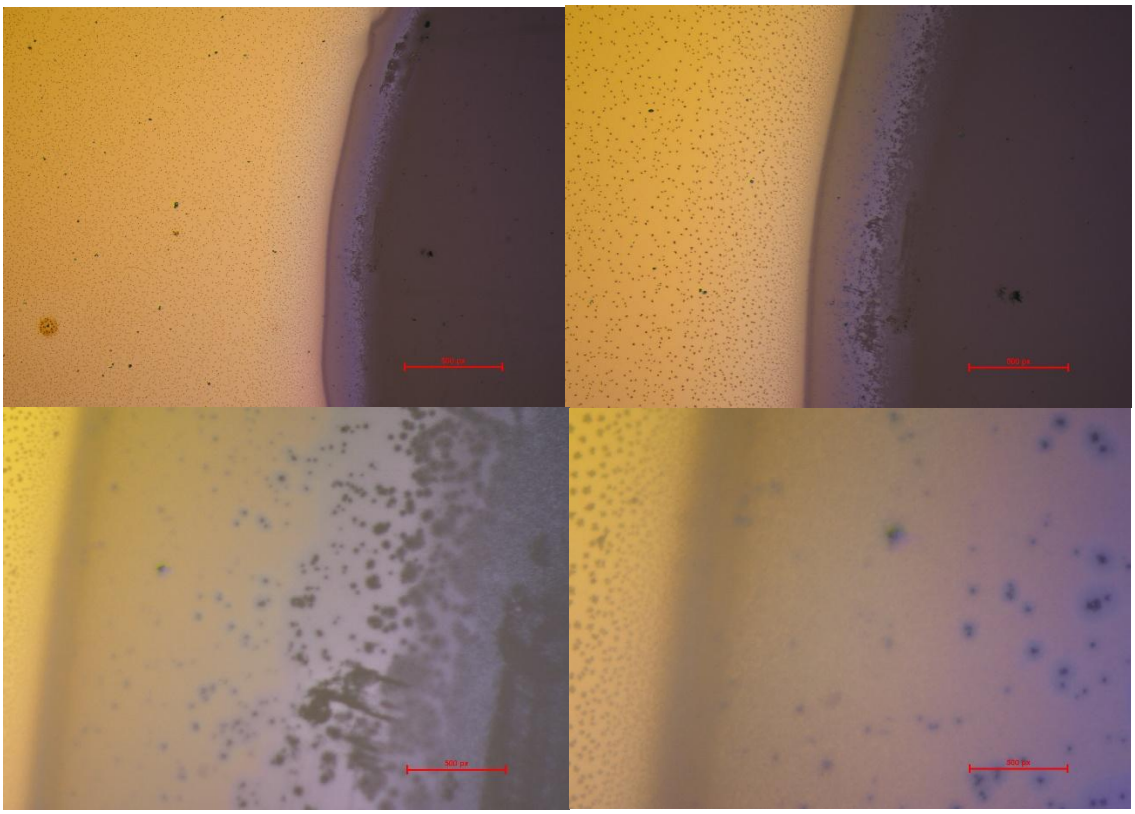

Figure 57: QCM Nr. 2. visible Cr on the electrode edge when using single part 3D-printed Mask. These images all look at the inner rim of the bridge that connects the electrodes (top left) 5x magnification, ruler = 1000µm, (top right) 10x magnification, ruler = 500µm, (bottom left) 50x magnification, ruler = 100µm, (bottom right) 100x magnification, ruler = 50µm

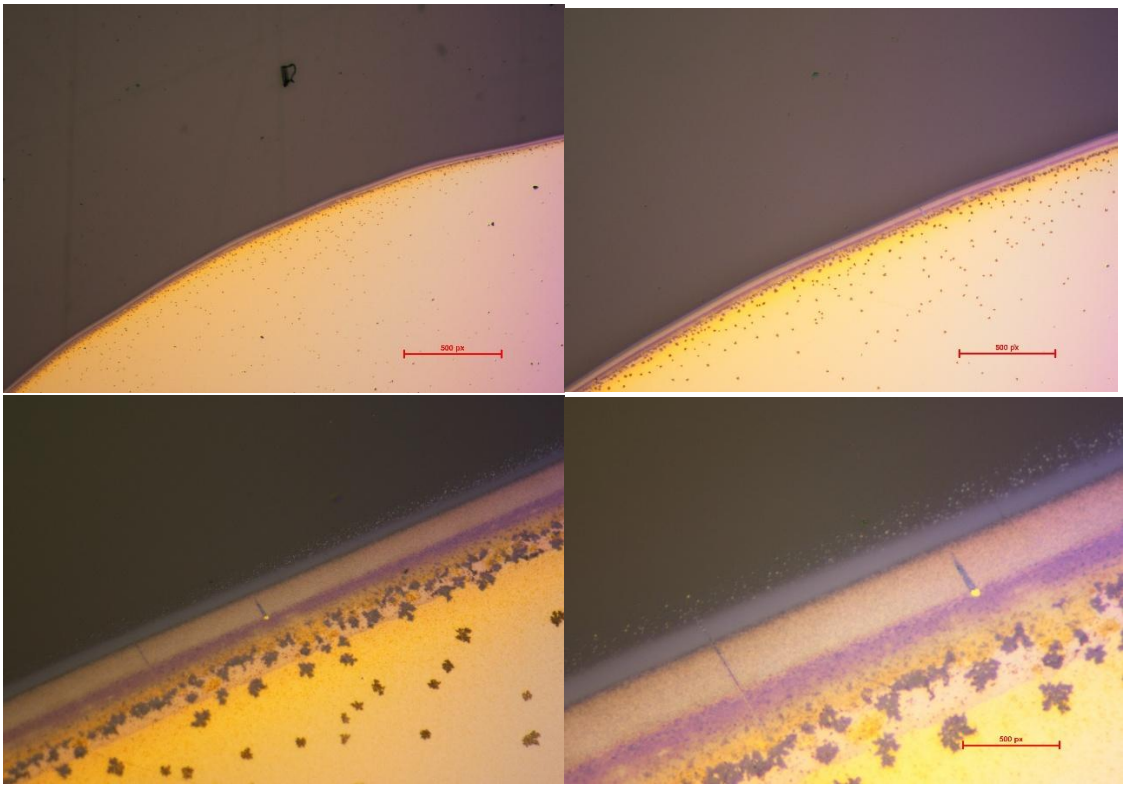

Figure 58: QCM Nr. 3. visible Cr on the electrode edge when using clip design 3D-printed Mask. These images all look at the outer rim of an electrode (top left) 5x magnification, ruler = 1000µm, (top right) 10x magnification, ruler = 500µm, (bottom left) 50x magnification, ruler = 100µm, (bottom right) 100x magnification, ruler = 50µm

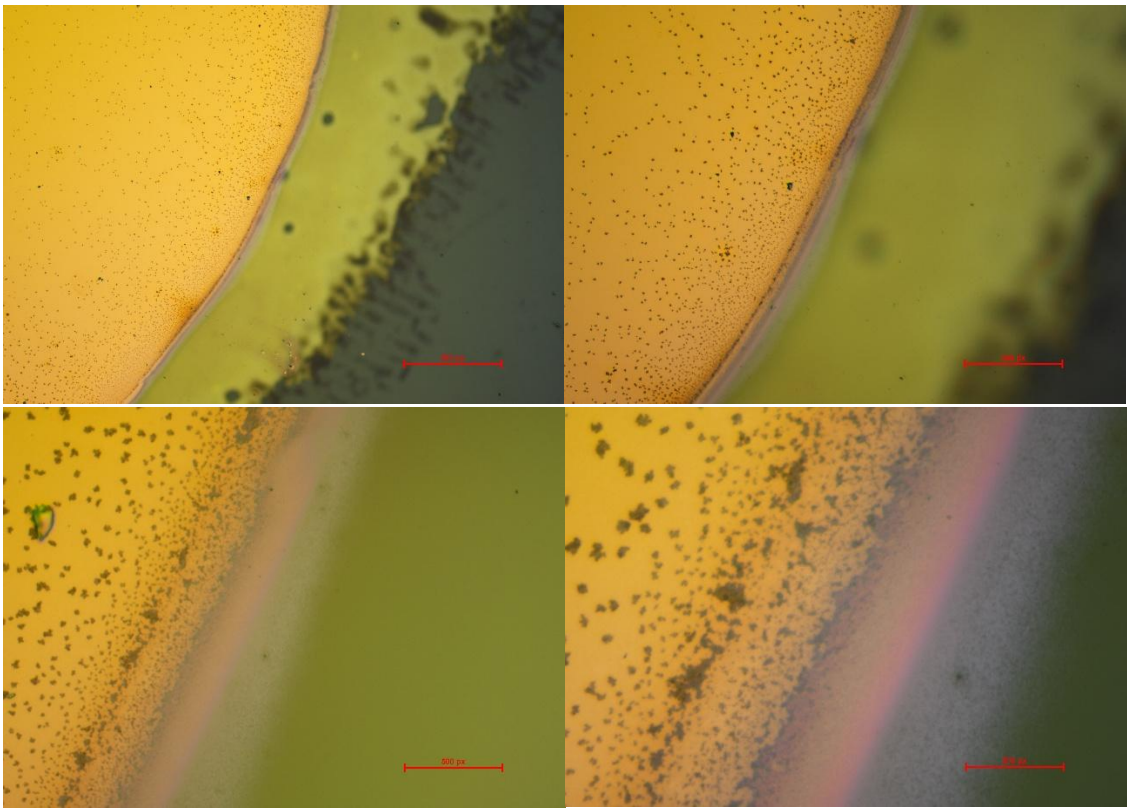

Figure 59: QCM Nr. 4. visible Cr on the electrode edge when using clip design 3D-printed Mask. These images all look at the outer rim of an electrode. The green area is from a not aligned electrode from the other side of the QCM. (top left) 5x magnification, ruler = 1000µm, (top right) 10x magnification, ruler = 500µm, (bottom left) 50x magnification, ruler = 100µm, (bottom right) 100x magnification, ruler = 50µm

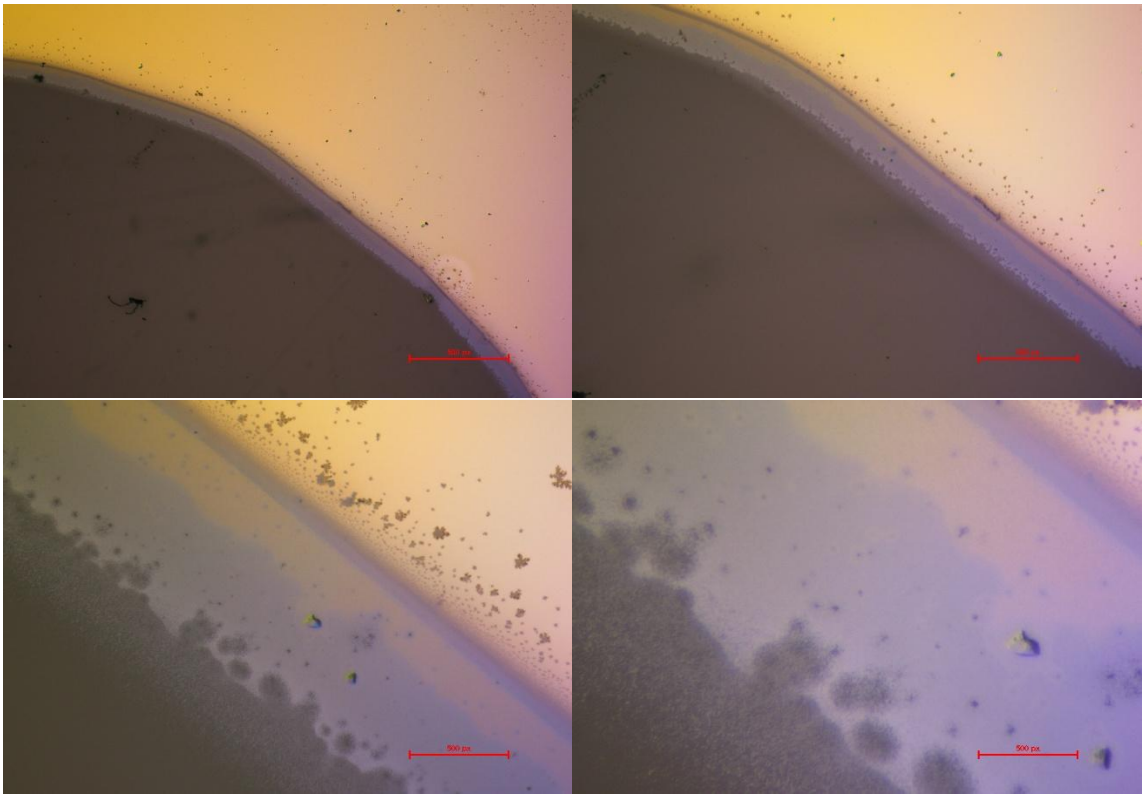

Figure 60: QCM Nr. 3. visible Cr on the electrode edge when using clip design 3D-printed Mask. These images all look at the inner rim of the bridge that connects the electrodes (top left) 5x magnification, ruler = 1000µm, (top right) 10x magnification, ruler = 500µm, (bottom left) 50x magnification, ruler = 100µm, (bottom right) 100x magnification, ruler = 50µm

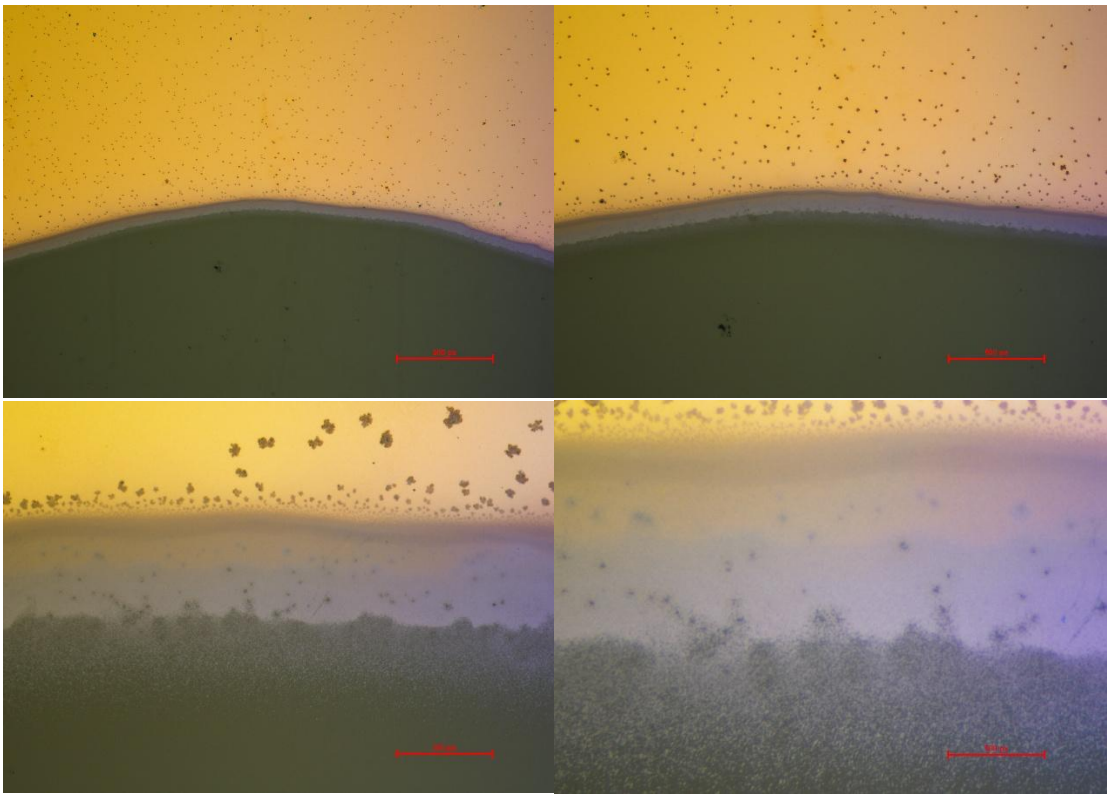

Figure 61: QCM Nr. 4. visible Cr on the electrode edge when using clip design 3D-printed Mask. These images all look at the inner rim of the bridge that connects the electrodes (top left) 5x magnification, ruler = 1000µm, (top right) 10x magnification, ruler = 500µm, (bottom left) 50x magnification, ruler = 100µm, (bottom right) 100x magnification, ruler = 50µm

These light microscope images captured the areas with the smallest and biggest borders on each QCM. The areas with the smallest border are those where the 3D printed top part and the pattern plate are closest to each other, while the area with the biggest border is the point farthest from the edges of the mask. In Figure 62 those areas are marked.

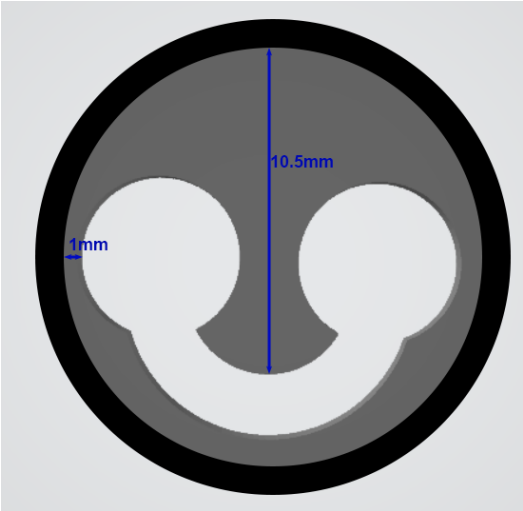

Figure 62: The difference in distance of the pattern to the more rigid parts of the mask (the sides) to visualize why the inner areas don't adhere as well to the QCM.

Table 1: Averaged and rounded biggest and smallest electrode chromium borders extracted from the light microscope photos resulting from the single part masks and the clippable masks.

	Single part design	Clippable mask design
Smallest Cr Border	95µm	50µm
Biggest Cr Border	820µm	200µm

Table 1 summarizes the extracted border sizes from the light microscope images. It shows that the clippable mask design indeed leads to better contact between the mask and QCMs leading to smaller areas containing only chromium. Removing the masks after deposition is also significantly easier with the clippable mask design, because the QCMs are less likely to get stuck. Because of these advantages, all further QCMs were deposited with the clippable 3D-printed mask designs.

Finally, as a last step the thickness of the pattern plate design was optimized as well. Figures 63-70 show light microscopy images of the Cr borders from QCMs produced with different mask thicknesses.

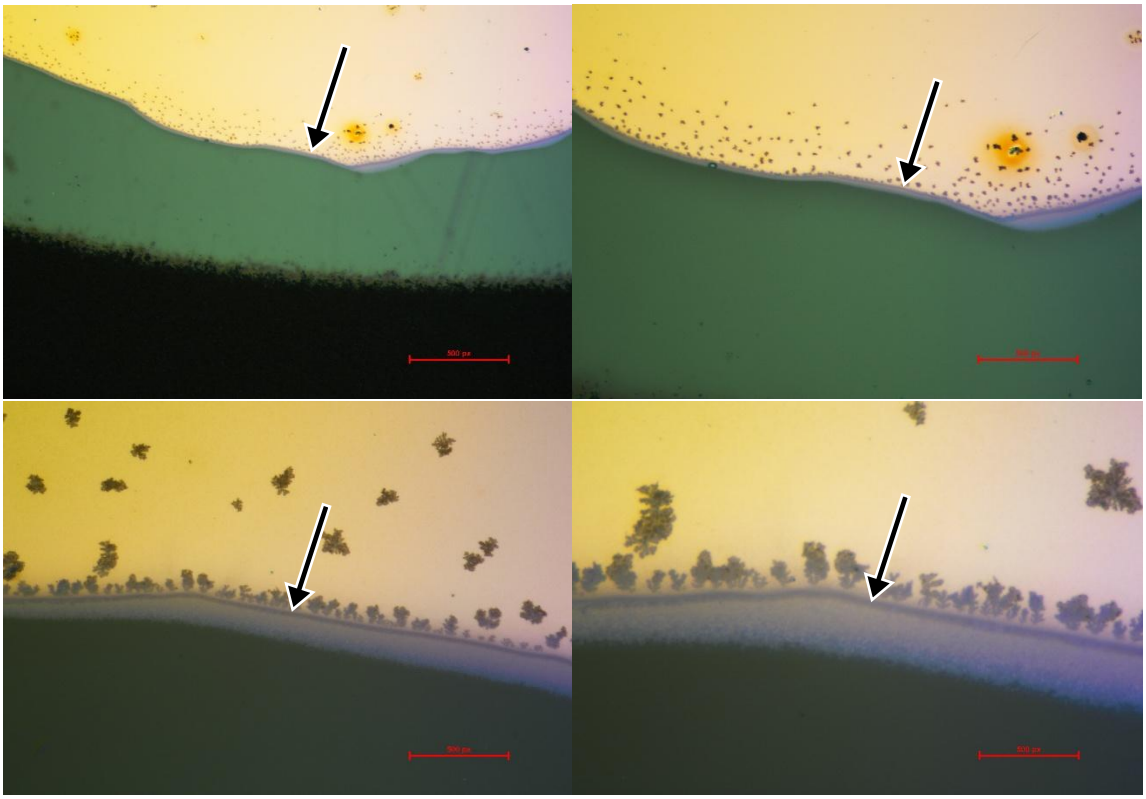

Figure 63: QCM Nr.1. visible Cr on the electrode edge when using a 0.5mm thick 3D-printed mask. These images all look at the outer rim of an electrode (top left) 5x magnification, ruler = 1000µm, (top right) 10x magnification, ruler = 500µm, (bottom left) 50x magnification, ruler = 100µm, (bottom right) 100x magnification, ruler = 50µm. The arrow is to show the chromium border.

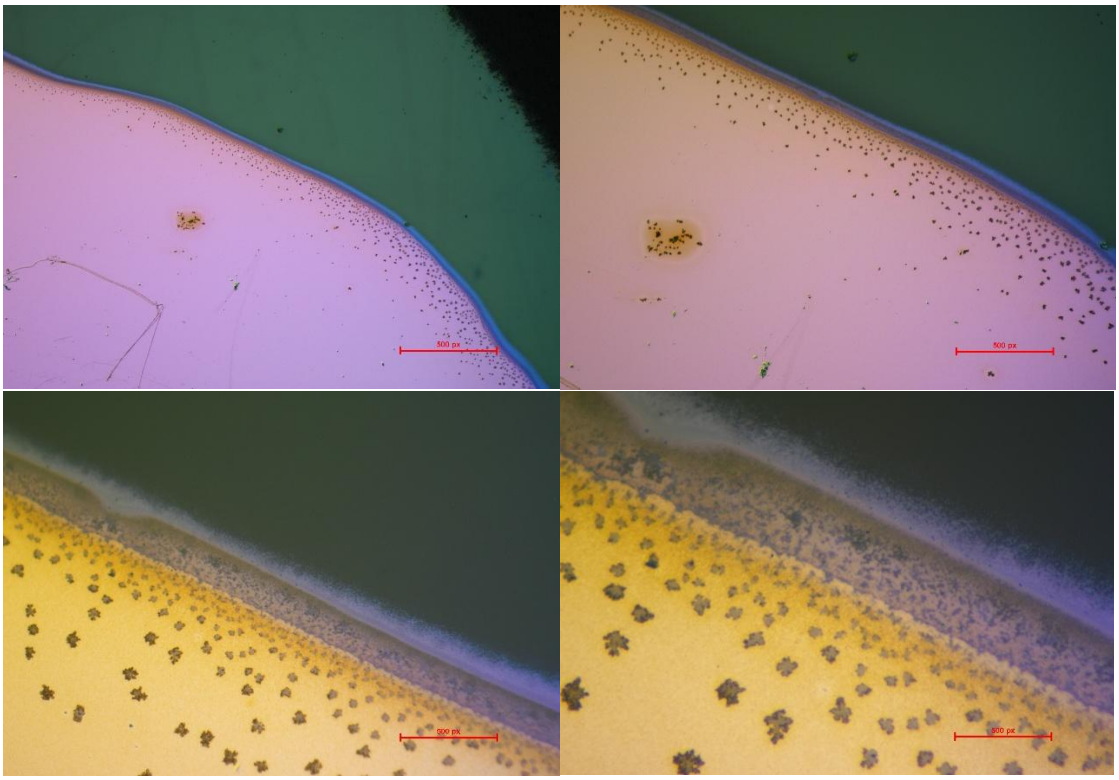

Figure 64: QCM Nr.2. visible Cr on the electrode edge when using a 0.5mm thick 3D-printed mask. These images all look at the outer rim of an electrode (top left) 5x magnification, ruler = 1000µm, (top right) 10x magnification, ruler = 500µm, (bottom left) 50x magnification, ruler = 100µm, (bottom right) 100x magnification, ruler = 50µm

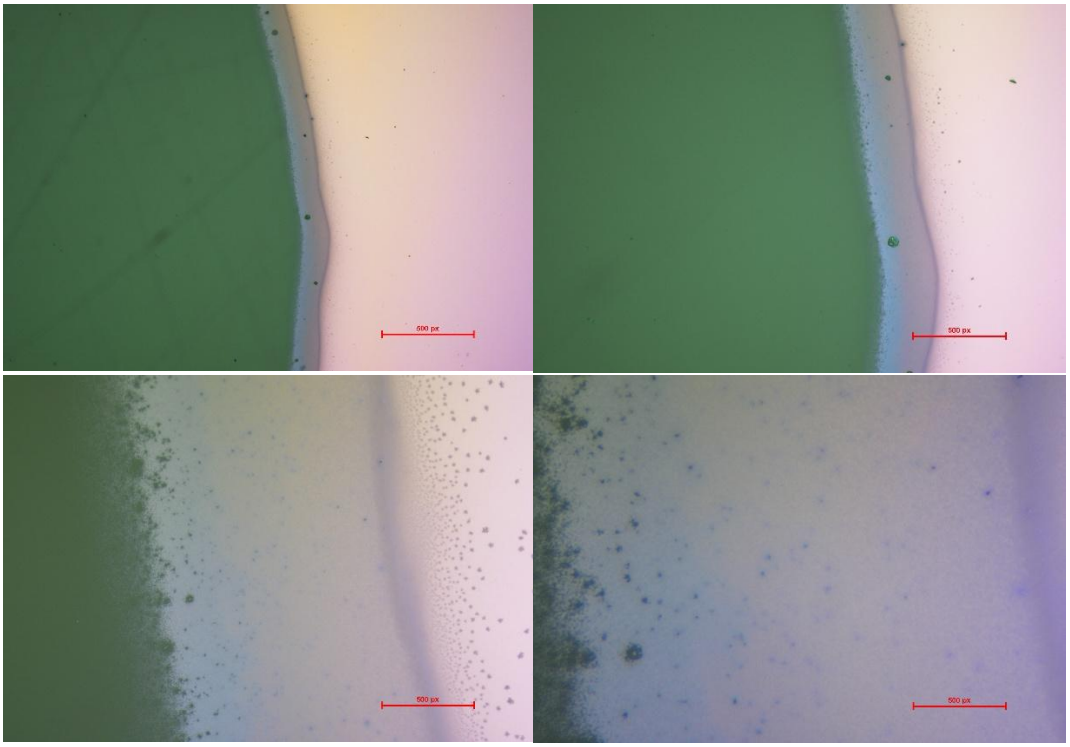

Figure 65: QCM Nr.1. visible Cr on the electrode edge when using a 0.5mm thick 3D-printed mask. These images all look at the inner rim of the bridge that connects the electrodes (top left) 5x magnification, ruler = 1000µm, (top right) 10x magnification, ruler = 500µm, (bottom left) 50x magnification, ruler = 100µm, (bottom right) 100x magnification, ruler = 50µm

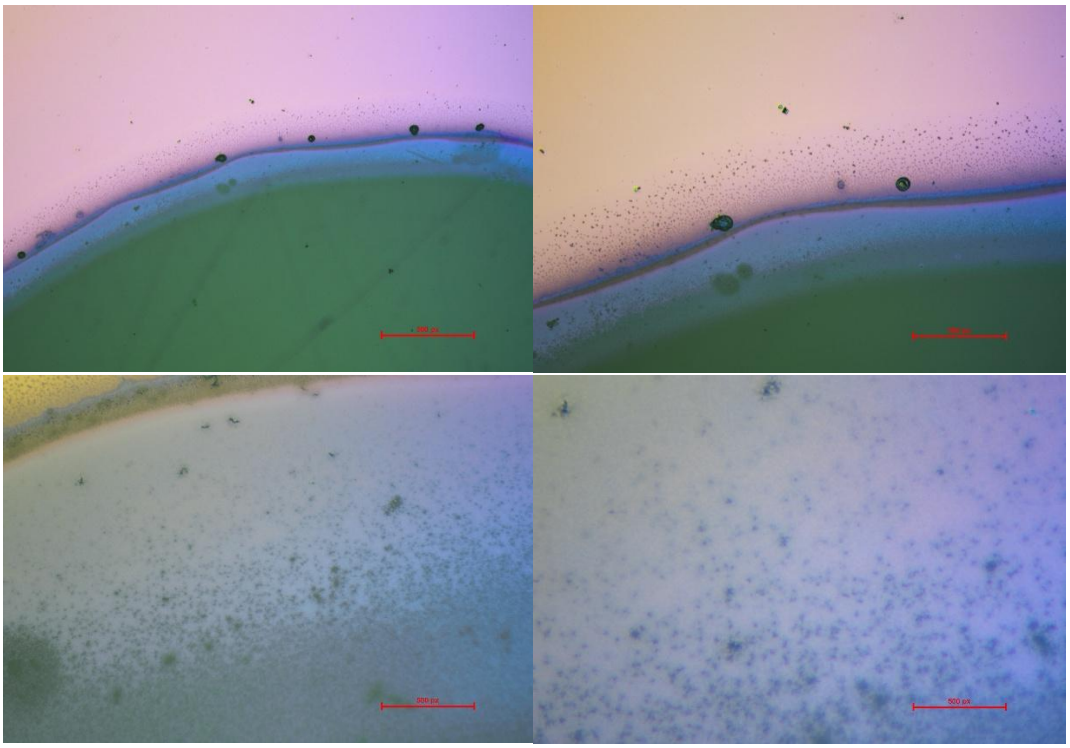

Figure 66: QCM Nr.2. visible Cr on the electrode edge when using a 0.5mm thick 3D-printed mask. These images all look at the inner rim of the bridge that connects the electrodes (top left) 5x magnification, ruler = 1000µm, (top right) 10x magnification, ruler = 500µm, (bottom left) 50x magnification, ruler = 100µm, (bottom right) 100x magnification, ruler = 50µm

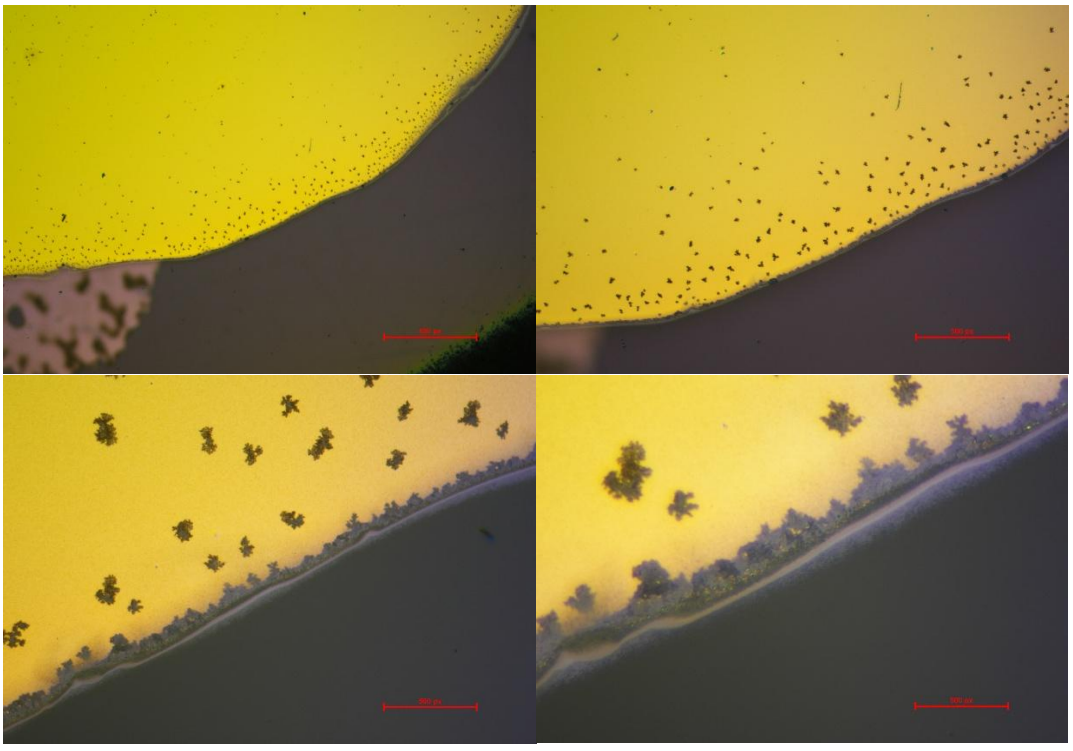

Figure 67: QCM Nr.3. visible Cr on the electrode edge when using a 1mm thick 3D-printed mask. These images all look at the outer rim of an electrode (top left) 5x magnification, ruler = 1000µm, (top right) 10x magnification, ruler = 500µm, (bottom left) 50x magnification, ruler = 100µm, (bottom right) 100x magnification, ruler = 50µm

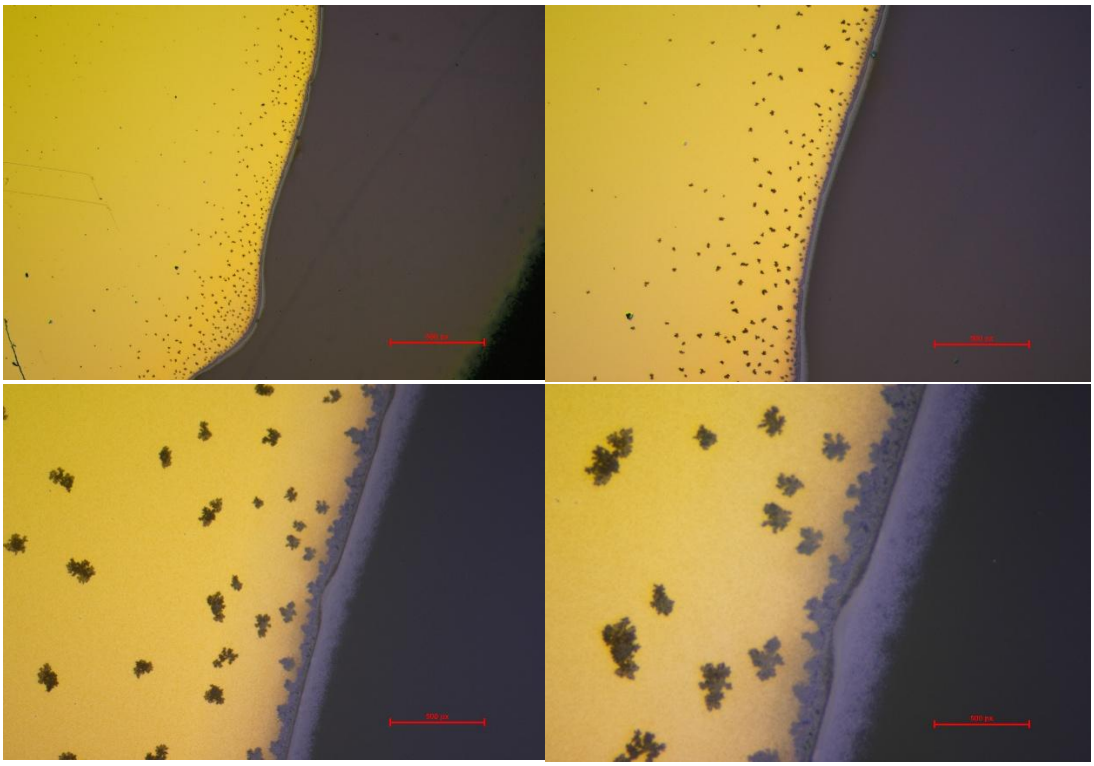

Figure 68: QCM Nr.4. visible Cr on the electrode edge when using a 1mm thick 3D-printed mask. These images all look at the outer rim of an electrode (top left) 5x magnification, ruler = 1000µm, (top right) 10x magnification, ruler = 500µm, (bottom left) 50x magnification, ruler = 100µm, (bottom right) 100x magnification, ruler = 50µm

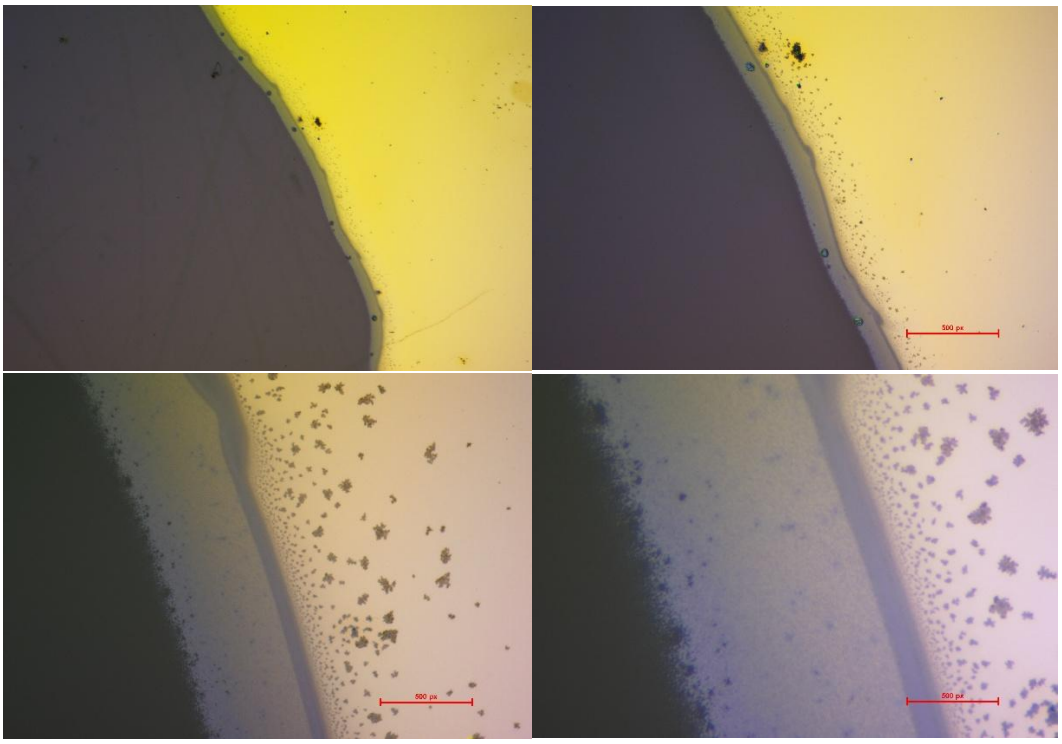

Figure 69: QCM Nr.3. visible Cr on the electrode edge when using a 1mm thick 3D-printed mask. These images all look at the inner rim of the bridge that connects the electrodes (top left) 5x magnification, ruler = 1000µm, (top right) 10x magnification, ruler = 500µm, (bottom left) 50x magnification, ruler = 100µm, (bottom right) 100x magnification, ruler = 50µm

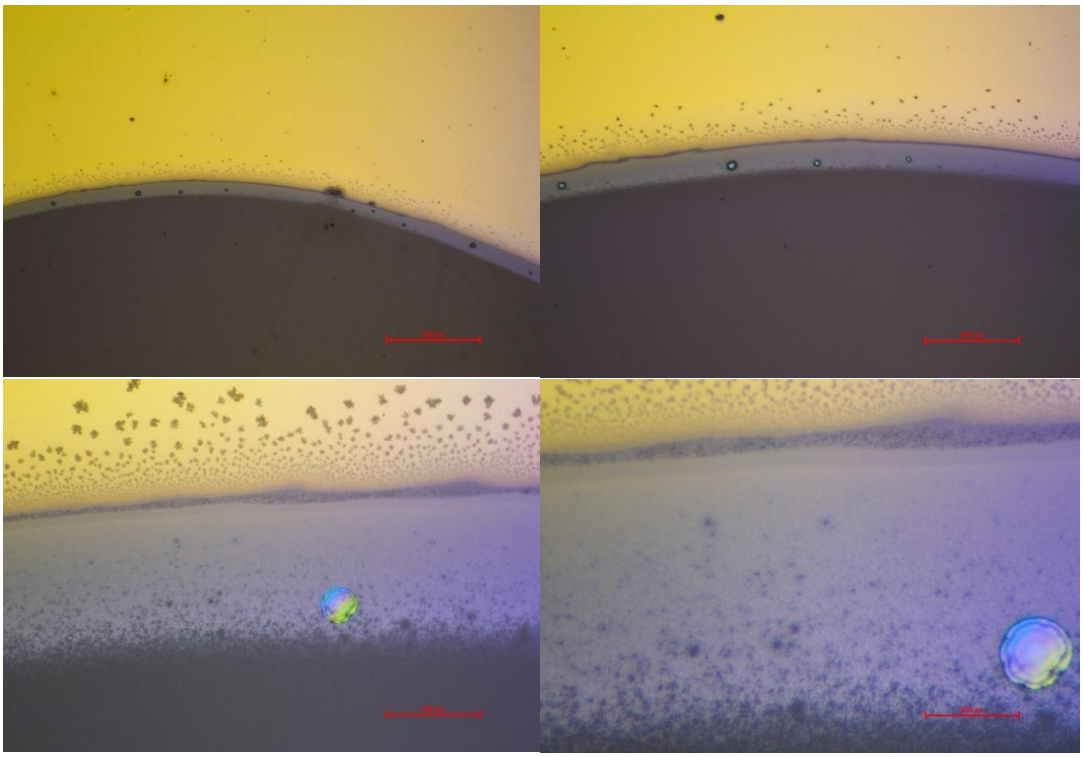

Figure 70: QCM Nr.4. visible Cr on the electrode edge when using a 1mm thick 3D-printed mask. These images all look at the inner rim of the bridge that connects the electrodes (top left) 5x magnification, ruler = 1000µm, (top right) 10x magnification, ruler = 500µm, (bottom left) 50x magnification, ruler = 100µm, (bottom right) 100x magnification, ruler = 50µm

Table 2: Averaged and rounded biggest and smallest electrode chromium borders extracted from the light microscope photos resulting from the 1mm thick masks and the 0.5mm thick masks.

	1 mm thick mask	0.5 mm thick mask
Smallest Cr Border	25µm	40µm
Biggest Cr Border	135µm	350µm

Table 2 summarizes the border sizes from the light microscope images from the different mask thicknesses. This shows that the 1mm thick masks design does indeed lead to better contact between the mask and QCMs and therefore the chromium border is generally smaller and that when the mask becomes too thin the structural integrity and contact is influenced. Since 1mm thick masks worked very well, they were taken from that point on. To see if the chromium border truly made a difference, QCM measurements were performed and the results are shown in section 4.3.3.

3D printed masks: Final design

Hence, the final design (see Figure 71-73) utilizes a flat bottom part for adhesion to the sample plate, the PDMS and protection plate to press the QCM to the mask and protect its gas side, the clipped top part and 1mm mask for better contact between mask and quartz plate and finally, locks to stabilize the assembly.

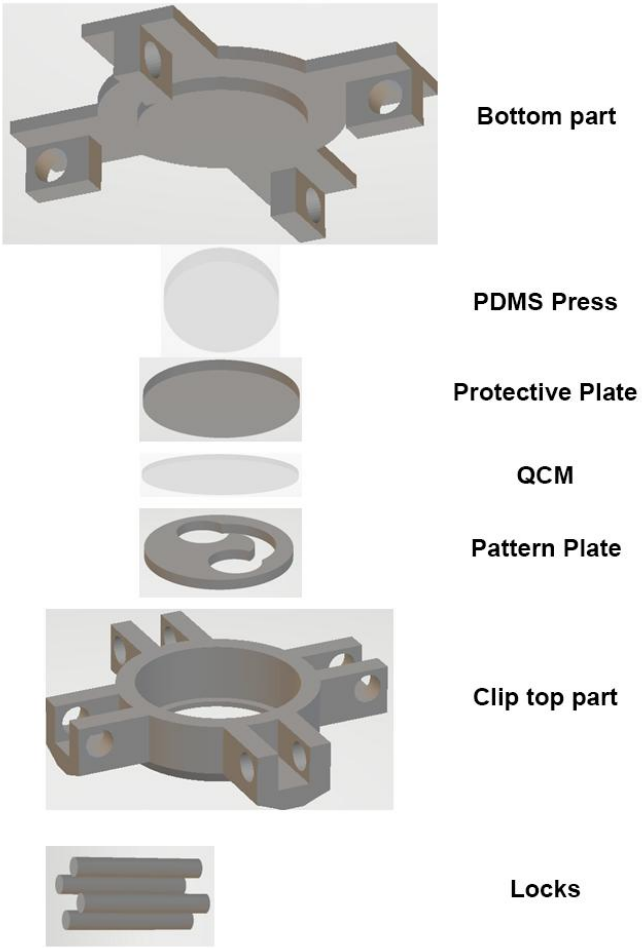

Figure 71: Final 3D-printed PVD mask design

Figure 72: A photo of how all the final mask assembly looked. (after PVD)

The advantage of this design is that it fulfills all the requirements and specifications defined: the mask is thin, the even side is on the QCMs side, the entire mask sticks to the sample plate of the PVD machine, it does not break the QCM while also allowing for pressure to improve contact, and, finally, it ensures that PVD deposits the electrodes in the center of the QCM. Placing the QCM into and removing it from the mask is also relatively simple.

Figure 73: A photo of masks after use in PVD.

4.2.2. Comparing different electrode manufacturing processes

Figure 74 shows QCM resulting from different electrode deposition processes.

Figure 74: QCMs resulting from different manufacturing methods. 1. Fully coated QCM, 2. 3D-printed mask partially coated QCM, 3. Screen printed partially coated QCM, 4. Parasol foil mask partially covered QCM, 5 Parasol foil mask and screen-printed bridge partially covered QCM.

The QCMs resulting from 3D-printed masks are far more uniform than those resulting from other methods.

Surprisingly the QCMs resulting from screen printing are less uniform than expected. Meanwhile those produced with parasol foil masks are predictably not very uniform. Figure 75 shows three different QCMs produced with parasol masks.

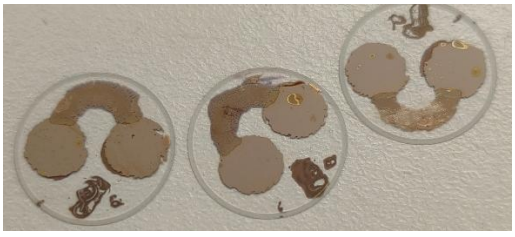

Figure 75: QCMs manufactured with parasol masks and screen printing.

The different QCM manufacturing processes were further compared with QCM measurements. The results of those measurements are being shown in section 4.3.4.

4.3. QCM design comparisons

4.3.1. QCM design comparison: The response to different AuNP concentrations

This section compares the results of different QCM measurements from the different batches. Figure 76 shows a successful example of a QCM measurement. The graph is already normalized. Normalizing is done by adjusting the graphs starting point to when the first injection occurs and normalizing the start point to zero. Tables 3 – 5 show the averaged response and noise from this and all other successful QCM measurements.

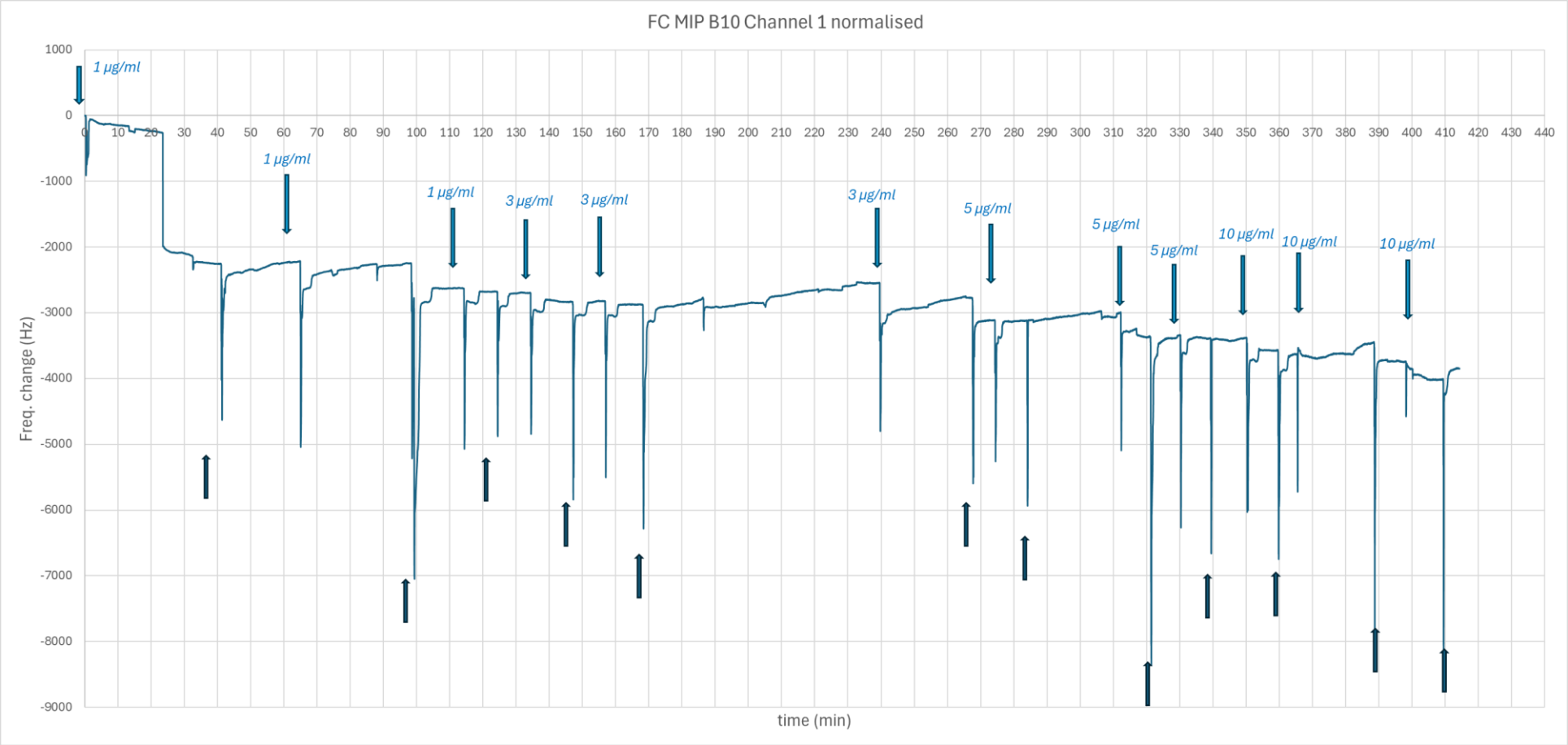

Figure 76: QCM measurement of a fully coated MIP QCM 1 of the first successful batch. The blue arrows above the curve indicate when the injections with AuNPs were performed, as well as their concentrations, while the black arrows below the curve represent washing steps with PBS.

Table 3: The extracted data of the QCM data from the first successful batch of QCMs. The table shows the average frequency change after injections/washing with the standard deviation of the average. It also shows the average standard deviation of the measurement of 40 seconds before injection to acquire the noise. (PC = partially coated, FC = fully coated)

First successful Batch	FC MIP 1		FC MIP 2		PC MIP 1		PC MIP 2		PC NIP		PC MIP thin mask		PC NIP thin mask	
Δ 1 µg/ml [ΔHz]	-774.67	+/- 1044.72	-6.11	+/- 5.47	-32.92	+/- 71.13	-655.60	+/- 922.29	-162.91	+/- 227.71	-198.44	+/- 711.70	-129.96	+/- 77.93
Δ Wash 1 [ΔHz]	-123.85	+/- 180.59	-122.86	+/- 96.82	-235.94	+/- 419.14	-17.85	+/- 74.70	-145.50	+/- 342.42	7.01	+/- 17.44	55.76	+/- 46.09
Δ 3 µg/ml [ΔHz]	-135.51	+/-69.60	86.84	+/- 109.90	-135.55	+/- 85.36	-61.85	+/- 232.36	195.59	+/- 256.75	-89.17	+/- 154.69	-118.23	+/- 132.65
Δ Wash 3 [ΔHz]	-3.33	+/- 272.63	-10.76	+/- 7.38	7.55	+/- 20.31	-66.47	+/- 224.20	-11.16	+/- 335.61	54.62	+/- 103.28	50.55	+/- 140.95
Δ 5 µg/ml [ΔHz]	-137.26	+/- 159.94	-5.07	+/- 26.84	-209.69	+/- 276.04	367.11	+/- 269.28	-27.36	+/- 20.58	-27.74	+/- 18.44	-12.66	+/- 50.59
Δ Wash 5 [ΔHz]	47.54	+/-47.99	4.28	+/- 30.38	-228.45	+/- 211.45	-286.20	+/- 322.04	10.86	+/- 155.95	-42.58	+/- 114.67	-34.56	+/- 11.84
Δ 10 µg/ml [ΔHz]	-98.30	+/- 189.26	20.08	+/- 27.36	-33.33	+/- 81.68	-36.57	+/- 226.79	10.63	+/- 47.76	50.85	+/- 95.16	-42.15	+/- 41.17
Δ Wash 10 [ΔHz]	-55.67	+/- 183.66	-101.66	+/- 105.54	27.57	+/- 64.85	-93.56	+/- 101.59	-84.72	+/- 56.90	-76.61	+/- 232.61	-24.62	+/- 64.31
Noise 1 [Hz]	2.30		0.47		2.65		2.35		0.91		2.51		0.68	
Wash Noise 1 [Hz]	2.13		0.62		1.93		2.44		2.36		1.39		0.85	
Noise 3 [Hz]	2.67		0.51		2.12		2.50		0.96		1.69		0.98	
Wash Noise 3 [Hz]	2.47		0.63		3.68		2.28		1.10		1.28		1.31	
Noise 5 [Hz]	3.84		0.50		4.47		3.04		1.45		2.32		1.63	
Wash Noise 5 [Hz]	5.09		0.56		2.95		71.50		2.01		2.46		0.76	
Noise 10 [Hz]	3.79		0.42		111.43		20.32		2.87		1.81		0.63	
Wash Noise 10 [Hz]	3.72		0.48		2.89		3.71		6.72		3.09		1.00	

Table 4: The extracted data of the QCM data from the second successful batch of QCMs. The table shows the average frequency change after injections/washing with the standard deviation of the average. It also shows the average standard deviation of the measurement of 40 seconds before injection to acquire the noise. In case there is an empty field, it is because there is no data, because not all three injections were performed.

Second successful Batch	PC MIP 3D-printed		PC NIP 3D-printed		PC MIP parasol foil mask + screen-print		PC NIP parasol foil mask + screen-print		PC MIP parasol foil mask	
Δ 1 µg/ml [ΔHz]	-38.37	+/- 49.93	-64.60	+/- 30.63	-6.31	+/- 5.02	-67.58	+/- 76.82	-83.88	+/- 60.37
Δ Wash 1 [ΔHz]	-12.11	+/- 21.45	-22.73	+/- 88.37	-7.48	+/- 10.30	-90.74	+/- 59.34	-379.77	+/- 457.80
Δ 3 µg/ml [ΔHz]	-77.62	+/- 48.30	363.81	+/- 496.02	-2.64	+/- 3.09	-14.88	+/- 44.97	591.36	+/- 387.53
Δ Wash 3 [ΔHz]	0.47	+/- 76.97	-1184.68	+/- 1131.92	-8.03	+/- 3.65	-42.73	+/- 100.56	-615.25	+/- 285.31
Δ 5 µg/ml [ΔHz]	-16.29	+/- 47.97	-94.24	+/- 72.66	2.65	+/- 3.37	-3825.28	+/- 5373.28	65.95	+/- 47.91
Δ Wash 5 [ΔHz]	-39.95	+/- 4.31	-9.92	+/- 30.65	-2.10	+/- 1.58	-526.79	+/- 1116.26	-69.04	+/- 14.70
Δ 10 µg/ml [ΔHz]	6.73	+/- 8.35	-16.87	+/- 30.03	0.66	+/- 6.53	-631.89		-53.53	+/- 79.65
Δ Wash 10 [ΔHz]	-51.20	+/- 12.07	-5.92	+/- 21.13	-3.39	+/- 12.66	14337.17		12.87	+/- 163.59
Noise 1 [Hz]	0.77		1.29		0.44		1.02		1.39	
Wash Noise 1 [Hz]	0.67		3.60		0.33		0.75		1.57	
Noise 3 [Hz]	0.73		2.95		0.29		0.83		3.73	
Wash Noise 3 [Hz]	2.46		2.09		0.28		1.13		1.31	
Noise 5 [Hz]	1.67		1.28		0.29		319.70		1.62	
Wash Noise 5 [Hz]	1.05		1.72		0.37		17.77		1.87	
Noise 10 [Hz]	1.95		0.89		0.36				2.20	
Wash Noise 10 [Hz]	1.69		0.92		0.41				3.52	

Table 5: The extracted data of the QCM data from the third successful batch of QCMs. The table shows the average frequency change after injections/washing with the standard deviation of the average. It also shows the average standard deviation of the measurement of 40 seconds before injection to acquire the noise.

Third successful Batch	FC MIP 1		FC MIP 2		FC NIP		PC MIP		PC NIP	
Δ 1 µg/ml [ΔHz]	-26.00	+/- 35.29	-20.72	+/- 81.23	-12.18	+/- 4.76	-192.82	+/- 93.96	29.28	+/- 53.93
Δ Wash 1 [ΔHz]	-30.23	+/- 64.67	-103.36	+/- 229.54	-20.18	+/- 14.07	-56.78	+/- 487.34	-220.02	+/- 279.14
Δ 3 µg/ml [ΔHz]	2.13	+/- 2.31	-80.51	+/- 84.27	-13.11	+/- 6.92	32.00	+/- 22.64	88.85	+/- 118.56
Δ Wash 3 [ΔHz]	-5.77	+/- 2.55	65.48	+/- 43.03	-3.43	+/- 20.32	-161.64	+/- 990.03	-104.04	+/- 182.72
Δ 5 µg/ml [ΔHz]	2.41	+/- 2.65	-49.04	+/- 42.94	-7.46	+/- 3.46	-18.41	+/- 34.55	-2.02	+/- 29.97
Δ Wash 5 [ΔHz]	-9.64	+/- 1.82	-12.36	+/- 68.67	-12.31	+/- 6.21	39.92	+/- 18.24	-13.10	+/- 278.49
Δ 10 µg/ml [ΔHz]	-5.72	+/- 2.97	29.61	+/- 41.59	-3.49	+/- 1.30	-46.10	+/- 107.26	-12.11	+/- 50.43
Δ Wash 10 [ΔHz]	-1.98	+/- 2.73	10.60	+/- 12.11	-1.35	+/- 2.57	-1030.65	+/- 1408.92	-9.78	+/- 307.33
Noise 1 [Hz]	0.40		0.51		0.48		1.78		-160.31	
Wash Noise 1 [Hz]	0.38		0.97		0.51		3.11		1.13	
Noise 3 [Hz]	0.45		0.45		0.40		1.67		1.21	
Wash Noise 3 [Hz]	0.41		0.91		0.40		1.14		1.72	
Noise 5 [Hz]	0.43		0.95		0.39		1.54		1.43	
Wash Noise 5 [Hz]	0.39		0.99		0.42		1.70		1.56	
Noise 10 [Hz]	0.39		0.39		0.44		2.08		1.43	
Wash Noise 10 [Hz]	0.37		4.12		0.40		3.23		1.31	

In the second successful batch, all fully coated QCMs as well as the NIP of the parasol foil mask broke in the QCM cell, which is why the data from that batch could not be used for the design comparison and was only used for the comparison of preparation methods.

To analyze if there is a difference in responses between the designs, they were both compared by calculating the response ratio between the averages of the response. In Table 6 the ratios between QCM designs for each produced batch are shown. In Table 7 the noise of each QCM design is shown depending on the injection concentration.

Table 6: The ratio between the responses in a batch between the fully coated and partially coated QCM designs for each injection concentration. As well as the average ratio.

	Ratio between response of FC:PC of the first successful batch	Average ratio between response of FC:PC of the third successful batch	Average response across batches
Δ 1 µg/ml	1.18	0.12	0.65
Δ Wash 1	6.94	1.18	4.06
Δ 3 µg/ml	2.19	-1.22	0.48
Δ Wash 3	0.05	-0.18	-0.07
Δ 5 µg/ml	-0.37	1.27	0.45
Δ Wash 5	-0.17	-0.28	-0.22
Δ 10 µg/ml	2.69	-0.26	1.21
Δ Wash 10	0.59	0.00	0.30

Table 7: The average noise of all successfully created QCMs divided into fully coated design and partially coated design as well as MIP and NIP.

	FC MIP all	FC NIP all	PC MIP all	PC NIP all
Noise 1 µg/ml	0.92	0.48	1.89	-52.70
Noise wash 1 µg/ml	1.02	0.51	2.04	2.36
Noise 3 µg/ml	1.02	0.40	1.76	1.70
Noise wash 3 µg/ml	1.10	0.40	2.39	1.64
Noise 5 µg/ml	1.43	0.39	2.68	1.39
Noise wash 5 µg/ml	1.76	0.42	19.30	1.76
Noise 10 µg/ml	1.25	0.44	33.94	1.73
Noise wash 10 µg/ml	2.17	0.40	2.88	2.98

While this tends to show lower responses for the fully coated designs, it is unclear whether the result is significantly affected by the design: the high distribution of the frequency changes, the low number of successful batches and the occurrence of differing ratios for both design types. The data thus does not seem to yield a linear correlation between AuNP concentration and sensor response.

To make the results of the noise more representative of the median, any single significantly deviating noise signal was removed from the average in Table 8.

Table 8: The average noise of all successfully created QCMs without the results that widely differed from the norm divided into fully coated design and partially coated design as well as MIP and NIP. The ratio between the noises of fully coated and partially coated designs are also showcased.

	FC MIP all adjusted	FC NIP all adjusted	PC MIP all adjusted	PC NIP all adjusted	Ratio MIP FC:PC	Ratio NIP FC:PC
Noise 1 µg/ml	0.46	0.48	1.89	1.10	0.24	0.44
Noise wash 1 µg/ml	0.65	0.51	2.04	2.36	0.32	0.21
Noise 3 µg/ml	0.47	0.40	1.76	1.70	0.27	0.24
Noise wash 3 µg/ml	0.65	0.40	2.39	1.64	0.27	0.24
Noise 5 µg/ml	0.63	0.39	2.68	1.39	0.23	0.28
Noise wash 5 µg/ml	0.65	0.42	1.90	1.76	0.34	0.24
Noise 10 µg/ml	0.40	0.44	2.01	1.73	0.20	0.25
Noise wash 10 µg/ml	1.66	0.40	2.88	2.98	0.58	0.13
Average					0.31	0.26

Comparing the ratios from Table 8 reveals that the noise of the fully coated designs is only 13% to 58% as high as for partially coated designs. On average the noise of the fully coated MIPs is only 31% and for the fully coated NIPs 26% of the ones for the partially coated QCMs. This means the noise is very consistently lower for the fully coated designs.

4.3.2. QCM design comparison: the response to different background concentrations

Varying the PBS buffer concentration at constant AuNP concentration leads to a different result. In Figure 77 one of the QCM measurements analyzing the background is shown and the extracted data of these measurements is visible in Table 9.

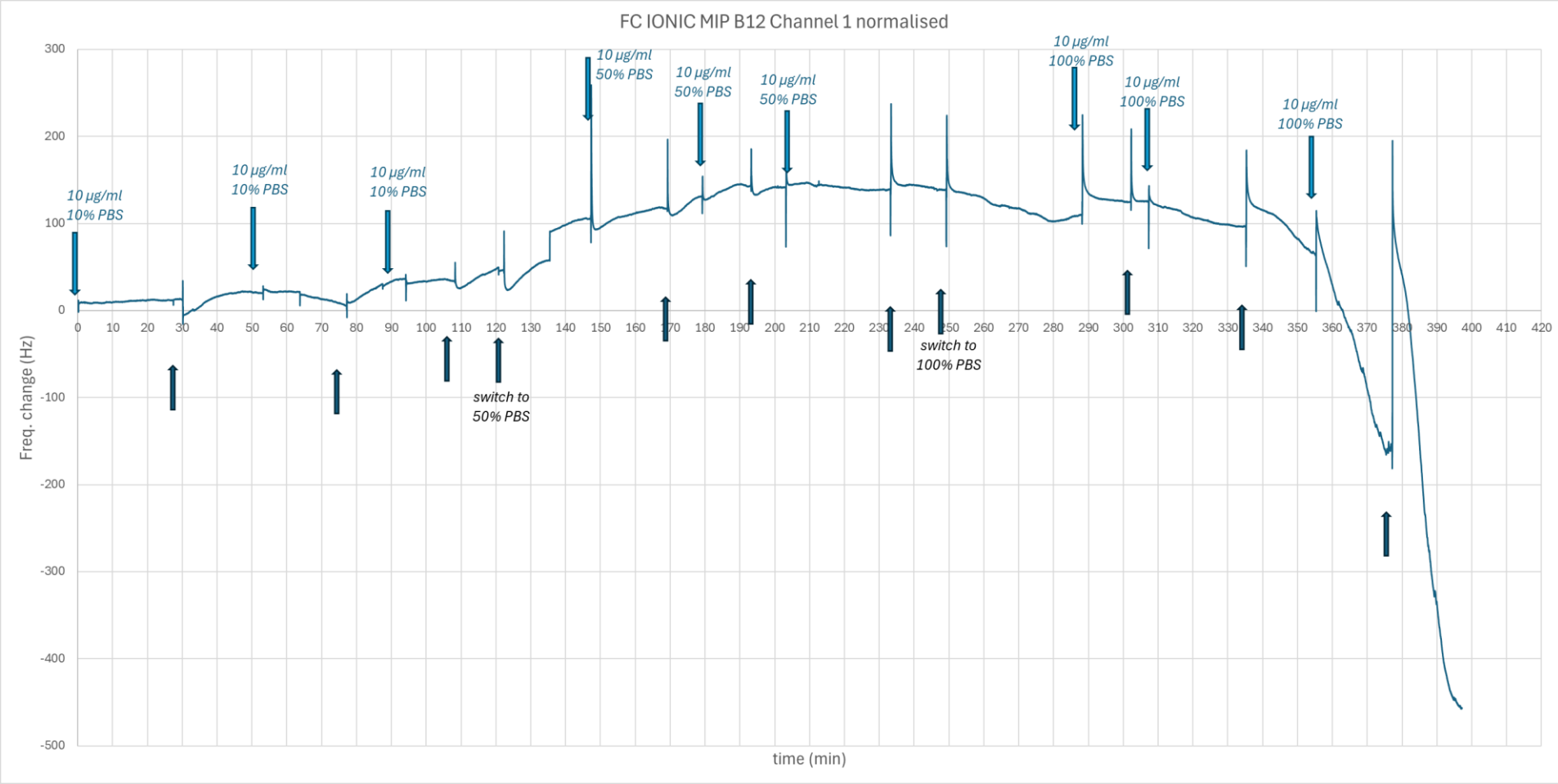

Figure 77: QCM measurement of a fully coated MIP QCM influence of the ionic background of the third successful batch. The injected amount of NPs was always the same, the PBS background concentration was changed after every third NP injection. The blue arrows above the curve with writing indicate when the injections with AuNPs were performed as well as their concentration, while the black arrows below the curve represent washing steps with PBS with writing when the background was changed from 10% PBS, to 50% to 100%

Table 9: The extracted data of the QCM data from the third successful batch of QCMs ionic measurements. The table shows the average frequency change after injections/washing with the standard deviation of the average. It also shows the average standard deviation of the noise of 40 seconds before injection.

Third successful Batch IONIC	FC MIP		FC NIP		PC MIP		PC NIP	
Δ 10% PBS 10 µg/ml AuNP [ΔHz]	-1.12	+/- 10.82	-22.34	+/- 43.93	-33.96	+/- 66.65	-268.64	+/- 329.28
Δ Wash 10% PBS [ΔHz]	16.38	+/- 9.81	-224.59	+/- 65.30	-203.40	+/- 408.77	-75.85	+/- 98.08
Δ 50%PBS 10 µg/ml AuNP [ΔHz]	7.06	+/- 6.86	-33.54	+/- 47.63	-318.87	+/- 225.98	52.08	+/- 137.25
Δ Wash 50% PBS [ΔHz]	4.06	+/- 6.82	7.05	+/- 26.42	74.62	+/- 68.51	-112.00	+/- 98.82
Δ 100%PBS 10 µg/ml AuNP [ΔHz]	-79.21	+/- 103.67	-15.46	+/- 54.28	-8.04	+/- 335.44	-42.38	+/- 17.22
Δ Wash 100% PBS [ΔHz]	-109.19	+/- 134.12	-3.18	+/- 9.75	-3.02	+/- 363.30	58.84	+/- 33.80
Switch from 10% to 50% PBS	59.16		-109.55		237.17		-276.44	
Switch from 50% to 100% PBS	-28.85		-39.41		-49.98		-11.80	
Noise 10% PBS 10 µg/ml AuNP [Hz]	0.80		0.38		7.60		1.13	
Wash Noise 10% PBS [Hz]	1.05		0.22		1.29		1.12	
Noise 50% PBS 10 µg/ml AuNP [Hz]	0.38		0.31		3.50		4.97	
Wash Noise 50% PBS [Hz]	0.45		0.24		4.21		1.32	
Noise 100% PBS 10 µg/ml AuNP [Hz]	0.31		1.00		68.32		1.09	
Wash Noise 100% PBS [Hz]	0.46		0.77		161.16		1.89	

Like in previous QCM measurements, a ratio between responses and noise was calculated for NIPs and the MIPs to compare the data on a mathematical basis (see Table 10 and Table 12).

Table 10: The ratio between the responses between the fully coated and partially coated QCM designs in a QCM measurement with changing electrolyte concentrations.

	Ratio between responses of MIPs FC:PC	Ratio between responses of NIPs FC:PC
Δ 10%PBS 10 µg/ml AuNP [ΔHz]	0.03	0.08
Δ Wash 10% PBS [ΔHz]	-0.08	2.96
Δ 50%PBS 10 µg/ml AuNP [ΔHz]	-0.02	-0.64
Δ Wash 50% PBS [ΔHz]	0.05	-0.06
Δ 100%PBS 10 µg/ml AuNP [ΔHz]	9.86	0.36
Δ Wash 100% PBS [ΔHz]	36.12	-0.05
Switch from 10% to 50% PBS	0.25	0.40
Switch from 50% to 100% PBS	0.58	3.34

While the responses of the partially covered QCMs tends to be higher, at times the response of the fully coated QCMs is stronger. Since the distributions widely differ it is inconclusive if the response is actually influenced by the QCM design. Looking solely at the influence of the background solution (see Table 11) by calculating and analyzing the ratio between the switch of PBS concentrations. The ratios between the background switches are formed because the response differed wildly between QCMs.

Table 11: Ratios between the response of the first and second electrolyte switch.

	FC	PC
MIP	-2.05	-4.75
NIP	2.78	23.42

In general, switching from 10% to 50% PBS leads to significantly higher effects than going from 50% to 100% PBS. Analyzing Table 11 showcases that PC QCMs show a significantly stronger relative response to the change of the background. So, FC QCMs are not as strongly influenced by the background as PC QCMs.

Table 12: The ratio between the noises of fully coated and partially coated designs for MIPs and NIPs

	Ratio between responses of MIPs FC:PC	Ratio between responses of NIPs FC:PC
Noise 10%PBS 10 µg/ml AuNP	0.050	0.707
Noise Wash 10% PBS	0.170	0.936
Noise 50%PBS 10 µg/ml AuNP	0.087	0.076
Noise Wash 50% PBS	0.058	0.336
Noise 100%PBS 10 µg/ml AuNP	0.015	0.285
Noise Wash 100% PBS	0.005	0.244
Average	0.06	0.43

The noise was also analyzed again and as was the case before, the noise is significantly lower for fully coated QCMs than for partially coated QCMs, no matter the background composition (Table 12). On average the noise for FC QCMs was only 6% of the noise of PC QCMs for MIPs and 43% for NIPs.

4.3.3. QCM mask design comparison: influence of chromium border

To see whether the chromium border truly made a difference, the QCMs from the first successful batch were analyzed by regular QCM measurement and compared. In Table 3 the extracted data is visible. In Table 13 the response and noise ratios between the partially coated thinner and thicker masks are visible.

Table 13: Ratios between the QCM measurement data of QCMs resulting from thinner masks and thicker masks. The high noise in the higher concentrations is due to time running out, which made it impossible to wait for full stabilization

	Ratio between 3D printed masks with different thicknesses. MIP 1mm:0.5mm	Ratio between 3D printed masks with different thicknesses. NIP 1mm:0.5mm
Δ 1 µg/ml	1.73	1.25
Δ Wash 1	-18.10	-2.61
Δ 3 µg/ml	1.11	-1.65
Δ Wash 3	-0.54	-0.22
Δ 5 µg/ml	-2.84	2.16
Δ Wash 5	6.04	-0.31
Δ 10 µg/ml	-0.69	-0.25
Δ Wash 10 µg/ml	0.43	3.44
Noise 1	1.00	3.91
Noise wash 1	1.57	2.27
Noise 3	1.37	2.17
Noise wash 3	2.32	2.82
Noise 5	1.62	2.74
Noise wash 5	15.12	3.88
Noise 10	36.35	175.86
Noise wash 10	1.07	2.88

The response tends to be a bit higher with the 1mm thick masks, but surprisingly the noise of the 1mm thick masks was also higher in all cases than the noise with the thinner 0.5mm masks. This means that the bigger chromium border resulting from the thinner masks does not significantly impede the response, while improving the noise. A drawback of the thinner masks is that the resulting QCMs take a lot longer to stabilize their signal in liquid phase. Despite the fact that the thinner masks actually improve the noise, the QCM measurements were already well underway and therefore were continued with the regular 1mm thick masks.

4.3.4. Comparing electrode manufacturing process influence on QCM measurements

In Table 4 the data extracted from the QCM measurements of different manufacturing processes is shown. Table 14 shows the compared response and noise of Table 4. This section only compares the data of the partially coated QCMs of different electrode manufacturing processes.

Table 14: Ratios between the different production methods responses and noises. The empty fields represent when the connection of the QCM was lost.

	Ratio between 3D printed mask and parasol mask MIP 3D:pm	Ratio between 3D printed mask and parasol mask with screen printed bridge MIP 3D:pmsp	Ratio between 3D printed mask and parasol mask with screen printed bridge NIP 3D:pmsp
Δ 1 µg/ml	0.46	6.08	0.96
Δ Wash 1	0.03	1.62	0.25
Δ 3 µg/ml	-0.13	29.39	-24.45
Δ Wash 3	0.00	-0.06	27.73
Δ 5 µg/ml	-0.25	-6.14	0.02
Δ Wash 5	0.58	19.05	0.02
Δ 10 µg/ml	-0.13	10.18	0.08
Δ Wash 10 µg/ml	-3.98	15.11	
Noise 1	0.55	1.73	1.26
Noise wash 1	0.43	2.01	4.83
Noise 3	0.20	2.52	3.53
Noise wash 3	1.88	8.75	1.85
Noise 5	1.03	5.72	0.00
Noise wash 5	0.56	2.83	0.10
Noise 10	0.89	5.35	0.39
Noise wash 10	0.48	4.16	
Average noise	0.75	4.13	1.71

It is evident that the 3D-printed masks yield QCMs with lower noise on average than parasol masks, but also to lower effects. If the noise result is averaged the noise of the QCMs produced by 3D-printed mask is only 75% of that of the ones made by parasol mask. But since only one QCM was successfully manufactured with a parasol mask, it means this is a non reproducible single result that may not be conclusive. It is assumed the noise is higher because of the less uniform and uneven edges of the resulting QCMs.

Surprisingly, QCMs created with parasol masks and a screen-printed bridge display a lower noise, than the noise of the QCMs created by 3D-printed masks. On the NIP the response was on average 16 times higher due to the higher surface roughness. Since the response is also very high on washing steps, it means the increase in surface roughness leads to false responses and essentially impedes quantitative measurements. Contrary to that, the response of the MIP basically disappeared: the average response of the QCMs resulting from parasol foil masks and screen printing was only 1/8 of that of a QCM from a 3D-printed mask. Since these measurements are inconsistent, it is reasonable to disregard the method of parasol masks and screen printing for reliable QCM production.

QCM measurements with fully screen-printed electrodes were performed as well, but none of the measurements were successful. After injection of the AuNPs, the resonance frequency would always increase or decrease until a loss of connection occurred. It is suspected this occurs because of higher surface roughness.

Finally, Figures 78 to 80 show the electrodes surfaces of QCMs produced by different manufacturing processes recorded with AFM.

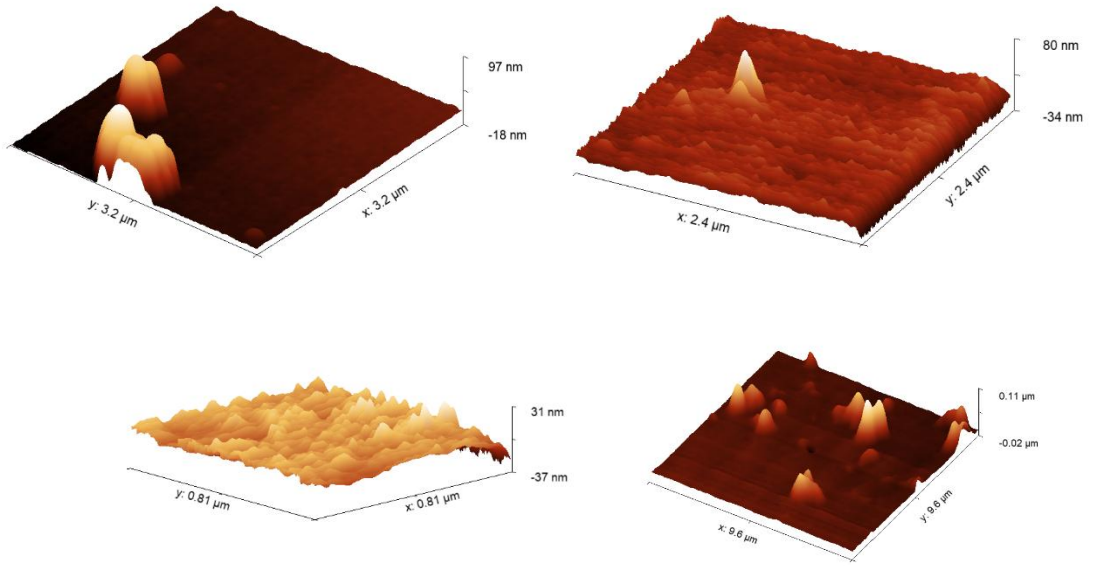

Figure 78: AFM images of the surface of a fully coated QCM (this means PVD surface) after the QCM measurement and washing. What is seen here is (top left) AuNPs on the surface of the QCM (tapping mode AFM), (top right) AuNP in a cavity (contact mode AFM), (bottom left) just the surface roughness without any NPs (contact mode AFM), (bottom left) the surface with AUNPs and a cavity (tapping mode AFM)

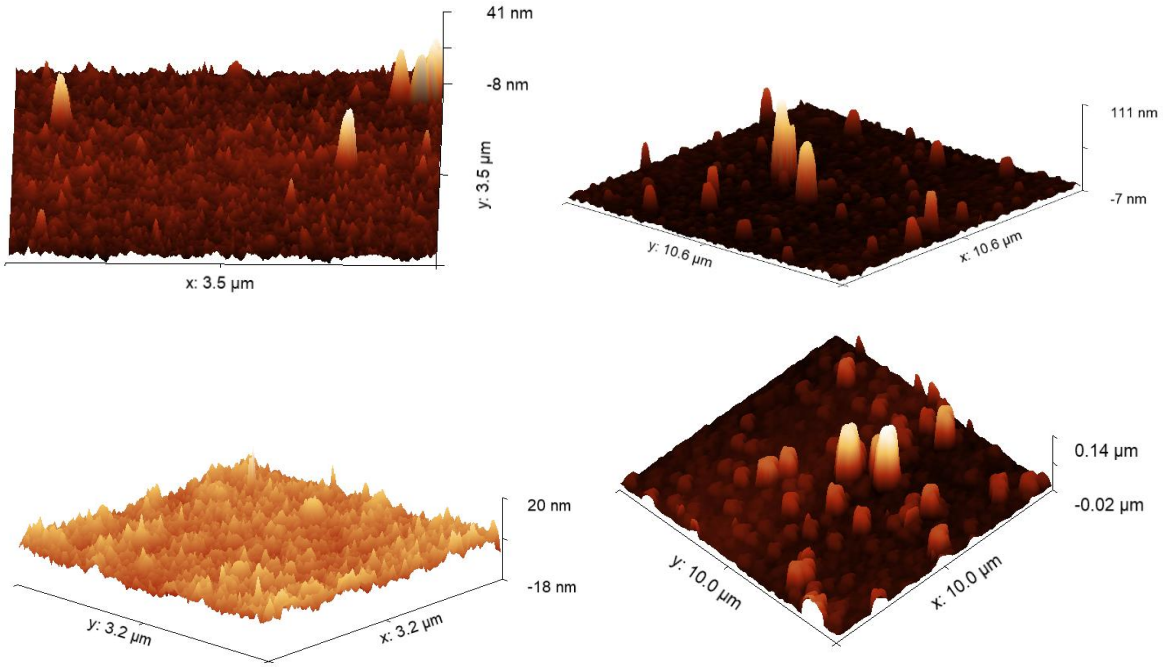

Figure 79: AFM images of the surface of a partially coated QCM, made with parasol masks, after the QCM measurement and washing. What is seen is (top left) the surface of a MIP (contact mode AFM), (top right) Surface of the MIP with some AuNPs in cavities (tapping mode AFM), (bottom left) surface roughness of the NIP surface (contact mode AFM), (bottom right) surface of NIP with suspected AuNPs clumping on surface (tapping mode AFM)

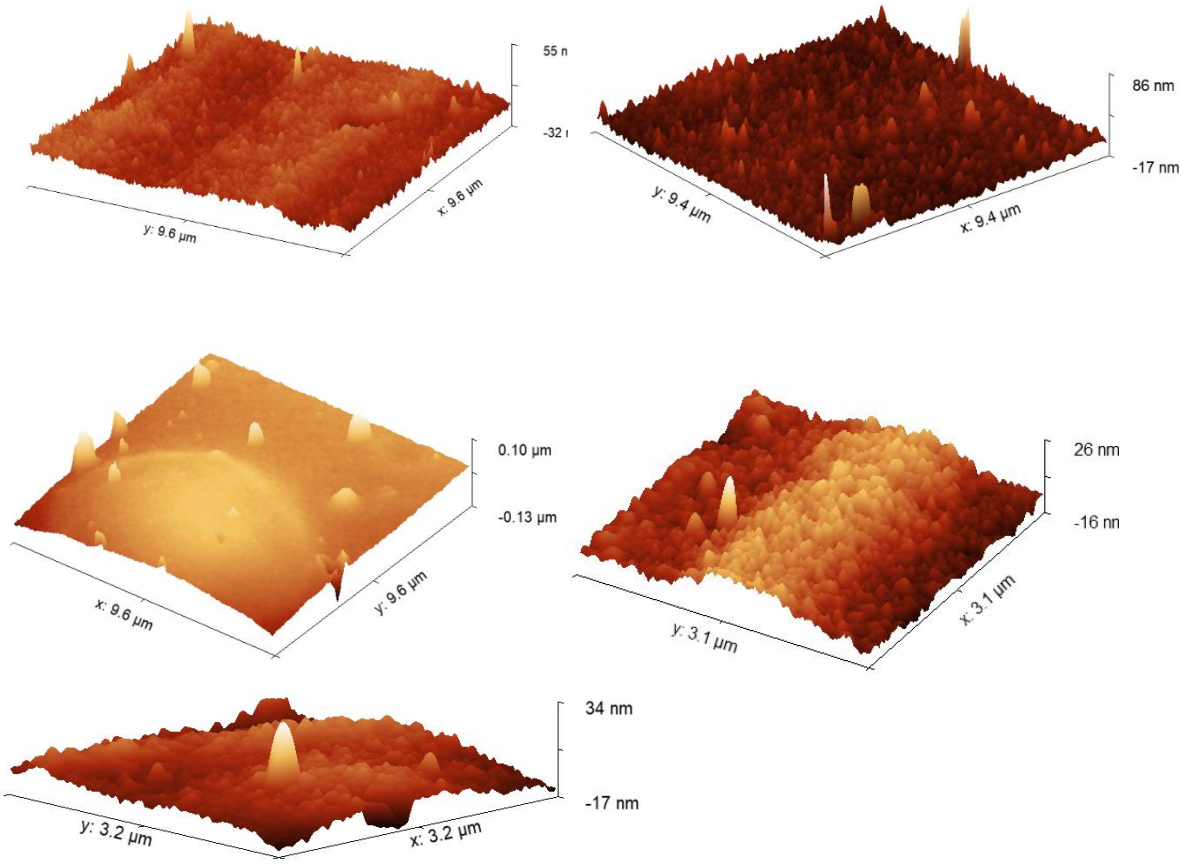

Figure 80: AFM images of the surface of a partially coated QCM, made with screen printing, after the QCM measurement and washing. What is seen is (top left) the surface of a NIP to show the roughness (contact mode AFM), (top right) the surface of the NIP and how there are higher irregularities (contact mode AFM), (middle left) the surface of the MIP and how the paste can create bigger deposits at times (tapping mode AFM), (middle right) surface of MIP and how the gold paste can lead to patches of more even surfaces too (contact mode AFM), (bottom left) irregularity of surface (contact mode AFM)

Overall, the surfaces of the fully coated and the surface of the partially coated QCMs manufactured using PVD masks are very similar. This means that deposition with a PVD mask should lead to a QCM with the same surface properties as one without. At the same time the surface of the screen-printed electrodes (Figure 80) substantially differs from the other two. Due to the surface tension and viscosity of the paste, it accumulates unevenly leading to different film thicknesses. The surface is so rough that the expected cavity depth of ~35nm is exceeded and the AuNPs can diffuse into the surface roughness itself, leading to irregular responses and higher noise. This throws off the QCM measurements of QCMs with screen-printed electrodes. QCMs with a screen-printed bridge are suspected to be so inconsistent for the same reason.

In conclusion producing QCMs with 3D-printed PVD masks leads to very reproducible QCMs with a surface that allows for stable and measurements with low noise.

4.3.5. QCM surface characterization

Characterization with SEM

Figure 81 shows SEM images of the surface of a successfully manufactured QCM.

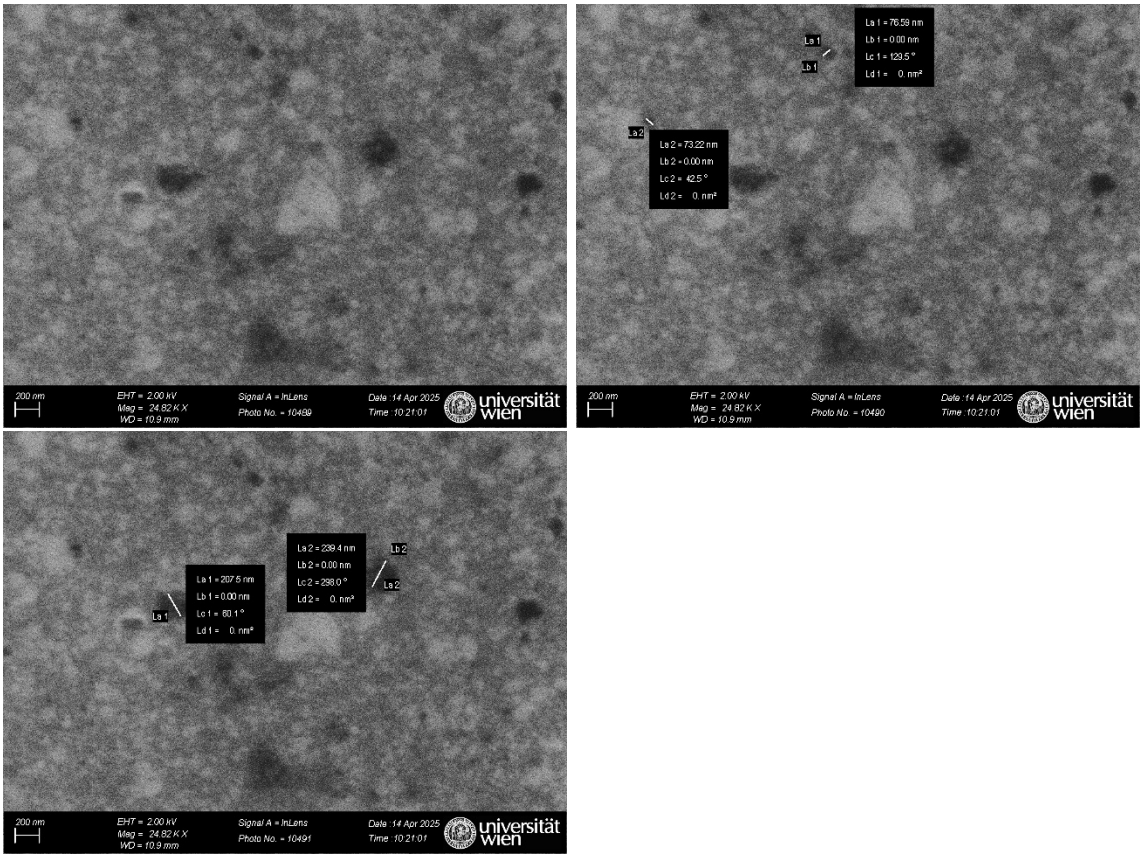

Figure 81: SEM image of the surface of the fully coated MIP from the first successful batch. (top left) image of surface (top right) image of surface with analyzed holes around the size the cavities should be, (bottom left) image of surface with analyzed holes larger than the expected size of cavities. those can originate from clustering

Overall, the surfaces of different QCMs showed the same features over different batches and manufacturing processes. On all QCMs AuNPs were still present from the prior QCM measurement. There are no noticeable differences between the surfaces deposited with or without 3D-printed mask. Differences are only noticeable between MIP and NIP. When QCMs with MIPs were analyzed, the cavities were sometimes hard to find, but visible, while there are fewer to no cavities found in the QCMs with NIPs. This was true for both the fully coated and partially coated QCMs. The surface of both designs looked basically indistinguishable.

Due to the small sizes of the nanoparticles and cavities and heating of the gold surface by the electron beam it was quite difficult to generate an image with a high focus.

Characterization with AFM

Figure 82 shows a typical AFM image of the surface of a MIP QCM. Same as with SEM, images of the surface of PC and FC QCMs look very similar. Differences between QCM surfaces only occur between MIP and NIP surfaces. On surfaces of MIPs one can see both cavities and AuNPs, while surfaces of NIPs only reveal AuNPs.

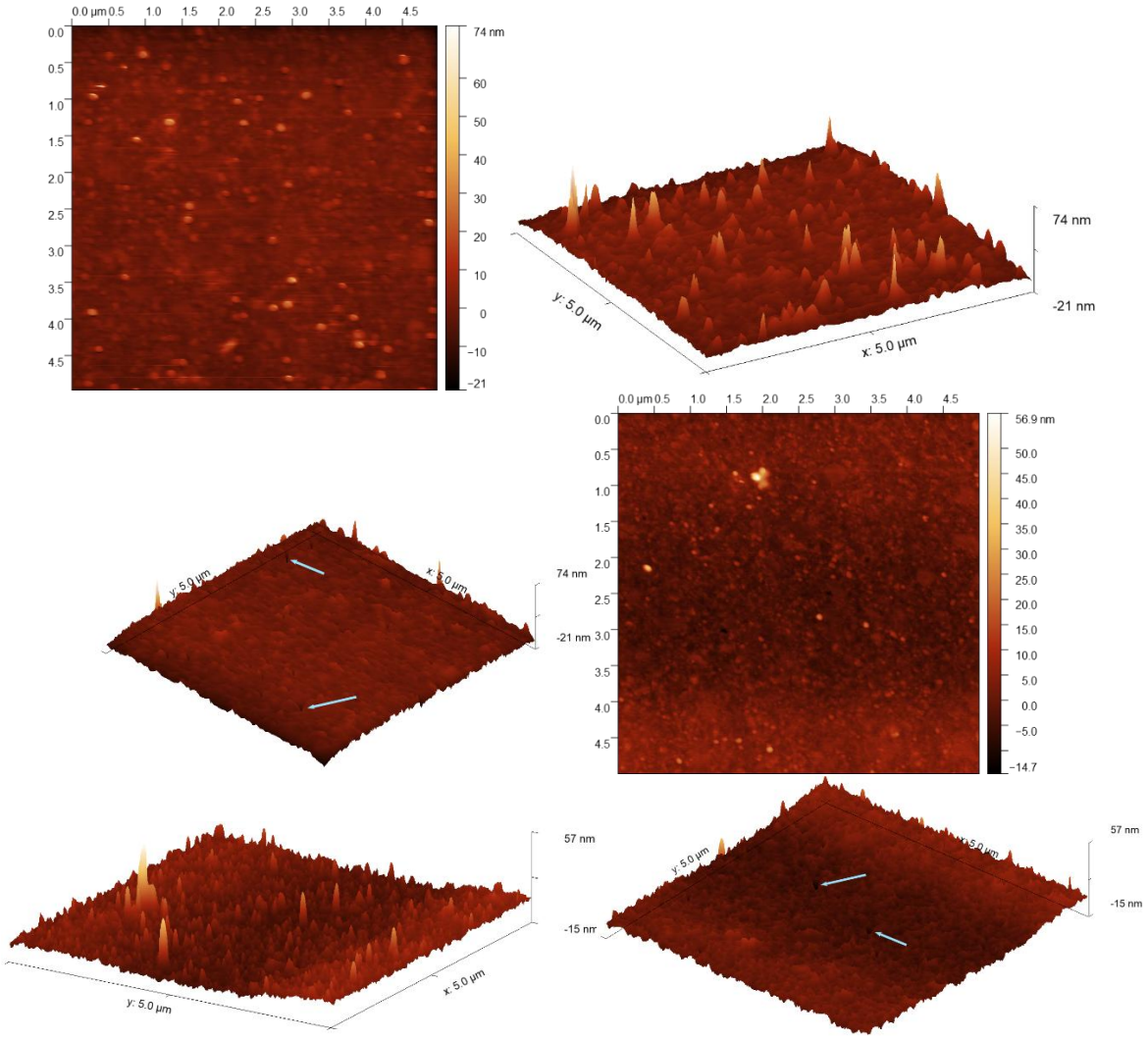

Figure 82: AFM images generated of the partially coated MIP QCM of the third batch. (top left) the measured QCM surface birds eye view 1 contact mode, (top right) top view 3D image view of the image 1 contact mode, with some AuNPs in cavities (middle left) bottom 3D image view of image 1 contact mode. One can see some pointed out cavities (middle right) the measured QCM surface birds eye view 2 tapping mode, (bottom left) top 3D image view of the image 2 tapping mode. There are some prominent spots that are believed to be AuNPs in cavities (bottom right) bottom 3D image view of the image 2 tapping mode. You can see some pointed out cavities and how much less prevalent they are compared to the ones in contact mode.

Figure 82 reveals how differently cavities are displayed by contact and tapping mode AFM. What becomes apparent from these images is that the cavities themselves are better visible with tapping mode AFM. At the same time, it is shown that the contact mode does tend to display the AuNPs in cavities better.

Typically, the surface of MIPs tends to be slightly rougher, which meets the expectations because of imprinting. The NIPs meanwhile tend to display less cavities, but also fewer AuNPs. Cavities can form naturally during washing if a part of the polymer surface is washed off, which is why in some cases “cavities” are seen on NIPs, but these cavities did tend to be a lot larger than the ones forming from imprinting.

Overall, characterization with SEM and AFM was successful and the AuNPs did form cavities successfully and are capable of diffusing into them. Also, the manufacturing of electrodes with 3D-printed masks, does not significantly influence the surface of the electrode.

5. Summary and conclusions

Over the course of the thesis a way of producing a specific pattern on a QCM with 3D-printed mask was developed and the way in which the electrode pattern on the QCM influences the measurements was analyzed. The developed design (see Figure 71) was optimized for the highest adherence between mask and QCM, high structural integrity of the mask, was thin enough near the QCM to allow for a good deposition of gold/chromium and was made to stick to the PVD deposition plate. The influence of the electrode manufacturing process of the partially coated QCMs on the quality of the QCM measurement was investigated. PVD deposited electrodes produced with the 3D printed masks lead to the overall most stable results compared to other electrode manufacturing methods of partially coated QCMs. The advantage found was that producing QCMs with 3D-printed masks and PVD, lead to a very even surface granted by PVD deposition, while also leading to very reproducible QCMs. When comparing the results of the two different QCM designs, it turns out that the response does not linearly correlate with the concentration of the AuNPs. The fully coated QCM design across measurements show a lower noise of ~25% on average. When the influence of the background composition was compared, it showed that the noise of the fully coated QCMs was also significantly lower than that of the partially coated QCMs. At the same time the influence of changing the background composition was lower for fully coated QCMs than for partially coated QCMs. The surfaces of different QCMs were characterized by SEM and AFM, which indicated that imprinting was successful despite no linear response and the surface of partially coated QCMs was not influenced by the 3D-printed masks.

The thesis also successfully shows that the electrode designs and manufacturing procedure have a significant influence on QCMs. The design and manufacturing process of the electrodes influence especially the noise and the background of QCM measurements. Ultimately, it was shown that the fully coated QCMs are preferable to the partially coated ones. Backtracking to the original goal, it means the field lines from the QCM electrodes reaching into the analyzed liquid, do influence the measurement and by using fully coated QCMs, and with that reducing these field lines, it does improve the measurements.

Since no linear correlation between the AuNPs concentration and the response could be established, influence of the electrode design on the response was inconclusive. For that reason, a repeat of QCM measurements with the analyzed designs with a different analyte would be ideal for future research.

Literature

[1] Songkhla, S. N., & Nakamoto, T. (2021). Overview of quartz crystal microbalance behavior analysis and measurement. In Chemosensors (Vol. 9, Issue 12). MDPI. https://doi.org/10.3390/chemosensors9120350

[2] Mujahid, A., Afzal, A., & Dickert, F. L. (2019). An overview of high frequency acoustic sensors—QCMs, SAWs and FBARs—chemical and biochemical applications. In Sensors (Switzerland) (Vol. 19, Issue 20). MDPI AG. https://doi.org/10.3390/s19204395

[3] Tressler, J. F., Alkoy, S., & Newnham, R. E. (1998). Piezoelectric Sensors and Sensor Materials. In Journal of Electroceramics (Vol. 2, Issue 4).

[4] Poole, I. (n.d.). Quartz Crystal Cuts: AT, BT, SC, CT . . https://www.electronics-notes.com/. Retrieved May 2, 2025, from https://www.electronics-notes.com/articles/electronic_components/quartz-crystal-xtal/crystal-resonator-cuts-at-bt-sc-ct.php

[5] O'sullivan, C. K., & Guilbault, G. G. (1999). Commercial quartz crystal microbalances-theory and applications. In Biosensors & Bioelectronics (Vol. 14). www.elsevier.com

[6] Urbakh, M., & Daikhin, L. (1998). Surface morphology and the quartz crystal microbalance response in liquids. In Colloids and Surfaces A: Physicochemical and Engineering Aspects (Vol. 134).

[7] Urbakh, M., & Daikhin, L. (2836). Influence of the Surface Morphology on the Quartz Crystal Microbalance Response in a Fluid (Vol. 10). https://pubs.acs.org/sharingguidelines

[8] Perrier, S. (2017). 50th Anniversary Perspective: RAFT Polymerization - A User Guide. In Macromolecules (Vol. 50, Issue 19, pp. 7433–7447). American Chemical Society. https://doi.org/10.1021/acs.macromol.7b00767

[9] Moad, G., Rizzardo, E., & Thang, S. H. (2013). RAFT polymerization and some of its applications. Chemistry - An Asian Journal, 8(8), 1634–1644. https://doi.org/10.1002/asia.201300262

[10] Liu, Y., Pan, B., Li, H., Lang, D., Zhao, Q., Zhang, D., Wu, M., Steinberg, C. E. W., & Xing, B. (2020). Can the properties of engineered nanoparticles be indicative of their functions and effects in plants? Ecotoxicology and Environmental Safety, 205. https://doi.org/10.1016/j.ecoenv.2020.111128

[11] Abdullah, Avin & Mohammed, Azad. (2019). Scanning Electron Microscopy (SEM): A Review.

[12] Ul-Hamid, A. (2018). A Beginners' guide to scanning Electron Microscopy. In Springer eBooks. p. 1-17, 77-82, 131 https://doi.org/10.1007/978-3-319-98482-7

[13] https://www.jove.com/v/5656/scanning-electron-microscopy-sem-operation-image-analysis

[14] What is SEM Analysis and Why Is It Important? (2024, January). Secat. https://secat.net/sem-analysis-use-importance/

[15] Scanning electron microscopy (SEM), what is it for?. ATRIA Innovation. (2025, March 19). https://atriainnovation.com/en/blog/scanning-electron-microscopy-uses/

[16] Zhang, Rui & Ulery, Bret. (2018). Synthetic Vaccine Characterization and Design. Journal of Bionanoscience. 12. 1-11. 10.1166/jbns.2018.1498.

[17] Bian, K., Gerber, C., Heinrich, A. J., Müller, D. J., Scheuring, S., & Jiang, Y. (2021). Scanning probe microscopy. In Nature Reviews Methods Primers (Vol. 1, Issue 1). Springer Nature. https://doi.org/10.1038/s43586-021-00033-2

[18] Lin, T. E., Bondarenko, A., Lesch, A., & Girault, H. H. (2018). Scanning electrochemical microscopy for bioimaging. In Encyclopedia of Interfacial Chemistry: Surface Science and Electrochemistry (pp. 445–452). Elsevier. https://doi.org/10.1016/B978-0-12-409547-2.13509-7

[19] Voigtländer, B. (n.d.). NanoScience and Technology Atomic Force Microscopy Second Edition. http://www.springer.com/series/3705

[20] Public Domain, https://commons.wikimedia.org/w/index.php?curid=3592868

[21] Augustyn, A., Rodriguez, E., Chauhan, Y., Gaur, A., Gregersen, E., Hosch, W. L., & Lotha, G. (Eds.). (1998, July 20). Hooke's law. Encyclopedia of Britannica. https://www.britannica.com/

[22] https://www.maxiv.lu.se/beamlines-accelerators/support-labs/microscopy-labs/atomic-force-microscope/afm-scanning-modes/

[23] Ertürk, G., & Mattiasson, B. (2017). Molecular imprinting techniques used for the preparation of biosensors. In Sensors (Switzerland) (Vol. 17, Issue 2). MDPI AG. https://doi.org/10.3390/s17020288

[24] Refaat, D., Aggour, M. G., Farghali, A. A., Mahajan, R., Wiklander, J. G., Nicholls, I. A., & Piletsky, S. A. (2019). Strategies for molecular imprinting and the evolution of MIP nanoparticles as plastic antibodies—synthesis and applications. In International Journal of Molecular Sciences (Vol. 20, Issue 24). MDPI AG. https://doi.org/10.3390/ijms20246304

[25] Hanson, M., & Wypych, A. (2019). Introduction. In Databook of Curatives and Crosslinkers (pp. 1–2). Elsevier. https://doi.org/10.1016/b978-1-927885-49-9.50003-7

[26] Khumsap, Tabkrich & Corpuz, Angelica & Nguyen, Loc Thai. (2021). Epitope-imprinted polymers: applications in protein recognition and separation. RSC Advances. 11. 11403-11414. 10.1039/D0RA10742E.

[27] Sajini, T., & Mathew, B. (2021). A brief overview of molecularly imprinted polymers: Highlighting computational design, nano and photo-responsive imprinting. In Talanta Open (Vol. 4). Elsevier B.V. https://doi.org/10.1016/j.talo.2021.100072

[28] Professor K.S. K.S Sree Harsha. (2005). Principles of Vapor Deposition of Thin Films, 1st Edition.

[29] 184, V. E., Er, N. B., Targets, P., & Sigmundt, P. (1969). PHYSICAL REVIEWS Theory of Sputtering. I. Sputtering Yield of Amorphous and.

[30] Balwanz, W. W. (1979). Plasma Cleaning of Surfaces. In: Mittal, K.L. (eds) Surface Contamination. https://doi.org/https://doi.org/10.1007/978-1-4684-3506-1_17

[31] Thanu, D. P. R., Srinadhu, E. S., Zhao, M., Dole, N. v., & Keswani, M. (2018). Fundamentals and applications of plasma cleaning. In Developments in Surface Contamination and Cleaning: Applications of Cleaning Techniques Volume 11 (pp. 289–353). Elsevier. https://doi.org/10.1016/B978-0-12-815577-6.00008-6

[32] Davide. (2024, April 15). Plasma Cleaning: What Is It And How It Works. sciplasma. https://www.sciplasma.com/post/plasma-cleaning-overview

[33] Hinman, Samuel. (2017). Plasmonic Interrogation of Biomimetic Systems for Enhanced Toxicity Assays.

[34] Manakhov, Anton. (2012). Towards the thermally reversible adhesion between metallic and polymeric surfaces functionalized by atmospheric plasma polymerization and gas phase reactions / Manakhov Anton. - Namur : Presses universitaires de Namur,.

[35] Yan, H., & Ho Row, K. (2006). Characteristic and Synthetic Approach of Molecularly Imprinted Polymer. Int. J. Mol. Sci, 7, 155–178. www.mdpi.org/ijms/

[36] Wang, C., Yan, Q., Liu, H. B., Zhou, X. H., & Xiao, S. J. (2011). Different EDC/NHS activation mechanisms between PAA and PMAA brushes and the following amidation reactions. Langmuir, 27(19), 12058–12068. https://doi.org/10.1021/la202267p

[37] Yan, Q., Zheng, H. N., Jiang, C., Li, K., & Xiao, S. J. (2015). EDC/NHS activation mechanism of polymethacrylic acid: Anhydride versus NHS-ester. RSC Advances, 5(86), 69939–69947. https://doi.org/10.1039/c5ra13844b

[38] Lis, M., & Tew, G. N. (2012). 9.16 - Polymer–Membrane Interactions. In Polymer Science: a Comprehensive Reference: Volume 1-10 (Vols. 1–10, pp. 289–315). Elsevier. https://doi.org/10.1016/B978-0-444-53349-4.00251-X

[39] Sincari, V., Petrova, S. L., Konefał, R., Hruby, M., & Jäger, E. (2021). Microwave-assisted RAFT polymerization of N-(2-hydroxypropyl) methacrylamide and its relevant copolymers. Reactive and Functional Polymers, 162. https://doi.org/10.1016/j.reactfunctpolym.2021.104875

[40] Matsumoto, A., Ando, H., & Oiwa, M. (1989). GELATION IN THE COPOLYMERIZATION OF METHYL METHACRYLATE WITH TRIMETHYLOLPROPANE TRIMETHACRYLATE. In Eur. Polym. J (Vol. 25, Issue 4).

[41] https://forumautomation.com/t/types-of-chemical-sensor/5576

[42] https://pubchem.ncbi.nlm.nih.gov/compound/16-Mercaptohexadecanoic-acid#section=2D-Structure

[43] https://en.wikipedia.org/wiki/2,2%27-Azobis(2-amidinopropane)_dihydrochloride#/media/File:2,2'-Azobis(2-amidinopropane)_dihydrochloride.svg

[44] https://de.wikipedia.org/wiki/1-Ethyl-3-(3-dimethylaminopropyl)carbodiimid#/media/Datei:EDC_Structure.svg

[45] By NEUROtiker - Own work, Public Domain, https://commons.wikimedia.org/w/index.php?curid=3784899

[46] Wikimedia Foundation. (2025, May 13). Polylactic acid. Wikipedia. https://en.wikipedia.org/wiki/Polylactic_acid

List of Tables

List of Formulas:

List of Illustrations

List of chemical structures:

Here the structures of all used chemicals are listed.

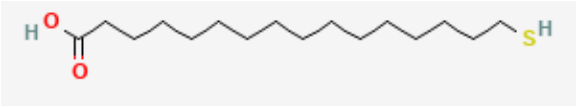

Figure 83: 16-MHDA structure [42]

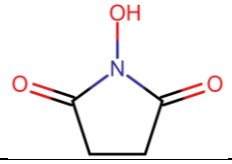

Figure 84: NHS structure

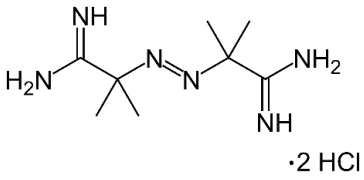

Figure 85: AAPH structure [43]

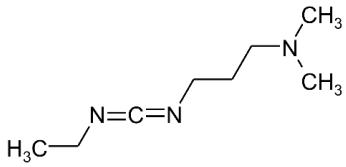

Figure 86: EDC structure [44]

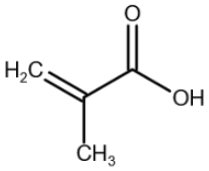

Figure 87: MAA structure

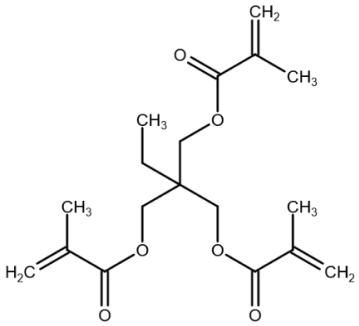

Figure 88:TRIM structure

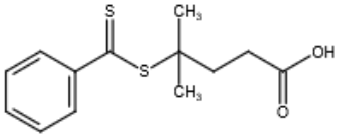

Figure 89:CPA structure

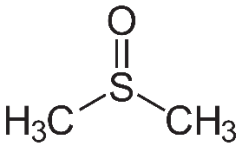

Figure 90: DMSO structure

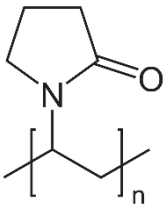

Figure 91: PVP structure [45]

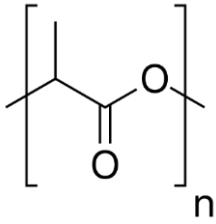

Figure 92: polylactic acid (PLA) [46]

Abstract in English

Sensors are a way to rapidly and cheaply generate highly sensitive and selective data from a sample. One of these sensors is the combination of a quartz crystal microbalance (QCM) transducer paired with a molecularly imprinted polymer (MIP) receptive layer. With this combination two different electrode designs of QCMs and their influences on the measurements were investigated. One design covered the whole QCM surface on the liquid side, while the other only covered the bare minimum of the electrodes. For usable results, physical vapor deposition (PVD) was used to deposit the electrodes on the QCM surface and a new way of selectively shielding the QCMs was developed and optimized to make manufacturing possible. Different ways of electrode manufacturing on the QCMs were investigated and compared, leaving PVD as the method of choice. Furthermore, once the QCM production was finished, the influences of the design were investigated. The QCM electrode design was not shown to have any magnificent influence on the response when using different concentrations of gold nanoparticles, but a significant decrease of noise was observed. Fully coated QCMs on average showed only ~75% of the noise than partially coated QCMs. Another point of interest was that the change in background composition influenced the measurements more on the partially covered QCMs, while the fully coated QCMs were comparatively barely influenced. To characterise, analyse and prove the cavity formation as well as rebinding of nanoparticles, atomic force microscopy and scanning electron microscopy were used.

Abstract in German

Sensoren bieten die Möglichkeit sehr schnell und billig, hoch sensitive und selektive Messdaten zu generieren. Ein solcher Sensor kombiniert einen Quartz Mikrowaagen (QCM) Transducer mit einer molekular gepägten Polymer (MIP) Rezeptorschicht. Mithilfe dieser Kombination wurden zwei verschiedene QCM Elektrodendesigns und ihre Einflüsse auf die Messungen untersucht. Bei einem Design wurde die QCM Seite mit Lösungskontakt vollkommen beschichtet, während das andere Design nur minimal beschichtet wurde so dass die Elektroden abgedeckt und Stromfluss etabliert war. Für die Elektrodenproduktion wurde physikalische Dampfabscheidung (PVD) eingesetzt und eine Möglichkeit des selektiven Abschimens der QCMs entwickelt und optimisiert. Verschiedene Methoden der Elektrodenherstellung wurden untersucht und verglichen, was PVD als geeignetste Methode ergab. Nachdem die Herstellung vollendet war wurden die Einflüsse auf QCM Messung erforscht. Das QCM Elektrodendesign hatte keinen nachweisbaren Einfluss auf die Sensorantwort bei unterschiedlichen Kenzentrationen von Goldnanopartikeln. Es wurde ein deutlicher Einfluss beim Rauschen erfasst. Voll beschichtete QCMs zeigten durchschnittlich nur 75% so starkes Rauschen als die teilweise beschichteten QCMs. Weiters wurde observiert dass völlig beschichtete QCMs weniger stark von der Zusammensetzung der Lösung beeinflusst werden. Zur Charakterisierung, Analyse und zum Nachweis der Kavitätbildung als auch Wiederbindung von Goldnanopartikeln, wurden Rasterkraftmikroskopie und Rasterelektronenmikroskopie eingesetzt.